ABSTRACT

Title of dissertation: ELECTRON ACCELERATION IN MAGNETIC RECONNECTION

Joel Timothy Dahlin, Doctor of Philosophy, 2015

Dissertation directed by: Professor James Drake
Department of Physics

Magnetic reconnection is a ubiquitous plasma physics process responsible for the explosive release of magnetic energy. It is thought to play a fundamental role in the production of non-thermal particles in many astrophysical systems. Though MHD models have had some success in modeling particle acceleration through the test particle approach, they do not capture the vital feedback from the energetic particles on the reconnection process. We use two and three-dimensional kinetic particle-in-cell (PIC) simulations to self-consistently model the physics of electron acceleration in magnetic reconnection. Using a simple guiding-center approximation, we examine the roles of three fundamental electron acceleration mechanisms: parallel electric fields, betatron acceleration, and Fermi reflection due to the relaxation of curved field lines. In the systems explored, betatron acceleration is an energy sink since reconnection reduces the strength of the magnetic field and hence the perpendicular energy through the conservation of the magnetic moment. The 2D simulations show that acceleration by parallel electric fields occurs near the magnetic X-line and the separatrices while the acceleration due to Fermi reflection fills

the reconnection exhaust. While both are important, especially for the case of a strong guide field, Fermi reflection is the dominant accelerator of the most energetic electrons. In a 3D systems the energetic component of the electron spectra shows a dramatic enhancement when compared to a 2D system. Whereas the magnetic topology in the 2D simulations is characterized by closed flux surfaces which trap electrons, the turbulent magnetic field in 3D becomes stochastic, so that electrons wander over a large region by following field lines. This enables the most energetic particles to quickly access large numbers of sites where magnetic energy is being released.

ELECTRON ACCELERATION IN MAGNETIC RECONNECTION

by

Joel Timothy Dahlin

Dissertation submitted to the Faculty of the Graduate School of the
University of Maryland, College Park in partial fulfillment
of the requirements for the degree of
Doctor of Philosophy
2015

Advisory Committee:
Professor James F. Drake, Chair/Advisor
Dr. Michael M. Swisdak, Co-Advisor
Professor William D. Dorland
Professor Adil B. Hassam
Professor M. Coleman Miller, Dean's Representative

Dedication

To my parents, who have supported and encouraged me from the beginning.

Acknowledgments

I am grateful to my advisor, Professor James Drake, for inviting me into his research group and guiding me on my journey through graduate school. It was always clear that had my career needs in mind every step of the way. I would also like to thank my co-advisor, Dr. Marc Swisdak. His door has always been open, and many were the hours graciously given to help with my work. I would havebeen fortunate to have had either as an advisor, and count myself remarkably privileged to have had both. Thanks go also to Adil Hassam, Bill Dorland, and Cole Miller for graciously agreeing to sit on my committee.

I would like to acknowledge my officemates present and past: Wrick Sengupta, Lora Price, Qile Zhang, Kevin Schoeffler, and Ray Fermo. These friends made my workplace a place of both camaraderie and scientific curiosity. Similar thanks go to my colleagues in the plasma group: Jimmy Juno, George Wilkie, Obioma Ohia, Jason Tenbarge, and Matt Landreman. I am also grateful for the 'conference buddies' who provided valuable company at scientific meetings and gave me glimpses into topic areas I would not otherwise have encountered. I especially appreciate the friendship of Micah Weberg, Kalman Knizhnik, Aleida Higginson, Lauren Woolsey, Mark Stakhiv, and Sam Schonfeld.

I would also like to acknowledge the IREAP and Physics department staff who have helped me along my graduate journey. I am especially grateful for the efforts of Jane Hessing and Mohini Kaul, who sorted out oh-so-many administrative issues over the years. I would like to give a special thanks to Prof. Peter Shawhan who

went above and beyond the duties of his position in helping me.

I am thankful for the housemates with whom I've lived in peace and friendship: Anto Peter, Walt Muench, Jake McCann, Scott Low, Aaron Hagerstrom, Freja Nordsiek, Anne Handschy, Avinash Kumar, and David Meyer. My friends at Maryland Christian Fellowship have provided a loving and supportive community. I would especially like to acknowledge the guidance and encouragement of Jeff Warner and Aaron Lohr. I have also valued my friendships with fellow believing physicists: Jonathan Larson, Yi-Hsieh Wang, Kristen Burson, and Erin Marshall.

I would like next to thank my family, especially my parents Carolyn and Tim and siblings Karin and Jonathan. Their uncondtional love and support have been a great boon in this journey.

Thanks are finally due to the God who created all the wondrous delights that I have been privileged to explore and who provides the ultimate source of value for anything I do.

Table of Contents

List of Figures

List of Abbreviations

$\mathbf{B}$	Magnetic Field
$\mathbf{b}$	Magnetic Field Unit Vector ($\mathbf{B}/\lvert\mathbf{B}\rvert$)
$\boldsymbol{\kappa}$	Magnetic Curvature
$\mathbf{E}$	Electric Field
$\mathbf{u_E}$	E-cross-B velocity.
$\mathbf{J}$	Current Density
$\mathbf{v}$	Plasma Flow Velocity
$E_\parallel$	Parallel Electric Field ($\mathbf{E}\cdot\mathbf{b}$)
P	Plasma Pressure
T	Plasma Temperature
n	Particle Density
β	Plasma Beta
ρ	Mass Density
μ	Magnetic Moment
d_i	Proton Inertial Length
d_e	Electron Inertial Length
λ_D	Debye Length
ρ_i	Proton Larmor Radius
Ω_{ci}	Proton Cyclotron Frequency
Ω_{ce}	Electron Cyclotron Frequency
ω_{pe}	Electron Plasma Frequency
c_A	Alfvén Velocity
c_{Ae}	Electron Alfvén Velocity
S	Lundquist Number
η	Resistivity
c	Speed of Light
γ	Lorentz Factor
e	Elementary Charge
m_e	Electron Mass
m_i	Proton Mass
ϵ	Particle Kinetic Energy
R_e	Earth Radius

TRACE	Transition Region and Coronal Explorer
RHESSI	Reuven Ramaty High Energy Solar Spectroscopic Imager
ACRs	Anomalous Cosmic Rays
DSA	Diffusive Shock Acceleration
PIC	Particle-in-Cell
MHD	Magnetohydrodynamics
CGL	Chew-Goldberger-Low

Chapter 1: Introduction

1.1 History

Magnetic reconnection is a fundamental plasma physics process that converts magnetic energy into plasma energy through a change in the magnetic topology. It is thought to play an important role in the dynamics of many astrophysical systems including the solar corona, planetary magnetospheres, magnetic sectors of the solar wind, pulsar wind nebulae, and black holes. Reconnection is also of great importance in the context of laboratory fusion devices, as it is the driver of the sawtooth crash which disrupts confinement in fusion devices.

The history of magnetic reconnection begins with the puzzle of solar flares. Solar flares are sudden flashes of brightening just above the surface of the sun. Perhaps the earliest and most famous of solar flares was the one independently reported in 1859 by the English amateur astronomers R. C. Carrington and R. Hodgson [1,2]. This flare, now commonly known as the 'Carrington Flare', disrupted telegraph communications and resulted in powerful aurorae that extended as far south as Cuba [3]. Fig. 1.1 depicts Carrington's visible-light observation as reported in the the Monthly Notices of the Royal Astronomical Society. By comparison, figure 1.2 shows a recent soft X-ray image of a solar flare taken by the TRACE satellite.

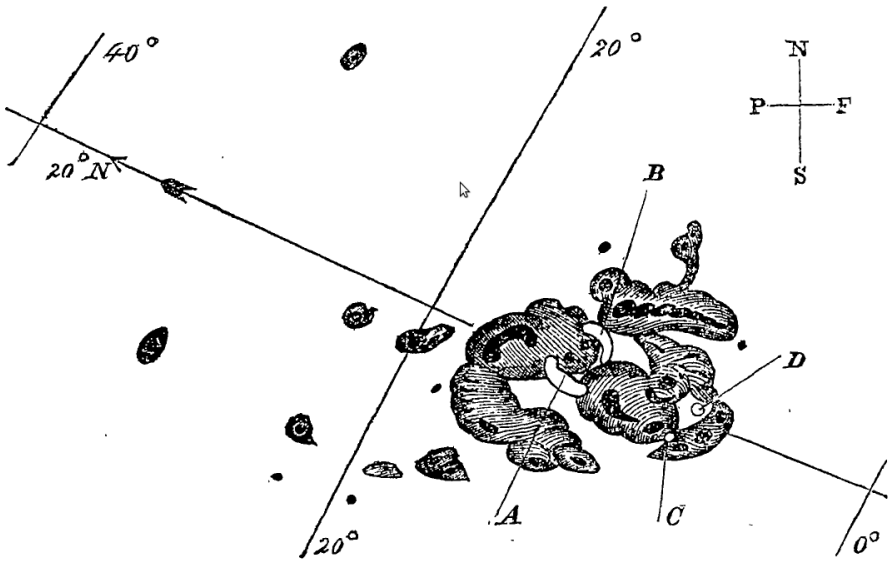

Figure 1.1: R. C. Carrington's diagram of the September 1, 1859 solar flare. The flare began with bright light appearing in the areas labeled A and B, and faded in intensity as it moved toward points C and D. Reprinted with permission from Carrington (1859) [1].

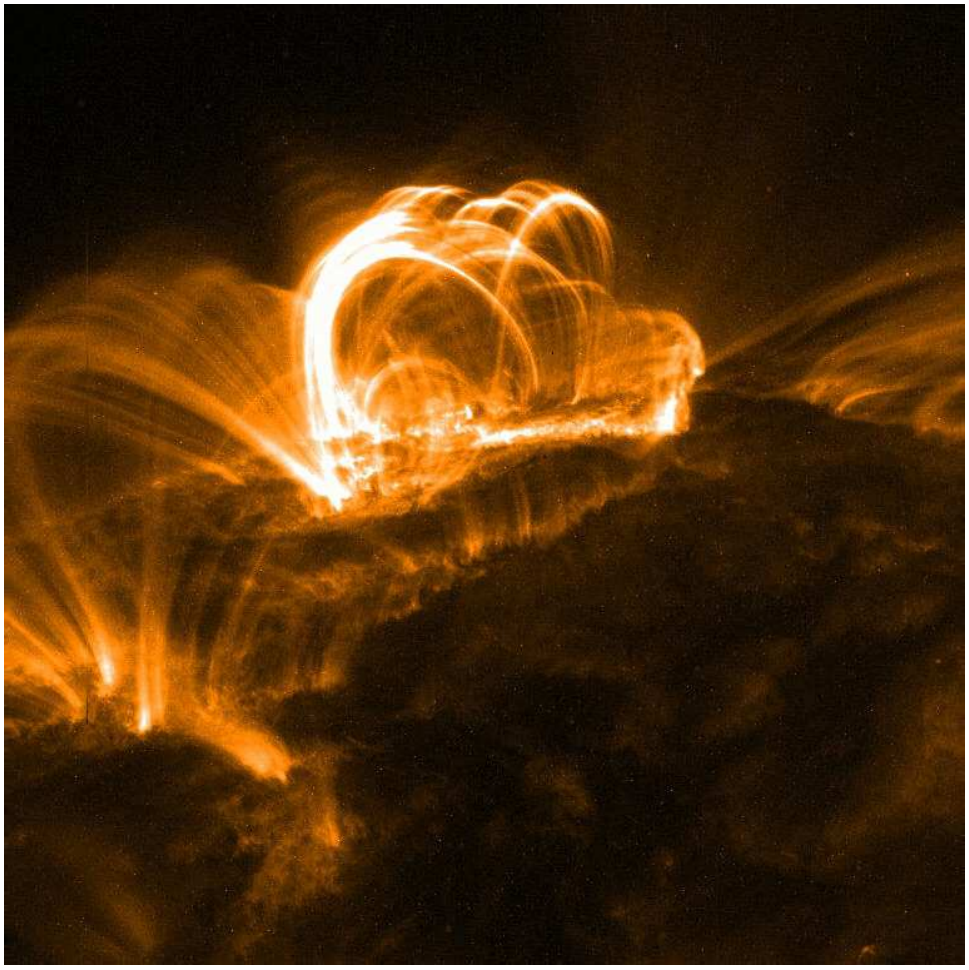

Figure 1.2: X-ray image of a solar flare. Image taken September 2005 by the TRACE Satellite. Credit: NASA/LMSAL.

Though observations steadily improved, the source of this phenomenon remained a mystery for almost a century. In 1947, Ron Giovanelli [4] noted that solar flares were associated with regions where there was a magnetic null point - that is, where the field changes direction. This idea was eventually pursued by James Dungey, who suggested that oppositely oriented field lines would break apart and reconnect due to diffusion, forming a thin current sheet in the process [5, 6].

It was around this time that P. A. Sweet presented an idea for how such a reversed field configuration could be formed. Bipolar field configurations just above the surface of the sun could be pressed together; these oppositely oriented fields, thus driven together, could then reconnect in a similar manner to that proposed by Dungey. E. N. Parker was present at the conference where Sweet gave his talk, and subsequently derived the steady state scaling analysis of what is now known as the Sweet-Parker reconnection [7, 8]. Parker's depiction of this model is shown in Fig. 1.3. This model was an important advance in that it showed that magnetic energy could be dissipated at a rate much greater than what would be predicted by simple diffusion. However, it was still too slow to explain the rapid dissipation observed in solar flares.

A few years after this model was proposed, H. E. Petscheck devised a solution in which the inflow and outflow regions are separated by slow shocks. These shocks facilitate a rate of magnetic energy dissipation that would be substantially greater than that of the Sweet-Parker model [10]. However, numerical simulations found that this configuration would only persist if the resistivity was locally enhanced [11]; it would otherwise revert to a Sweet-Parker configuration [12].

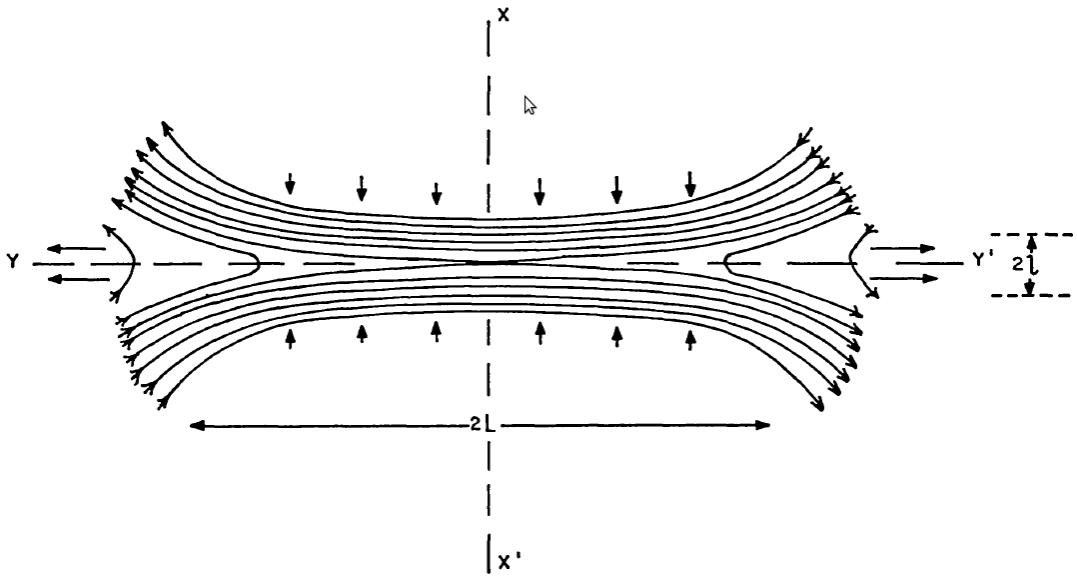

Figure 1.3: Diagram of Sweet-Parker reconnection. Antiparallel magnetic field lines are driven together from above and below a central current sheet. The field lines 'merge' or reconnect, and are expelled to the left and right. Reprinted from Parker, 1963 [9].

More recently, work in collisionless reconnection has showed that the reconnection rate can be fast when the width of the current layer is thin enough that a fluid description of the plasma becomes inadequate. This is due to the presence of small-scale kinetic physics that allows magnetic flux to slip past the plasma more rapidly than would be expected from resistive diffusion. Comparisons of a variety of numerical models showed a remarkable invariance of the reconnection rate so long as a minimum set of kinetic physics was included [13].

Reconnection occurs in a variety of regimes: from dense, collisional plasmas in fusion devices to collisionless reconnection in the magnetotail, to relativistic phenomena where the dominant positively charged species is the positron. Reconnection may be focused near a narrow current sheet where its onset is determined by the tearing instabilities, or it may be globally driven by large-scale external flows. Given the breadth of this field, this thesis will primarily focus on the dynamics of thin current sheets in collisionless systems. The localized, intense dynamics of a current sheet enable rapid acceleration of particles, and the absence of collisions allows the production of superthermal particles with energies much larger than the temperature of the ambient medium.

1.2 Observations of Energetic Particles in Reconnection

Magnetic reconnection is often found to be accompanied by the production of energetic particles. Prominent early studies of superthermal electron production during solar flares date back to the 1960's, when X-ray spectra were used to deduce

energetic populations well above 10 keV. [14–16]. The Reuven Ramaty High Energy Solar Spectroscopic Imager (RHESSI) is the leading modern experiment for studying the production of energetic particles during solar flares. It is capable of spatially resolving hard X-ray sources in order to isolate the origin of the energetic spectra. Observations of over-the-limb flares (where the intensely radiating footpoints are occulted by the solar disc) have recently been used to isolate X-ray sources near the flaring region. Figure 1.4 shows a RHESSI image of an above-the-looptop source for energetic particles; electron energy spectra inferred from this source have large superthermal components that may contain a significant fraction of the released magnetic energy [17, 18]. Other studies have found that the energetic electron production can comprise a significant fraction ($\sim 10\%$) of the energy budget in a solar flare/coronal mass ejection event [15, 19].

A number of in-situ magnetospheric observations have also found energetic electrons associated with magnetic reconnection. A magnetotail reconnection event reported by Øieroset et al. [20] was accompanied by energetic electrons that formed power laws extending up to 300 keV. These energies are significant in that they greatly exceed the kinetic energy associated with characteristic electron velocities such as the Alfvén speed [21] ($m_e c_{Ae}^2 \sim 2\text{keV}$). A number of other observations [21–23] find that energetic electron fluxes are enhanced along magnetic separatrices and within magnetic islands.

Though these are the most thoroughly documented observations associating energetic particle production with the reconnection process, there are a number of other scenarios where reconnection might be important for energetic particle produc-

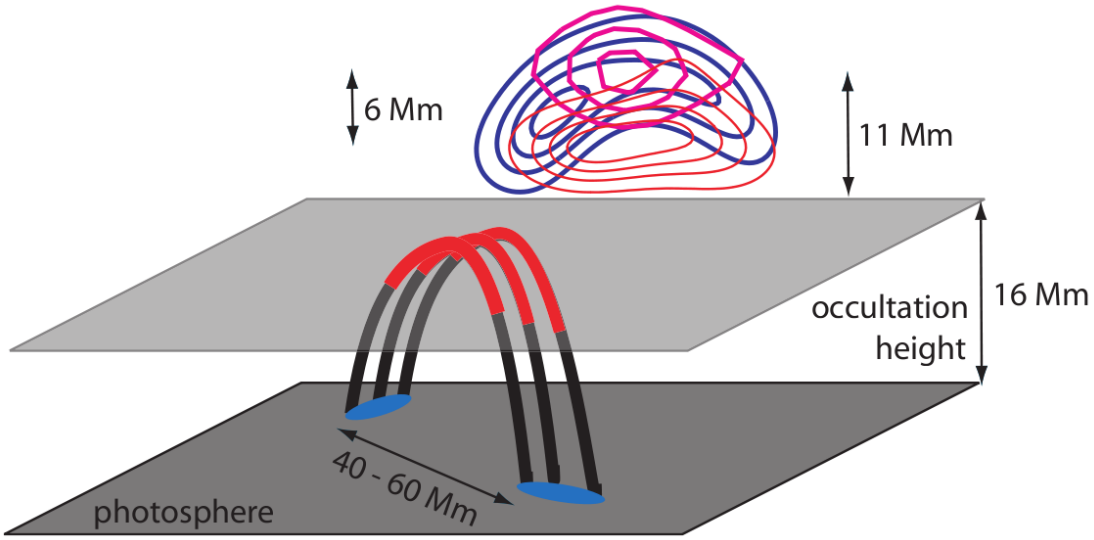

Figure 1.4: Cartoon diagram of over-the-limb solar flare observed by RHESSI. The flare loops are shown as black and red tubes. Hard X-rays ($30 - 50$ keV) are shown in blue contours, and microwaves are shown in magenta. Reprinted from Krucker et al., 2010 [17].

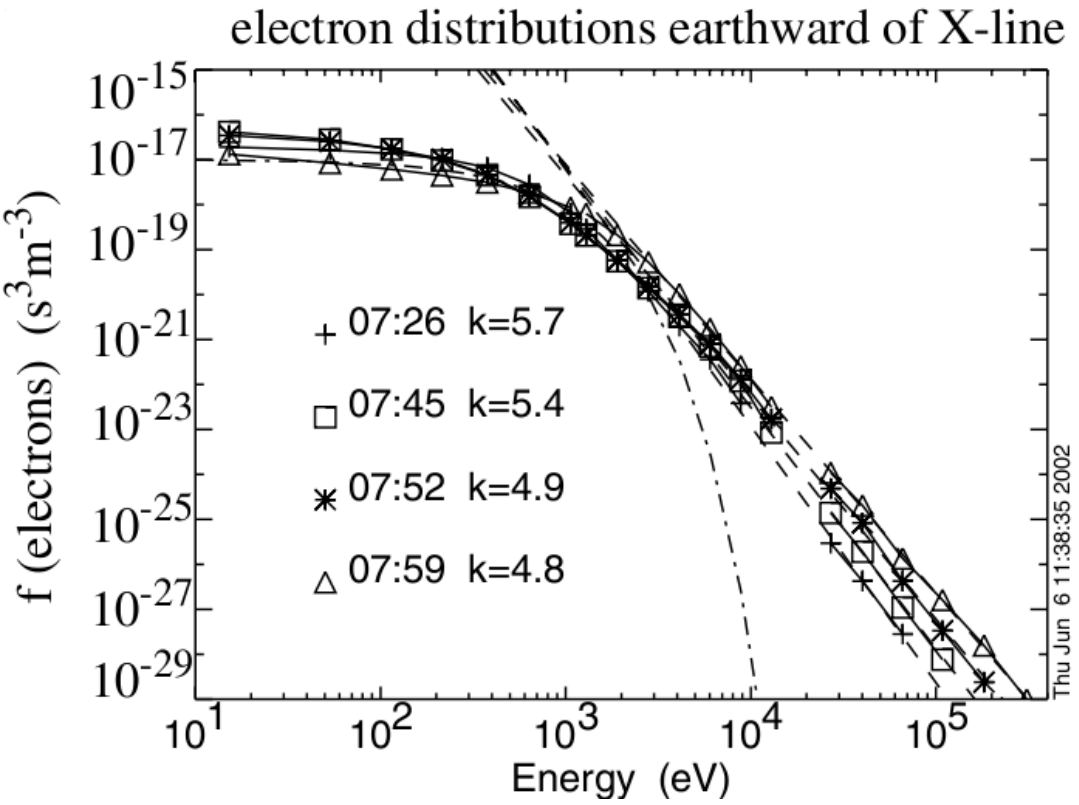

Figure 1.5: Electron energy spectra earthward of a magnetotail X-line. Reprinted from Øieroset et al., 2002 [20].

tion. One such example comes from the outer heliosphere where the stacked sectors of the heliospheric current sheet provide an ideal environment for efficient magnetic reconnection. The reconnection process has recently been posed as a possible means for accelerating the Anomalous Cosmic Rays (a population of 10-100 MeV/nucleon singly-ionized ions with a composition matching the interstellar medium) [24, 25]. Pulsar wind nebulae such as the Crab Nebula have similar geometries to that described in the heliosheath. It has been suggested that reconnection may be vital for facilitating the transition from a magnetically-dominated regime near the base to a particle-dominated at the termination shock of the pulsar wind. Reconnection may also explain remarkable recent gamma-ray observations in which the photon energy exceeded the expected theoretical limit for synchrotron radiation [26, 27].

The prospects of reconnection as an efficient particle accelerator have driven efforts to study it in the context of accretion discs, black hole jets, and magnetars (neutron stars with strong magnetic fields). The well-known Cosmic Ray spectrum forms a power law extending over ten orders of magnitude, up to 10^{20} eV. The standard mechanism for the energization of cosmic rays is Diffusive Shock Acceleration (DSA) at supernova remnant shocks. DSA is a type of Fermi acceleration [28] which occurs in the vicinity of astrophysical shocks. However, some authors have suggested that magnetic reconnection may play a role in the production of the most energetic cosmic rays [29].

1.3 Summary of Results

A vast body of evidence shows that magnetic reconnection is an important driver of energetic particles in astrophysical environments. Though significant progress has been made in numerical study of particle acceleration, there have been few studies which treat this issue in a fully three-dimensional system where turbulent structure can impact the transport of particles and confinement in the reconnection region.

In this thesis, I first discuss fundamental aspects of reconnection theory and argue that a kinetic treatment of fully three-dimensional reconnection is vital for capturing essential physics of the particle acceleration problem. I then present an intuitive guiding-center model for particle energization and discuss the physical importance of several important mechanisms that arise in this model: electric fields parallel to the magnetic field accelerate particles directly while those perpendicular to $\mathbf{B}$ do so through gradient-B and curvature drifts. The curvature drift drives parallel heating through Fermi reflection while the gradient-B drift changes the perpendicular energy through betatron acceleration.

I then evaluate the relative importance of these mechanisms in two-dimensional kinetic simulations. For a case with a small guide field (20% of the magnitude of the reconnecting component) the curvature drift is the dominant source of electron heating. However, for a larger guide field (equal to the magnitude of the reconnecting component) electron acceleration by the curvature drift is comparable to that of the parallel electric field. In both cases the heating by the gradient-B drift is

negligible in magnitude. It produces net cooling because the conservation of the magnetic moment $\mu = mv_\perp^2/2B$ (where m is the mass, and $v_\perp$ is the velocity perpendicular to the field) and the drop of B during reconnection produce a decrease in the perpendicular electron energy. Heating by the curvature-drift dominates in the outflow exhausts where bent field lines expand to relax their tension and is therefore distributed over a large area. In contrast, the parallel electric field is localized near X-lines. This suggests that acceleration by parallel electric fields may play a smaller role in large systems where the X-line occupies a vanishing fraction of the system. The curvature drift and the parallel electric field dominate the dynamics and drive parallel heating. A consequence is that the electron energy spectrum becomes extremely anisotropic at late time, which has important implications for quantifying the limits of electron acceleration due to synchrotron emission. An upper limit on electron energy gain that is substantially higher than earlier estimates is obtained by balancing reconnection drive with radiative loss.

I proceed to examine electron acceleration in a three-dimensional system. Electron acceleration is greatly enhanced when compared with a 2D system. In the 2D system, electrons are trapped in magnetic islands which limits their energy gain by inhibiting access to regions near the X-line and reconnection exhaust where magnetic energy is released. In the 3D system, however, the stochastic magnetic field enables the electrons to access volume-filling acceleration regions. The dominant accelerator of the most energetic electrons is a Fermi-type mechanism associated with the curvature drift.

I then briefly examine how the three-dimensional results scale with the system

size and mass ratio. I find that the relative enhancement of particle acceleration increases with the system size. This suggests that the physical results discussed in this thesis will be even more important for astrophysical regimes much larger than what can be captured in kinetic simulations. Additionally, I find that the key features of the three-dimensional simulations are preserved in a system with a more realistic proton-to-electron mass ratio, suggesting that these results are robust and relevant for physical systems.

Chapter 2: Magnetic Reconnection Theory

In this chapter, I briefly describe the theoretical background for the modern understanding of magnetic reconnection. I begin by presenting the ideal magnetohydrodynamic (MHD) formulation of plasma physics and discuss the concept of magnetic tension and the approximate conservation law known as the 'frozen flux theorem'. I then discuss a simplified picture of reconnection and describe how the violation of the frozen flux theorem facilitates energy release through field line shortening driven by magnetic tension. I then discuss steady-state reconnection including the slow Sweet-Parker model and compare it to fast reconnection at kinetic scales. I proceed to argue that a treatment which includes kinetic physics in a three-dimensional system is vital for considering the particle acceleration problem. I conclude by describing the particle-in-cell (PIC) formulation used in the simulations examined in this thesis.

2.1 Magnetohydrodynamics

The magnetohydrodynamic (MHD) formulation treats plasma as a conducting fluid. This is useful for studying reconnection on large temporal and spatial scales. MHD combines Maxwell's equations with the Navier-Stokes equations. Below are

the ideal equations, where the plasma is taken to be a perfectly conductive fluid with no viscosity:

$$\frac{d\rho}{dt} + \rho \boldsymbol{\nabla} \cdot \mathbf{v} = 0 \tag{2.1}$$

$$\rho \frac{d\mathbf{v}}{dt} = \frac{1}{c} \mathbf{J} \times \mathbf{B} - \boldsymbol{\nabla} P \tag{2.2}$$

$$\frac{\partial \mathbf{B}}{\partial t} = -\frac{1}{c} \boldsymbol{\nabla} \times \mathbf{E} \tag{2.3}$$

$$\mathbf{J} = \frac{c}{4\pi} \boldsymbol{\nabla} \times \mathbf{B} \tag{2.4}$$

$$\mathbf{E} + \frac{\mathbf{v} \times \mathbf{B}}{c} = 0 \tag{2.5}$$

Equations 2.4 and 2.5 can be used to eliminate the current density $\mathbf{J}$ and the electric field $\mathbf{E}$, yielding a set of equations in the following set of variables: the mass density ρ, the bulk flow $\mathbf{v}$, the magnetic field $\mathbf{B}$ and the pressure scalar P. The operator $d/dt \equiv \partial/\partial t + \mathbf{v} \cdot \boldsymbol{\nabla}$ is the convective derivative. An additional equation is required in order to close this set of equations; a common choice is the adiabatic equation of state:

$$\frac{d}{dt}\left(\frac{P}{\rho^\gamma}\right) = 0$$

where γ is the ratio of specific heats. Ampère's law can be used to rewrite the momentum equation (2.2) in the following form:

$$\rho \frac{d\mathbf{v}}{dt} = -\boldsymbol{\nabla} P - \boldsymbol{\nabla}_\perp \frac{B^2}{8\pi} + \boldsymbol{\kappa} \frac{B^2}{4\pi} \tag{2.6}$$

where the perpendicular gradient $\boldsymbol{\nabla}_\perp \equiv \boldsymbol{\nabla} - \mathbf{b}(\mathbf{b}\cdot\boldsymbol{\nabla})$ is defined with respect to the unit vector in the direction of the magnetic field: $\mathbf{b} = \mathbf{B}/B$. The second term on the right-hand-side acts similarly to the thermal pressure, though it only operates tranverse to the magnetic field. The final term corresponds to magnetic tension which acts in the direction of the magnetic curvature $\boldsymbol{\kappa} \equiv \mathbf{b}\cdot\boldsymbol{\nabla}\mathbf{b}$. Magnetic tension drives the Alfvén wave, a fundamental MHD wave which propagates at a velocity which depends on the magnetic field magnitude and the mass density: $c_A = B/\sqrt{4\pi\rho}$

The quantity $\boldsymbol{\kappa} = d\mathbf{b}/dl$ describes the curvature of the magnetic field (dl is an infinitesimal displacement along the field line). Integration of this along a field line yields the change in the magnetic field vector:

$$\begin{aligned}\int d\ell\boldsymbol{\kappa} &= \int d\ell(\mathbf{b}\cdot\boldsymbol{\nabla}\mathbf{b}) \\ &= \int d\ell\frac{d}{d\ell}\mathbf{b} \\ &= \mathbf{b}_2 - \mathbf{b}_1\end{aligned}$$

The magnetic curvature can be related to a local radius of curvature: $\boldsymbol{\kappa} = -\mathbf{R}/R^2$. Hence the magnetic curvature points in the opposite direction as a radius vector.

An important result of ideal MHD is the 'frozen-in-flux' law, which states that the magnetic flux through a surface moving with the fluid is conserved:

$$\int_S \mathbf{B}\cdot d\mathbf{S} = const \tag{2.7}$$

This follows straightforwardly from Eqns. 2.3 and 2.5 which together yield:

$$\frac{\partial\mathbf{B}}{\partial t} = \boldsymbol{\nabla}\times(\mathbf{v}\times\mathbf{B}) \tag{2.8}$$

Due to this property, it is often useful to describe the dynamics of field lines which co-move with the plasma. Two fluid elements along a given field line will therefore always be threaded by the same field line, and hence a field line cannot 'break'. This a good approximation for many large-scale systems.

2.2 The Basics of Reconnection Theory

2.2.1 The Self-Driven Process: Breaking Field Lines

An important aspect of magnetic reconnection is that it 'breaks' this approximate conservation law. A simple picture of a 2D 'X-line' is shown in Fig. 2.1. This geometry includes a central current sheet that separates magnetic fields of opposite polarity. Four topological domains are divided by separatrices which meet at the central 'X'.

Magnetic tension pulls the strongly curved magnetic fields away from the central X. This drives down the pressure at the X-line, and therefore pulls in new plasma. However, for this to happen, the newly inflowing field lines must pass across the separatrices, 'breaking' and reconnecting with each half of a pair on the other side of the X-line. In other words, plasma elements once threaded by a single field line are no longer topologically connected. This therefore suggests that 2.7 is not be valid, and implies that physics omitted from the ideal Ohm's law (Eqn. 2.5) play an important role in enabling the magnetic field to slip past the plasma in the vicinity of the X-line (this volume is known as the 'diffusion region', and is depicted shaded in red in fig. 2.1). An important example is resistive diffusion which arises

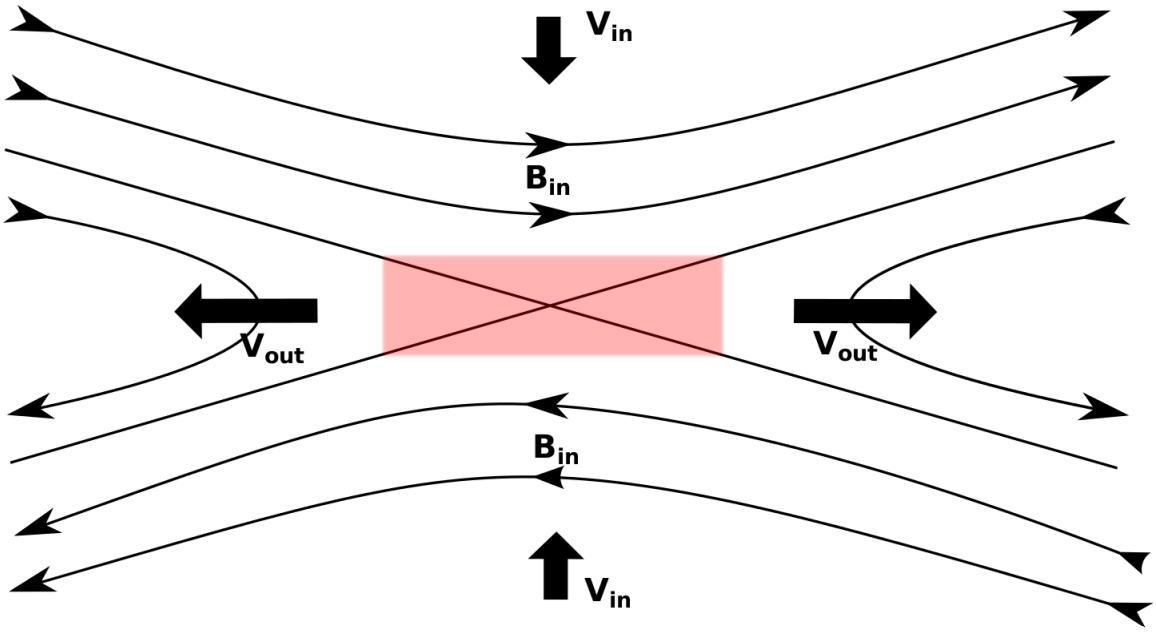

Figure 2.1: Two-dimensional magnetic reconnection diagram. A central X-line demarcates four regions of magnetic flux. Magnetic tension drives plasma away from the X-line and draws in new field lines which 'break' and reconnect as they cross the separatrices.

from the finite conductivity of the plasma.

It is important to note that while this figure includes no magnetic field in the out-of-plane direction, the two-dimensional topology is essentially equivalent in that case.

2.2.2 Magnetic Energy Release

Magnetic reconnection releases energy through the shortening of field lines via magnetic tension. Fig. 2.2 shows a contracting magnetic bubble (in reconnection, these are frequently labeled 'magnetic islands' or 'flux ropes' and are created between two X-lines). A flux tube is shown in green. The length of the initial bubble is L and the width is w. The resulting circular bubble is described by a radius R, and the flux contained in the island is given by Φ. Reconnection is a nearly incompressible process (the inflow velocities are sub-magnetosonic, which allows magnetosonic waves to propagate and enforce pressure balance) so the contraction preserves the island area $A \approx wL \approx R^2$ so that $R = \sqrt{wL}$. In the elongated island, most of the magnetic energy is in the horizontal magnetic field $B_i = \Phi/w$. In the circular bubble, the magnetic field is a constant $B_f = \Phi/R$. The energy release through this process is then:

$$A(B_i^2 - B_f^2)/8\pi = A\frac{B_i^2}{8\pi}(1 - B_f^2/B_i^2) = A\frac{B_i^2}{8\pi}(1 - \frac{w}{L}) \tag{2.9}$$

so that if $w \ll L$, almost all of the initial energy is released.

Though the picture above is only a toy model, it illustrates the general magnetic energy release process. The released magnetic energy must therefore be trans-

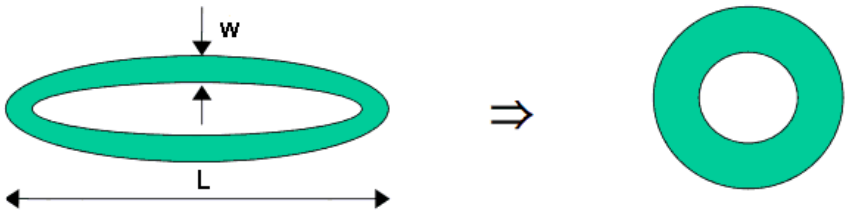

Figure 2.2: Cartoon diagram of a flux tube in a contracting magnetic bubble. Figure courtesy of Jim Drake.

ferred to the kinetic energy of the plasma, either in bulk flows, thermal energy, or energetic particles. Magnetic reconnection generates bulk outflows on the order of the Alfvén speed. These outflows may carry a substantial amount of energy, and are typically some of the clearest in-situ signatures of the process.

There are also a number of ways in which the plasma may be heated. For example, cold ions in the reconnection exhaust may reflect from retracting field lines, (in a manner analogous to a slingshot) generating counterstreaming beams that increase the effective temperature [30]. There are also a number of mechanisms for heating the electrons, including a number of beam instabilities. Some of the most important mechanisms will be discussed in Chapter 2.6.3.

Energetic particle production, where some of the plasma is accelerated to energies much larger than that of the ambient medium, can be another important avenue for magnetic energy conversion. This is particularly relevant for collisionless regimes where the small collision frequency allows non-Maxwellian distributions to form and persist. Observational evidence (discussed in a section 1.2) suggests that a large amount of energy may be released in superthermal particles. Some of the

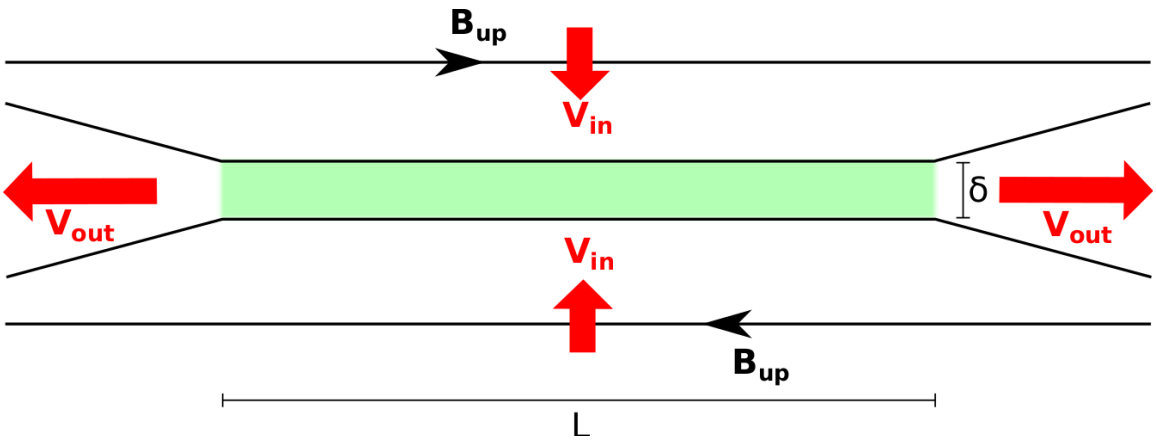

Figure 2.3: Sweet-Parker current sheet. The plasma flows advects the magnetic field B_{up} toward the diffusion region (green) with a velocity v_{in}. The field lines break and are advected outward with a velocity v_{out}.

important mechanisms for heating the bulk plasma overlap with those thought to be responsible for producing superthermal particles. For example, Fermi acceleration [28] (a mechanism in which charged particles gain energy by reflecting from magnetic field disturbances) depends on the energy ϵ of the particle: $d\epsilon/dt \propto \epsilon$ and is therefore more efficient at energizing superthermal particles. In principle, however, it may still play a role in heating the thermal population.

2.3 Steady-State Reconnection

2.3.1 Sweet-Parker Theory

In order to treat the reconnection process quantitatively, I now include a description of the well-known Sweet-Parker theory for steady-state reconnection. The simple 2D 'X-line' picture of steady-state reconnection is shown in Fig. 2.3.

Reconnection is nearly incompressible, ($\rho = const.$) so the steady-state continuity equation (2.1) becomes $\boldsymbol{\nabla} \cdot \mathbf{v} = 0$. Let δ be the thickness of the dissipation region, and L be the length, which typically corresponds to a system scale size. Take $v_y = v_{in}$ to be the velocity of the inflowing plasma (oriented in the y-direction), and $v_x = v_{out}$ to be that of the outflowing plasma. Then:

$$\frac{v_{in}}{\delta} \sim \frac{v_{out}}{L} \Rightarrow v_{in} \sim \frac{\delta}{L} v_{out} \tag{2.10}$$

Using Gauss' law ($\boldsymbol{\nabla} \cdot \mathbf{B} = 0$) based on an upstream magnetic field $B_x = B_{up}$ and a downstream magnetic field $B_y = B_{down}$, we find:

$$\frac{B_{up}}{L} \sim \frac{B_{down}}{\delta} \Rightarrow B_{down} \sim \frac{\delta}{L} B_{up} \tag{2.11}$$

where B_{up} is the horizontal component of the magnetic field immediately upstream of the dissipation region, and B_{down} is the vertical component downstream.

We may then examine the momentum equation and balance the x-component of the convection term $\rho(\mathbf{v} \cdot \boldsymbol{\nabla})\mathbf{v}$ with the tension force $(\mathbf{B} \cdot \boldsymbol{\nabla})\mathbf{B}/4\pi$, neglecting pressure gradients: $\rho v_{out}^2/L \sim B_{down}(B_{up}/\delta)/4\pi$. Using Eq. 2.11, we arrive at the result:

$$v_{out}^2 \sim \frac{B_{up}^2}{4\pi\rho} \sim c_{Aup}^2$$

where c_{Aup} is the Alfvén velocity based on the upstream plasma parameters.

Reconnection requires a form of dissipation in the MHD model, typically via a resisivity which modifies the Ohm's Law (2.5) as follows:

$$\mathbf{E} + \frac{\mathbf{v} \times \mathbf{B}}{c} = \eta \mathbf{J} \tag{2.12}$$

The electric field can then be substituted into Eq. 2.3 to obtain:

$$\frac{\partial \mathbf{B}}{\partial t} = \boldsymbol{\nabla} \times (\mathbf{v} \times \mathbf{B}) + \frac{\eta c^2}{4\pi} \boldsymbol{\nabla}^2 \mathbf{B} \tag{2.13}$$

In a steady-state, incompressible plasma, this becomes:

$$(\mathbf{B} \cdot \boldsymbol{\nabla})\mathbf{v} - (\mathbf{v} \cdot \boldsymbol{\nabla})\mathbf{B} + \frac{\eta c^2}{4\pi} \boldsymbol{\nabla}^2 \mathbf{B} = 0 \tag{2.14}$$

We can examine the y-component of this equation along the symmetry line immediately upstream of the dissipation region. The first term is zero because of the symmetry of the system. This yields:

$$v_{in} \frac{B_{up}}{\delta} \sim \frac{\eta c^2}{4\pi} \frac{B_{up}}{\delta^2} \Rightarrow \frac{v_{in}}{v_{out}} \sim \sqrt{\frac{\eta c^2}{4\pi} \frac{1}{c_{Aup} L}} \sim \frac{1}{\sqrt{S}} \tag{2.15}$$

Where S is the Lundquist number (the magnetic Reynolds number based on the Alfvén velocity, corresponding to the relative importance of the second and third terms in Eq. 2.12). As the Lundquist number is typically very large in astrophysical plasmas, this yields a low rate of reconnection, and hence of magnetic energy conversion.

The energy conversion can be summarized as follows. We take $\epsilon = \delta^2/L^2$, a small parameter. The inflowing energy is given by the Poynting flux $c\mathbf{E} \times \mathbf{B}/4\pi$, equivalent to a magnetic enthalpy flux across the dissipation region of:

$$(v_{in} L) B_{up}^2 / 4\pi \sim (c_{Aup} \delta)(B_{up}^2 / 4\pi) \tag{2.16}$$

The downstream magnetic enthalpy flux is:

$$(v_{out} \delta) B_{down}^2 / 4\pi \sim \epsilon (c_{Aup} \delta)(B_{up}^2 / 4\pi) \tag{2.17}$$

The upstream plasma flow energy is given by:

$$(v_{in}L)(\rho v_{in}^2/2) \sim \epsilon(1/2)(c_{Aup}\delta)(B_{up}^2/4\pi) \tag{2.18}$$

and finally the downstream kinetic energy flux is:

$$(v_{out}\delta)(\rho v_{out}^2/2) \sim (1/2)(c_{Aup}\delta)(B_{up}^2/4\pi) \tag{2.19}$$

The kinetic energy flux is the only term at the same order as the upstream Poynting flux, and only accounts for half of inflowing flux, suggesting that this simplified analysis fails to capture an important component of the energy conversion. In the resistive plasma scenario, Ohmic heating can help satisfy this energy budget. However, resistive physics is typically of little importance to astrophysical scenarios. Magnetic energy release must therefore occur through other means, motivating the subject of this thesis.

2.3.2 Fast Reconnection and Kinetic Physics

The preceding analysis has dealt with a fluid approach to reconnection. Recent developments have shown that when a reconnecting current sheet thins to kinetic length scales, (such as the ion inertial length $d_i = c/\omega_{pi}$, where ω_{pi} is the ion plasma frequency[1]) reconnection can proceed much more rapidly. This is due to the importance of physics such as the Hall effect, which allows the magnetic field to decouple from the protons and instead advect only with the electrons. In the Hall regime, the

[1]The ion inertial length may also be written as c_A/Ω_{ci}, the effective Larmor radius based on the Alfvén speed.

electrons carry the bulk of the current, resulting in an Ohm's law of the following form:

$$\mathbf{E} \approx -\frac{\mathbf{v_e} \times \mathbf{B}}{c} \approx \frac{\mathbf{J} \times \mathbf{B}}{ne} \tag{2.20}$$

where n is the plasma density and e is the electron charge. The electrons flow in the $\mathbf{z}$ direction in order to produce the current supporting to the magnetic field. The Lorentz force then rotates the electrons into the outflow direction. Within the electron diffusion region (current sheet thickness less than d_i), the outflow flux is then:

$$\delta v_{out} \sim \delta \left(\frac{J}{ne} \right) \sim \delta \left(\frac{c}{4\pi} \frac{B_{up}}{\delta} \right) \frac{1}{ne} \sim c_A d_i \tag{2.21}$$

Hence in this regime the outflowing plasma flux is independent of the current sheet thickness (so long as the layer thickness significantly exceeds electron scales). This modifies the reconnection rate that would otherwise be expected from current sheet thicknesses implied by $\delta \propto L/\sqrt{S}$ in astrophysical regimes where S is large. For example, the magnetotail has a Lundquist number $\sim 10^{10}$, so that $\delta/L \sim 10^{-5}$. Current sheets in the magnetotail are on the order of $10^2 d_i$, which would yield $\delta \sim 10^{-3} d_i$, well within the range where kinetic processes become relevant. A similar analysis finds $\delta << d_i$ in the solar corona.

2.4 Kinetic Reconnection

2.4.1 The Role of Feedback

A straightforward reason for the need of a kinetic treatment of reconnection is the simple fact that fluid models cannot self-consistently treat nonthermal spectra

(such as power laws) that may be produced during reconnection. Feedback from electron acceleration can play an important role in throttling magnetic reconnection. The mirror and firehose instabilities effectively constrain the plasma so that it always lies within the marginal stability boundaries: $\beta_\parallel - \beta_\perp = 2$ (firehose) and $\beta_\parallel - \beta_\perp^2/(1+\beta_\perp) = 0$ (mirror). Such behaviour has been observed in the slow solar wind [31, 32].

In gyrotropic plasma, the pressure tensor (assuming relevant time scales are below the cyclotron frequency) is given by:

$$\mathbf{P} = P_\parallel \mathbf{bb} - P_\perp(\mathbf{I} - \mathbf{bb}) \tag{2.22}$$

where $P_\parallel$ and $P_\perp$ are the parallel and perpendicular components of the pressure, $\mathbf{I}$ is the identity tensor, and $\mathbf{b}$ is the local direction of the magnetic field. The force due to the gyrotropic pressure is:

$$-\boldsymbol{\nabla}\cdot\mathbf{P} = -\boldsymbol{\nabla}_\perp P_\perp - \boldsymbol{\nabla}_\parallel P_\parallel - (P_\perp - P_\parallel)\boldsymbol{\nabla}_\parallel(\ln B) \tag{2.23}$$

$$+ (P_\perp - P_\parallel)\boldsymbol{\kappa} \tag{2.24}$$

so that the tension force ($\propto \boldsymbol{\kappa}$) in Eq. 2.6 is modified to become:

$$\left(\frac{B^2}{4\pi} - P_\parallel + P_\perp\right)\boldsymbol{\kappa} = \left(1 - \frac{\beta_\parallel}{2} + \frac{\beta_\perp}{2}\right)\frac{B^2}{4\pi}\boldsymbol{\kappa} \tag{2.25}$$

where $\beta_\perp = 8\pi P_\perp/B^2$, $\beta_\parallel = 8\pi P_\parallel/B^2$. When $\beta_\parallel - \beta_\perp = 2$, this term vanishes, corresponding to the marginal stability condition for the firehose instability. Field-aligned streaming (associated with $\beta_\parallel$) produces a centrifugal force which opposes the magnetic tension. In the context of reconnection, parallel heating due to tension-driven shortening of field lines acts as a back-reaction. In high β plasmas, this leads to very elongated magnetic islands as strong magnetic tension is required to maintain

reconnection against the back pressure of the plasma [33]. The anisotropy generated during reconnection can also lead to the development of secondary instabilities such as the Weibel instability [34].

The inclusion of pressure anisotropy absent in MHD is therefore essential for the self-consistent treatment of reconnection dynamics. The Chew-Goldberger-Low (CGL) equations form an important fluid closure which includes the effects of anisotropy. However, the CGL formulation neglects thermal transport, which is especially important in the case of electrons, where $v_{th,e} \gg c_A$. Therefore, a kinetic treatments which include the effects of thermal transport is required to capture this important aspect of the reconnection process.

2.4.2 Non-Maxwellian Distribution Functions

Non-Maxwellian distribution functions can be very important for the microscale physics of reconnection. The small collision rate in most astrophysical systems means that the timescale for relaxation to an equilibrium distribution is typically much longer than that of the relevant physical dynamics. This allows the formation of a superthermal component of the distribution function (often a power-law). Solar flare observations (described in 1.2) have found that the energetic component can contain a large fraction of the total energy in the system, which suggests that the superthermal population can contribute significantly to the dynamics. This hence provides an important reason to include kinetic physics in models of reconnection. The small-scale, non-ideal nature of the reconnection diffusion region

leads to other important distribution function dynamics such as the production of energetic beams via strong particle acceleration near the reconnection X-line. In some situations, particularly at low electron β, these beams can spawn secondary streaming instabilities which can help break field lines and enhance the effective dissipation [35, 36].

2.5 Three-Dimensional Reconnection

Though two-dimensional treatments can be useful approximations for a number of systems, there is growing evidence that some aspects of reconnection can be fundamentally different in a full three-dimensional treatment. Two-dimensional topologies are relatively simple. Consider a system where $\partial/\partial z = 0$. The magnetic field may then be written in the form:

$$\mathbf{B} = \mathbf{z} \times \boldsymbol{\nabla}\psi(x, y) + B_z(x, y)\,\mathbf{z} \tag{2.26}$$

where ψ is the flux function. The contours of the flux function trace out magnetic field lines. In the 2D picture, the topological separatrices trace out distinct magnetic 'flux surfaces'. In contrast, in three-dimensional topologies, an individual field line does not by itself form a separatrix, allowing greater freedom in the rearrangement of the magnetic field by the reconnection process. An initially laminar magnetic field can become stochastic, and individual field lines may be ergodic [37, 38] (that is, a field line traced for a sufficient distance will pass arbitrarily close to an given point in the stochastic region).

Three-dimensional topology is important even in reconnection that begins from

a quasi-2D equilibrium. The tearing mode, which is the primary instability that initiates reconnection, requires $\mathbf{B_0} \cdot \mathbf{k} = 0$ [39]. In a 2D (x,y) system with reconnecting field components $B_x(y)$, this condition simplifies to $k_x B_x = 0$, so that this instability is localized in the center of the current sheet where $B_x = 0$.

However, in a 3D system which allows a variation in z, and hence a component of the wavevector k_z, this condition is instead $k_x B_x + k_z B_z = 0$. In the presence of a finite guide field ($B_z \neq 0$), this allows a number of different possible orientations for the tearing mode, which can grow in locations away from the center of the current sheet ($B_x \neq 0$). These multiple available modes can interact nonlinearly and generate complex structure which cannot be described by closed flux surfaces or 'islands' [40, 41].

2.6 Numerical Simulations of Magnetic Reconnection

2.6.1 The Particle-in-Cell Formulation

The work described in this thesis will explore reconnection using the kinetic Particle-in-Cell (PIC) code `p3d` [42]. A cartoon diagram illustrating the Particle-in-Cell method is shown in Fig. 2.4. This code models the distribution function via representative 'macroparticles' with the appropriate charge-to-mass ratio per species. The macroparticle trajectories are evolved using the relativistic Newton-Lorentz equation:

$$\frac{d}{dt}(m\gamma\mathbf{v}) = q\left(\mathbf{E} + \frac{\mathbf{v}}{c} \times \mathbf{B}\right) \tag{2.27}$$

where m is the rest mass and $\gamma = 1/\sqrt{1 - v^2/c^2}$ is the Lorentz factor.

The electromagnetic fields are defined on a grid, and are evolved using Ampère's and Faraday's laws using charges and currents that are accumulated by summing the contributions from the macroparticles.

2.6.2 Simulation Parameters and Boundary Conditions

PIC simulations of reconnection, especially in three dimensions, are extremely computationally intensive. It is important that the simulation domain capture large scale dynamics $L \gg d_i$, $t \gg \Omega_{ci}^{-1}$ while also resolving electron scales $\Delta x \sim d_e$, $\Delta t \sim \Omega_{ce}^{-1}$. Numerical stability conditions for explicit codes are even more stringent, requiring that the Debye length λ_{De} and plasma frequency ω_{pe} also be resolved.

In a three-dimensional simulation, the computational expense scales as a large power of the proton to electron mass ratio: $(m_i/m_e)^{5/2}$. Artificial values of the mass ratio are typically used in order to reduce this computational expense. The value $m_i/m_e = 25$ is typically considered sufficient to maintain a minimum separation of scales between the two species.

Another way of reducing the computational expense is to use a ratio of the electron plasma frequency to the cyclotron frequency that is smaller than realistic values. This reduces the time resolution constraint while preserving cyclotron time scale physics (dynamics at the electron plasma frequency are typically not important for reconnection problems). For example, the simulations in this work use $\omega_{pe}/\Omega_{ce} = c/c_{Ae} = 3$, which is substantially smaller than a typical magnetotail value of ≈ 16 (based on $n = 1\,\mathrm{cm}^{-3}$ and $B = 20\,\mathrm{nT}$).

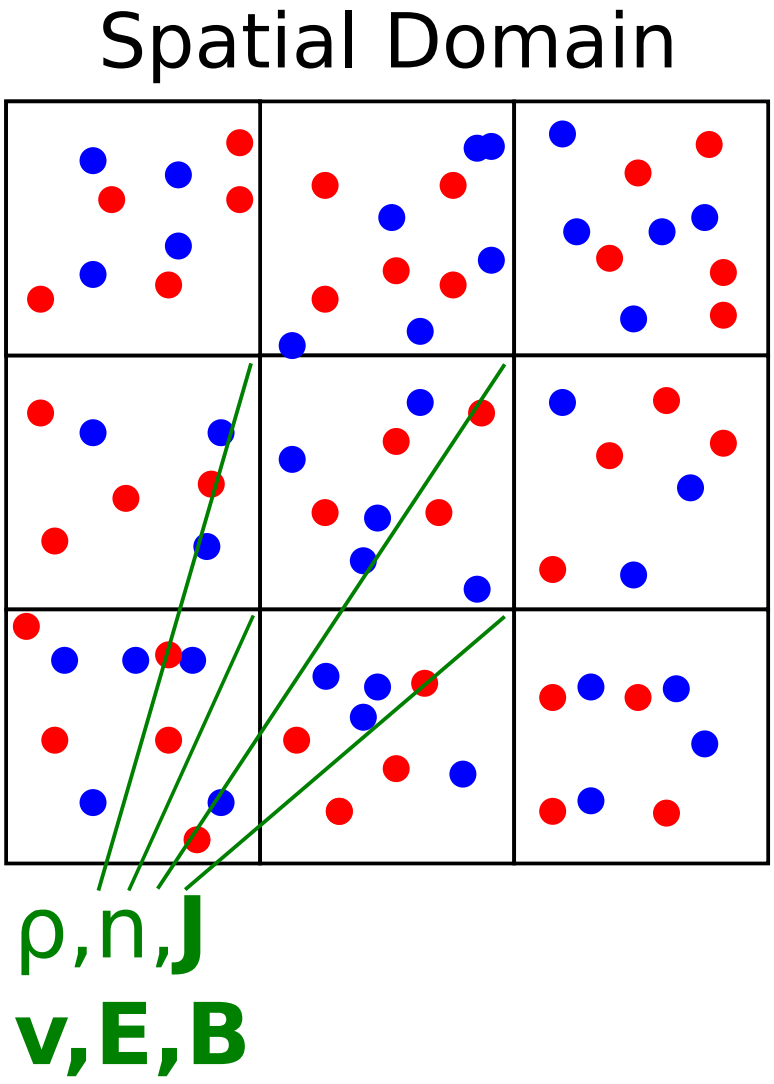

Figure 2.4: The Particle-in-Cell Method (PIC) method. Electromagnetic fields are defined on a grid. Representative 'macroparticles' are evolved using the Lorentz force law interpolated from the grid. Distribution function moments including charge and current are accumulated on the grid cells and used to evolve Maxwell's equations for the electromagnetic field.

In this simulations presented in this thesis, I will use periodic boundary conditions for all dimensions. Given that the reconnecting component of the magnetic field reverses across a current sheet, this requires that the initial condition contains two current sheets, so that magnetic field reverses twice. Though there are two current sheets, we will treat them independently as the systems of interest contain only a single sheet. There is a potential concern in that at late time, the current sheets can become strongly correlated so that eventually the separatrices and magnetic islands from neighboring sheets merge. However, all analysis will be carried out at times when the dynamics of the two sheets are uncorrelated.

Other boundary choices are possible. Conducting boundaries parallel to the reconnecting component of the field have often been used [13]. However, these boundary conditions suppress field line bending and therefore reduce the reconnection rate, especially in small systems. Open boundary conditions, where waves and particles may leave the system, have seen use in recent years [43, 44]. However, the small size of 3D PIC simulations is a serious problem. Energetic particles and magnetic structures such as islands are rapidly lost from the simulation domain, so that they no longer have an impact on the evolution. In most astrophysical systems, the relevant scale sizes are many orders of magnitude larger than what is possible in PIC, so that this is also a poor approximation. The periodic system is more appropriate in that it models an 'infinite' current sheet where there would be no such loss over the evolution time scales typically considered ($\sim 100\Omega_{ci}^{-1}$).

2.6.3 Current Sheet Initial Conditions

In modeling astrophysical systems, there are two typical initial conditions for a symmetric one-dimensional current sheet. The varying quantities for each configuration are depicated in Fig. 2.5. One is the Harris equilibrium, devised by E. G. Harris [45] where the current sheet is supported by plasma pressure:

$$B_x = B_0 \tanh(y/\lambda) \tag{2.28}$$

$$n = n_0 \operatorname{sech}^2(y/\lambda) \tag{2.29}$$

where B_x is the reconnecting component of the field and n is the plasma density. The electron and proton temperatures are chosen such that $n_0(T_e + T_i) = B_0^2/8\pi$ so that the total pressure is a constant.

In Harris' initial formulation, this is an exact kinetic equilibrium where the proton and electron distribution functions are Maxwellians with drift velocities proportional to their temperatures. The Harris equilibrium is typically modified to include a constant background density n_b and possibly a constant guide field B_z which preserve the fluid equilibrium (pressure balance). This initial condition is often used to model the magnetotail, where the current sheet population has a much higher temperature and density than the lobe (asymptotic) population, and the guide field is small.

The force-free configuration is another common initial condition used for modeling a current sheet. The name comes from the fact that the Lorentz force $|\mathbf{J} \times \mathbf{B}|$

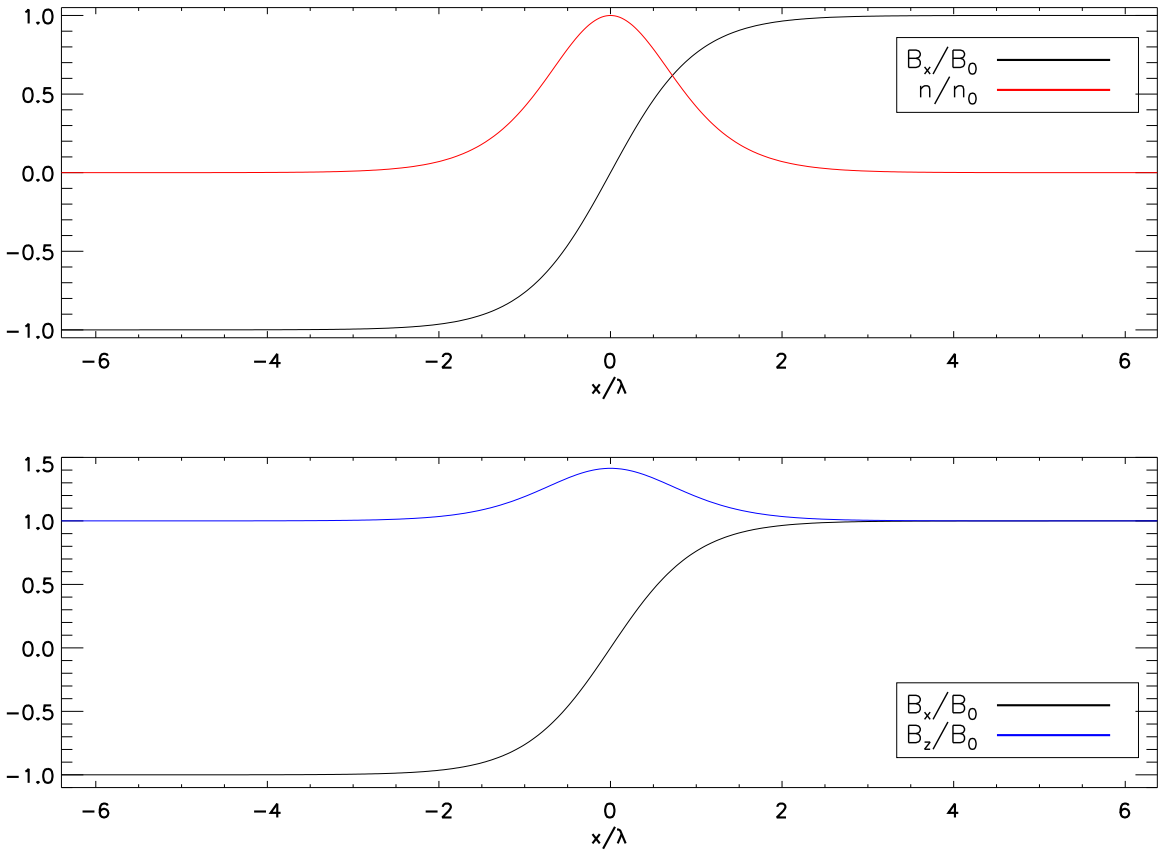

Figure 2.5: Varying quantities for current sheet equilibria. (Top) Harris configuration; the temperature and the guide field (not shown) are constant. (Bottom) Force-free configuration; the density and temperature (not shown) are constant.

$= 0$ so that $|\mathbf{B}| = const.$ Our implementation is given as follows:

$$B_x = B_{x0} \tanh(y/\lambda) \tag{2.30}$$

$$B_z = \sqrt{B_{z0}^2 + (B_{x0}^2 - B_x^2)} \tag{2.31}$$

The plasma pressure is constant. This configuration is well-suited for systems where the current sheet is supported by the magnetic field rather than the plasma pressure. This is a natural choice in low-β systems such as the solar corona.

Chapter 3: Particle Acceleration Mechanisms

In this chapter, I describe some of the important mechanisms for accelerating particles in magnetic reconnection. I begin by presenting a simple guiding-center model and proceed to describe the important mechanisms which arise. I first discuss the role of parallel electric fields, which can accelerate electrons very quickly, but are typically localized to small scales. I then describe betatron acceleration and argue that its role should be small in the systems considered in this thesis. I then discuss Fermi acceleration including its history, application to reconnection, and its relation to the curvature-drift term in the guiding-center model. I finally present a bulk equation which casts the three relevant particle energization mechanisms in terms of fluid moments.

3.1 Particle Acceleration in the Guiding-Center Approximation

In order to examine various effects contributing to electron energy evolution, consider a standard treatment of the guiding-center approximation given by Northrop [46]. The evolution of the energy ϵ of a single electron in the guiding-center

limit is given by:

$$\frac{d\epsilon}{dt} = (\mu/\gamma)\frac{\partial B}{\partial t} + q(v_\parallel \mathbf{b} + \mathbf{v}_c + \mathbf{v}_g) \cdot \mathbf{E} \tag{3.1}$$

where $\mathbf{b} = \mathbf{B}/|\mathbf{B}|$, $\mu = m_e\gamma^2 v_\perp^2/2B$ is the magnetic moment, γ is the relativistic Lorentz factor, $v_\parallel = \mathbf{v} \cdot \mathbf{b}$, and $\mathbf{v}_c$ and $\mathbf{v}_g$ are the curvature and grad-B drifts:

$$\mathbf{v}_c = \frac{v_\parallel^2 \mathbf{b}}{\Omega_{ce}} \times \boldsymbol{\kappa} \tag{3.2}$$

$$\mathbf{v}_g = \frac{v_\perp^2 \mathbf{b}}{2\Omega_{ce}} \times \frac{\nabla B}{B} \tag{3.3}$$

In Eqs. (3.2) and (3.3) the electron cyclotron frequency $\Omega_{ce} = eB/\gamma m_e c$, and the magnetic curvature is $\boldsymbol{\kappa} = \mathbf{b} \cdot \boldsymbol{\nabla}\mathbf{b}$.

Equation (3.1) may be rewritten in the following enlightening form:

$$\frac{d\epsilon}{dt} = qE_\parallel v_\parallel + \frac{\mu}{\gamma}\left(\frac{\partial B}{\partial t} + \mathbf{u}_{_E} \cdot \nabla B\right) + \gamma m_e v_\parallel^2 (\mathbf{u}_{_E} \cdot \boldsymbol{\kappa}) \tag{3.4}$$

Three distinct terms are apparent in this formulation. The first corresponds to acceleration by parallel electric fields $E_\parallel$. Parallel electric fields are difficult to sustain over large regions since they are typically shorted out by fast moving electrons. As a consequence they are typically localized to a scale of only a few Debye lengths. The second grouping of terms corresponds to betatron acceleration, associated with the conservation of the magnetic moment μ. When a charged particle experiences an adiabatic change in B, either by advection ($\mathbf{u_E}$) or a local change in the magnetic field strength, the perpendicular velocity evolves to compensate. Parallel motion of the particles in the absence of an electric field simply exchanges energy between

$\epsilon_\parallel$ and $\epsilon_\perp$ via the well-known magnetic mirror phenomenon and therefore does not change the particle energy. The final term corresponds to a type of Fermi acceleration due to reflection of charged particles from contracting field lines. The $\mathbf{u}_E \cdot \boldsymbol{\kappa}$ term shows that this occurs wherever magnetic fields are advected in the direction of the magnetic curvature, hence releasing tension. These terms will be addressed in turn in subsequent sections of this chapter.

These three terms accelerate particles in distinct ways. Both the first and third terms change the parallel energy. Parallel electric fields, which are directional, typically produce magnetic field-aligned beams. These beams can subsequently be thermalized through a variety of instabilities. The magnitude of Fermi acceleration is directly proportional to the parallel energy, and the process increases the parallel temperature directly (omitting transport processes, $d\epsilon/dt \propto \epsilon$ leads to an evolving temperature $dT/dt \propto T$). The betatron mechanism instead increases the perpendicular energy concurrent with an increase in the magnetic field. For a significant energy gain to be possible, this would typically require the particle to see a large increase in the magnetic field.

3.2 Parallel Electric Fields

An apparently straightforward means of accelerating particles in reconnection is via parallel electric fields. Acceleration by parallel electric fields has been explored in a number of studies [18, 47, 48]. However, parallel electric fields are typically localized to small regions, as electrons move quickly to short out the parallel electric

field.

Parallel electric fields can arise in the reconnection diffusion region in the presence of a guide field. As in the Sweet-Parker analysis presented in Section 2.3.1, we discuss a localized region with boundary conditions determined by the ideal plasma properties. In the presence of a guide field, only the in-plane component of the tension drives the reconnection outflow, and hence $v_{out} = c_{Ax}$. The inflow velocity is given by continuity: $v_{in} = (\delta/L)v_{out}$.

As in the Sweet-Parker picture, a constant electric field $E_z = -v_{in}B_{x0}/c$ supports the steady-state reconnection of the in-plane magnetic field B_{x0}. However, this field must be accompanied by in-plane components so that $\mathbf{E} + \mathbf{v}/c \times \mathbf{B} = 0$. In the inflow $E_{\|} = \mathbf{E}_x B_{0x} + E_z B_{0z} = 0$ so $E_x = -E_z B_{9z}/B_{0x}$. Similarly, along the outflow $E_y = -E_z B_{0z}/B_{0y}$. For B_{0z} very large, these in-plane fields are much larger than the reconnection electric field. These in-plane fields have odd symmetry across the x-line and therefore are small within the diffusion region where $E_{\|} \neq 0$. The typical transverse scale of the diffusion region for the case of a strong guide field is the electron-sound Larmor radius [49]

There are several other ways in which parallel electric fields can arise in the context of magnetic reconnection. For example, Egedal et al. [48] have examined 'pseudo-potential' wells near the X-line that develop as accelerated electrons leave the X-line and leave ions behind, generating parallel electric fields. However, these pseudopotentials are at most of the order $m_e c_{Ae}^2$, and hence do not significantly affect energetic particles $v_{\|} \gg c_{Ae}$. The role of any large-scale potential structure in particle acceleration remains uncertain because particles entering such a potential

and then leaving do not gain net energy. One of the goals of this dissertation is to clarify this point.

Another way in which parallel electric fields can arise is through streaming instabilities such as the Buneman instability [35, 50], which can form electron holes with strong localized electric fields. However, as with the pseudopotentials described above, these typically interact most strongly with thermal particles, as the potentials associated with these electron holes derive from the free energy of reconnection-produced electron beams, and are hence associated with bulk flow energies $v_{e\parallel} \sim c_{Ae}$. Hence these structures also do not seem likely to be efficient accelerators of energetic particles. Again, one of the goals of this dissertation is to clarify the role of turbulence versus the inductive electric field in heating and acceleration of electrons.

3.3 Betatron Acceleration

The betatron mechanism is a well-understood method of accelerating charged particles. In earth-based particle accelerators, this is accomplished by using the induced electric fields from a changing magnetic field in order to energize electrons traveling in a circular orbit.

In a plasma, the underlying physics is essentially identical. It is convenient to consider the non-relativistic magnetic moment $\mu = mv_\perp^2/2B = \epsilon_\perp/B$. If the temporal scales are much longer than the cyclotron period, then this is an adiabatic invariant. Hence the evolution of the perpendicular energy $\epsilon_\perp$ is associated with a

change in the magnetic field:

$$\frac{d\mu}{dt} = \frac{1}{B}\frac{d\epsilon_\perp}{dt} - \frac{\epsilon_\perp}{B^2}\frac{dB}{dt} = 0 \tag{3.5}$$

$$\frac{d\epsilon_\perp}{dt} = \frac{\epsilon_\perp}{B}\left(\frac{\partial}{\partial t} + \mathbf{v}\cdot\boldsymbol{\nabla}\right)B \tag{3.6}$$

where $\mathbf{v}$ is the velocity of the particle. The rapid gyromotion does not result in a net drift, and the parallel motion only transfers energy between the perpendicular and parallel components, and does not produce a net energization. Hence the net energy gain is given by:

$$\frac{d\epsilon}{dt} = \frac{\epsilon_\perp}{B}\left(\frac{\partial}{\partial t} + \mathbf{u_E}\cdot\boldsymbol{\nabla}\right)B \tag{3.7}$$

where $\mathbf{u_E}$ is the $\mathbf{E}\times\mathbf{B}$ velocity. In the guiding-center frame, this reduces to the partial time derivative. A finite $\partial B/\partial t$ corresponds to a finite curl of the electric field, which energizes the particle as it orbits the magnetic field line, in a manner analogous to that employed in particle acceleration.

Magnetic reconnection releases magnetic energy, and hence reduces the magnitude of the magnetic field. Hence it would not be expected that betatron acceleration would be very efficient, as it requires the particle to experience an increase in B in order to gain energy. However, the global topology change enabled by reconnection can result in betatron acceleration. One example is a 'dipolarization front' in the magnetotail, where the onset of reconnection allows stretched field lines to snap back toward the earth and into a region of larger magnetic field. Such global effects are not captured by the slab kinetic simulations employed in this thesis.

3.4 Fermi Acceleration

What is now known as Fermi acceleration was first proposed by E. Fermi in order to explain the origin of Cosmic Rays [28]. In the original formulation, Fermi proposed that charged particles could collide with randomly moving 'magnetic irregularities'. A head-on collision would increase the energy of the particle, a tail-on collision decrease the energy of the particle. Fermi argued that since the head-on collisions are more likely, there would be an average acceleration. The average gain in energy per collision would then be given by:

$$\delta\epsilon \propto (V/c)^2\epsilon \tag{3.8}$$

where ϵ is the energy of the particle and V is the velocity of the magnetic irregularity. He then assumed that energetic particles would have a finite lifetime, losing their energy via collisions with ambient particles. A simple equation for the evolution of the distribution $f \equiv f(\epsilon, t)$ of energetic particles is given by:

$$\frac{\partial f}{\partial t} + \frac{\partial}{\partial \epsilon}\left(\dot{\epsilon} f\right) = -\frac{f}{T}.$$

If the average time between interations with magnetic irregularities is τ, then $\dot{\epsilon} = \epsilon(V/c)^2/\tau$. If we assume no time variation ($\partial/\partial t = 0$) and take T to be the characteristic lifetime of the energetic particles, we arrive at:

$$\frac{\partial}{\partial \epsilon}\left(\alpha\epsilon f\right) = -\frac{f}{T}. \tag{3.9}$$

Where $\alpha = (V/c)^2/\tau$. The solution to 3.9 takes the form of a power law:

$$f(\epsilon) \propto \frac{1}{\epsilon^{1+(\alpha T)^{-1}}} \tag{3.10}$$

as is required in order to explain the Cosmic Ray spectrum.

Fermi's original idea was subsequently adapted to describe acceleration at astrophysical shocks. For any given shock there exist reference frames where the fluid flow (and any magnetic irregularities) converges toward the shock. Charged particles reflecting from these irregularities in the vicinity of the shock will always see the head-on type of collisions and will gain energy in a secular fashion. This type of Fermi acceleration is known as Diffusive Shock Acceleration, and is the leading current model for the acceleration of Galactic and Intergalactic cosmic rays.

3.4.1 Fermi Acceleration in Reconnection

Recent work by Drake et al. [51] has described a Fermi-type process which can occur inside magnetic islands during reconnection. In Fermi's original article, he described two types of collisions: type 'A' involving reflections from moving magnetic mirrors, and type 'B' involving reflection from a moving, curved field line. Fig. 3.1 illustrates the latter process adapated to a reconnecting system. In the reconnection picture, the curved field line is contracting away from an X-line with an Alfvénic outflow velocity.

The curved field line is moving rightward (here at the Alfvén velocity c_A) and a charged particle along the field line is moving leftward with a parallel velocity $v_x = -v_0$. In the reference frame of the field line, the particle begins with a velocity $v'_{x,i} = -v_0 - c_A$. The particle reflects elastically from the field line, so that its final velocity is $v'_{x,f} = v_0 + c_A$. Transforming back to the 'lab frame', we find that the

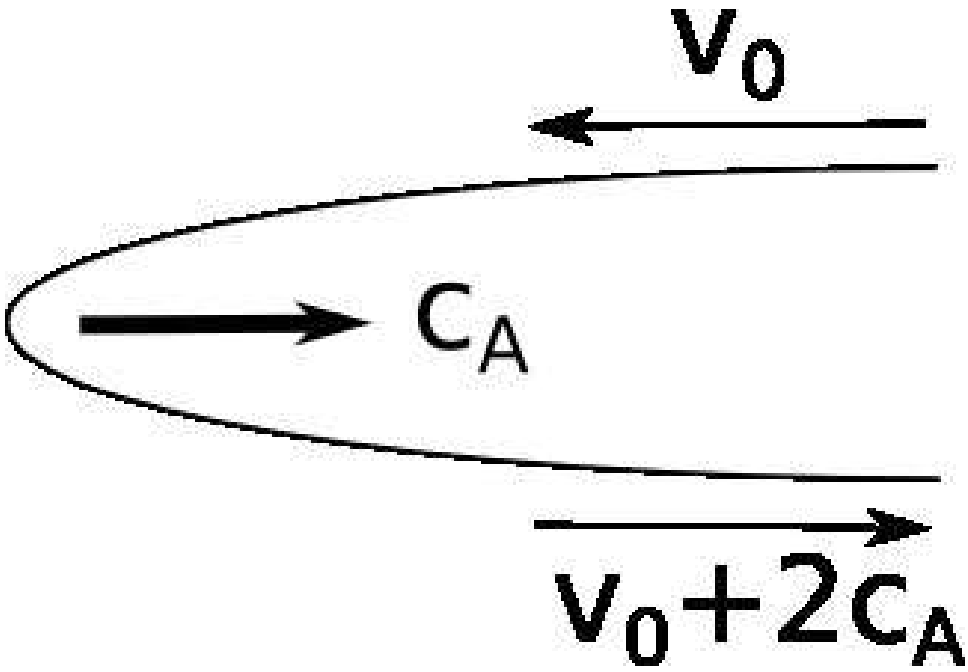

Figure 3.1: Cartoon diagram of a charged particle reflecting from a magnetic loop contracting at the Alfvén speed. The particle velocity increases by $2c_A$.

particle's final velocity is $v_0 + 2c_A$.

Magnetic reconnection typically generates magnetic islands, which can be pictured as elongated magnetic bubbles that are contracting at both ends. In such a situation, the particles are well-confined and, if sufficiently fast, can reflect many times from either end of the island. If the velocity of the particle is much greater than the Alfvèn speed (as is typically the case for electrons), then the energy gain per collision is $\Delta\epsilon \approx (mv)c_A$. The reflections occur with a frequency $\sim v/L$, so that:

$$\frac{d\epsilon}{dt} \sim m(v/L)(vc_A) \sim (c_A/L)\epsilon \tag{3.11}$$

Another way to describe why the energy increases relies on the conservation of the parallel action $J_\parallel = \int v_\parallel d\ell$. As the island contracts, the field lines become shorter. If the particles are circulating rapidly ($v \gg c_A$) then this directly implies that $v_\parallel$ must increase.

The acceleration of a particle in the presence of a contracting field line can also be calculated analytically. Begin by calculating the evolution of the parallel velocity:

$$\frac{dv_\parallel}{dt} = \frac{d}{dt}(\mathbf{v}\cdot\mathbf{b}) \tag{3.12}$$

$$= \mathbf{b}\cdot\frac{d\mathbf{v}}{dt} + \mathbf{v}\cdot\frac{d\mathbf{b}}{dt} \tag{3.13}$$

$$= \frac{q}{m}E_\parallel + \mathbf{v}\cdot(\mathbf{v}\cdot\boldsymbol{\nabla})\mathbf{b} + \mathbf{v}\cdot\frac{\partial\mathbf{b}}{\partial t} \tag{3.14}$$

where we have used the Newton-Lorenz equation for $d\mathbf{v}/dt$. For simplicity, we assume $\partial\mathbf{b}/\partial t = 0$, which is typically a good approximation for hot electrons (the result is essentially the same without this assumption, but the deriviation and interpretation are somewhat more complicated). We can then apply gyro-averaging

$\langle\,\rangle$ to find a tractable expression for $\mathbf{vv}$:

$$\langle \mathbf{vv} \rangle \approx (\mathbf{I} - \mathbf{bb})\frac{v_\perp^2}{2} + \mathbf{v}_\parallel \mathbf{v}_\parallel + \mathbf{u_E} \mathbf{v}_\parallel + \mathbf{v}_\parallel \mathbf{u_E} \tag{3.15}$$

which neglects higher order terms such as the curvature and grad-B drifts. Dyadics with leading $\mathbf{b}$ vanish when dotted into $\boldsymbol{\nabla}\mathbf{b}$, yielding:

$$\left\langle \frac{dv_\parallel}{dt} \right\rangle = \frac{q}{m} \langle E_\parallel \rangle + \langle \mathbf{vv} \rangle : \boldsymbol{\nabla}\mathbf{b} \tag{3.16}$$

$$= \frac{q}{m} \langle E_\parallel \rangle + \frac{v_\perp^2}{2} \boldsymbol{\nabla} \cdot \mathbf{b} + \mathbf{u_E} \cdot (v_\parallel \nabla_\parallel)\mathbf{b} \tag{3.17}$$

$$= \frac{q}{m} \langle E_\parallel \rangle - \frac{v_\perp^2}{2B} \nabla_\parallel B + \mathbf{u_E} \cdot (v_\parallel \boldsymbol{\kappa}) \tag{3.18}$$

The first term is the familiar parallel electric field term. The second corresponds to the mirror force $\mu \boldsymbol{\nabla}_\parallel B$ which transfers energy between the parallel and perpendicular components of the velocity. The last term corresponds to reflection from contracting field lines. Neglecting parallel electric fields and the mirror force, the evolution of the parallel kinetic energy $\epsilon_\parallel$ due to this term is then given by:

$$\frac{d}{dt}\left(\frac{m v_\parallel^2}{2}\right) = m v_\parallel^2 \mathbf{u_E} \cdot \boldsymbol{\kappa} \tag{3.19}$$

$$\frac{d\epsilon_\parallel}{dt} = 2\epsilon_\parallel \frac{c\mathbf{E} \times \mathbf{B}}{B^2} \cdot \boldsymbol{\kappa} \tag{3.20}$$

$$= q\mathbf{E} \cdot \left(\frac{2c\epsilon_\parallel}{qB} \frac{\mathbf{B} \times \boldsymbol{\kappa}}{B}\right) \tag{3.21}$$

$$= q\mathbf{E} \cdot \mathbf{v_c} \tag{3.22}$$

where $\mathbf{v_c}$ is the curvature drift.

The expression in Eq. 3.18 may be used to evaluate the increase in particle velocity as it reflects from a contracting field line in a reconnection exhaust (neglecting

the other two terms):

$$\Delta v_{\parallel} = \int_1^2 \frac{dv_{\parallel}}{dt} dt \tag{3.23}$$

$$= \int_1^2 v_{\parallel} (\mathbf{u_E} \cdot \boldsymbol{\kappa}) \frac{d\ell}{v_{\parallel}} \tag{3.24}$$

$$= \int_1^2 \mathbf{u_E} \cdot (\mathbf{b} \cdot \boldsymbol{\nabla}) \mathbf{b} \, d\ell \tag{3.25}$$

We may replace $\mathbf{u_E}$ with the reconnection outflow velocity $\mathbf{u} = \mathbf{u_E} + u_{\parallel}\mathbf{b}$ as $\mathbf{b} \cdot \boldsymbol{\kappa} = 0$. Since $\mathbf{u}$ is roughly constant throughout the reconnection outflow, we may then move it outside of the integral:

$$\Delta v_{\parallel} = \mathbf{u} \cdot \int_1^2 \frac{d\mathbf{b}}{d\ell} \, d\ell = \mathbf{u} \cdot (\mathbf{b}_2 - \mathbf{b}_1) \tag{3.26}$$

Assuming an outflow velocity $u = c_A \hat{\mathbf{x}}$ and antiparallel magnetic fields $\mathbf{b}_2 - \mathbf{b}_1 = 2\hat{\mathbf{x}}$, we arrive at the result $\Delta v_{\parallel} = 2c_A$. This is consistent with the cartoon picture discussed previously (Fig. 3.1).

3.5 Bulk Acceleration Equations

If we sum over all the particles in a local region (applying $\int f \, d^3\mathbf{v}$), Equation 3.1 becomes:

$$\frac{dU}{dt} = \frac{\beta_{\perp}}{2} \frac{\partial}{\partial t} \left(\frac{B^2}{8\pi} \right) + \mathbf{E} \cdot \left[\mathbf{J}_{\parallel} + \left(\frac{\beta_{\parallel}}{2} + \frac{u_{\parallel}^2}{c_{Ae}^2} \right) \frac{c}{4\pi} \mathbf{B} \times \boldsymbol{\kappa} + \frac{\beta_{\perp}}{2} \frac{c}{4\pi} \mathbf{B} \times \frac{\nabla B}{B} \right] \tag{3.27}$$

which may be rewritten as:

$$\frac{dU}{dt} = E_{\parallel} J_{\parallel} + \frac{p_{\perp}}{B} \left(\frac{\partial B}{\partial t} + \mathbf{u}_{_E} \cdot \boldsymbol{\nabla} B \right) + (p_{\parallel} + m_e n u_{\parallel}^2) \mathbf{u}_{_E} \cdot \boldsymbol{\kappa} \tag{3.28}$$

where U is the total kinetic energy, u_E is the E-cross-B drift, c_{Ae} is the electron Alfvén velocity, and $u_\parallel$ is the bulk velocity parallel to the magnetic field. The parallel and perpendicular pressures are $p_\parallel$ and $p_\perp$, respectively; n is the electron density, $\beta_\parallel = 8\pi p_\parallel / B^2$, and $\beta_\perp = 8\pi p_\perp / B^2$. It is worth noting here that the equations above are not specific to electrons, but will apply to any species for which the guiding-center approximation is valid. This formulation is useful as it expresses energy gain in terms of fluid moments which are frequently used diagnostics for kinetic PIC simulations. Energization by parallel electric fields is represented in the first term, betatron acceleration in the second, and curvature-drift or Fermi acceleration is expressed in the third.

Chapter 4: Electron Acceleration in Two-Dimensional Systems

4.1 Introduction

In this chapter, we discuss electron energization in two-dimensional kinetic simulations of magnetic reconnection. In section 4.2, we present the set of simulations that will be explored in this chapter. We then discuss electron heating and the relative importance of different energization mechanisms in section 4.3. In section 4.4 we examine superthermal electron production as revealed by energy and momentum spectra. We then present results from simulations with a larger mass ratio ($m_i/m_e = 100$), and finally discuss the relevance of these results for astrophysical contexts in section 4.6.

4.2 Simulations

We explore particle heating via simulations using the particle-in-cell (PIC) code `p3d` [42]. Particle trajectories are calculated using the relativistic Newton-Lorentz equations, and the electromagnetic fields are advanced using Maxwell's equations. The initial condition consists of a uniform guide field B_z superimposed

on a double-Harris equilibrium [45]. The magnetic field configuration is:

$$B_x = B_0 \left[\tanh\left(\frac{y - L_y/4}{w_0} \right) - \tanh\left(\frac{y - 3L_y/4}{w_0} \right) - 1 \right] \tag{4.1}$$

where B_0 is the asymptotic reconnecting field, w_0 is the current sheet half-width and L_y is the length of the computational domain in the y-direction. The density consists of two populations, a drifting population with density:

$$n = n_0 \left[\mathrm{sech}^2\left(\frac{y - L_y/4}{w_0} \right) + \mathrm{sech}^2\left(\frac{y - 3L_y/4}{w_0} \right) \right] \tag{4.2}$$

that carries the current and a uniform background with density $0.2n_0$.

We use an artificial mass ratio $m_i/m_e = 25$ and speed of light $c = 15c_A$ where m_i and m_e are the electron mass, c_A is the Alfvén velocity based on B_0 and n_0. These choices allow for sufficient separation of scales (between proton and electron spatial scales and electromagnetic and particle time scales, respectively) while significantly reducing the computational expense of the simulation. Lengths in our simulation are normalized to the ion skin depth $d_i = c/\omega_{pi}$ and times are normalized to the inverse ion cyclotron frequency, Ω_{ci}^{-1}. The initial temperature of all species is $0.25 m_i c_A^2$ for both background and the current sheet populations. The current sheet half-thickness is set to $w_0 = 0.25 d_i$ so that reconnection will onset quickly. The grid scale is $\Delta = d_e/4 \approx 0.94\lambda_D$ where $d_e = c/\omega_{pe}$ is the electron inertial length and λ_D is the Debye length. We use periodic boundary conditions in both directions.

The goal of the present chapter is to explore the mechanisms for particle acceleration using the expression for electron energy gain in Eq. (3.28). Since this equation is valid only for adiabatic motion, we limit our computations to systems

with a non-zero initial guide field. It was shown previously that electrons are magnetized in reconnecting systems with guide field exceeding $0.1B_0$ [52]. In this paper we therefore focus on two simulations with non-zero guide fields both with dimensions $L_x \times L_y = 204.8 \times 102.4$. Simulation 'A' has $B_z = 0.2B_0$ and 'B' has $B_z = 1.0B_0$. We note that although our simulations contain two current sheets, we will often present results from only the upper current sheet. In all cases the other sheet exhibits similar behavior. We will then present energy spectra from two larger simulations with dimensions $L_x \times L_y = 409.6 \times 204.8$ and $L_x \times L_y = 819.2 \times 409.6$, each with a guide field $B_z = 1.0B_0$.

4.3 2D Simulation Results: Electron Heating

Reconnection develops rapidly from the particle noise inherent in the PIC formulation. Figure 4.1 shows the evolution of the electron out-of-plane current density in simulation A. The tearing instability generates many magnetic islands on each current layer that continually grow and merge due to reconnection. We halt the simulation when the islands on the two current layers begin to interact, here at $t \approx 150$. Figures 4.2 and 4.3 display the parallel and perpendicular electron temperatures in simulations A and B early and late in the simulation. In simulation A the parallel electron temperature increases substantially within the exhausts downstream of the X-lines and within the developing magnetic islands. The perpendicular temperature increment is strongest in localized regions in the cores of magnetic islands. In contrast, $T_{e\parallel}$ significantly exceeds $T_{e\perp}$ throughout the duration of simulation B.

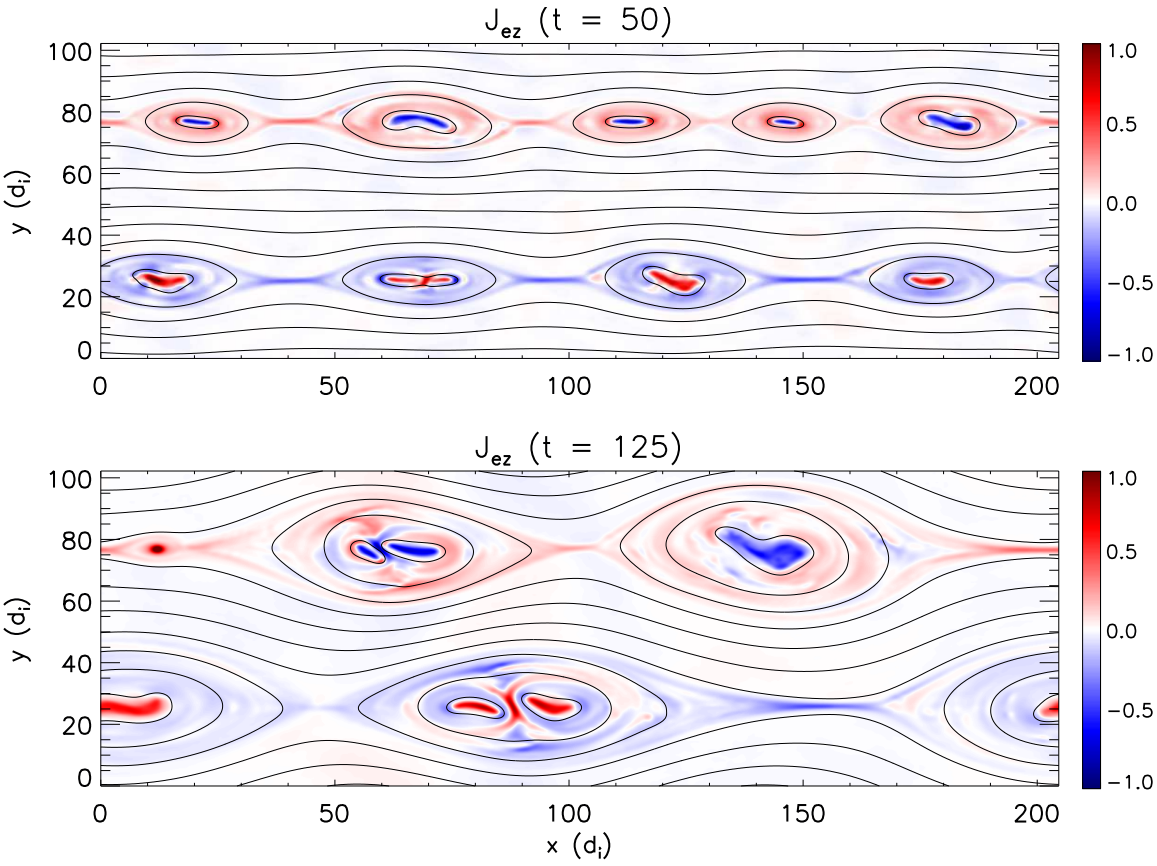

Figure 4.1: Out-of plane electron current density in simulation A at $t\Omega_{ci} = 50$ (top) and $t\Omega_{ci} = 125$ (bottom). Reconnection generates many islands which merge until they approach the system size.

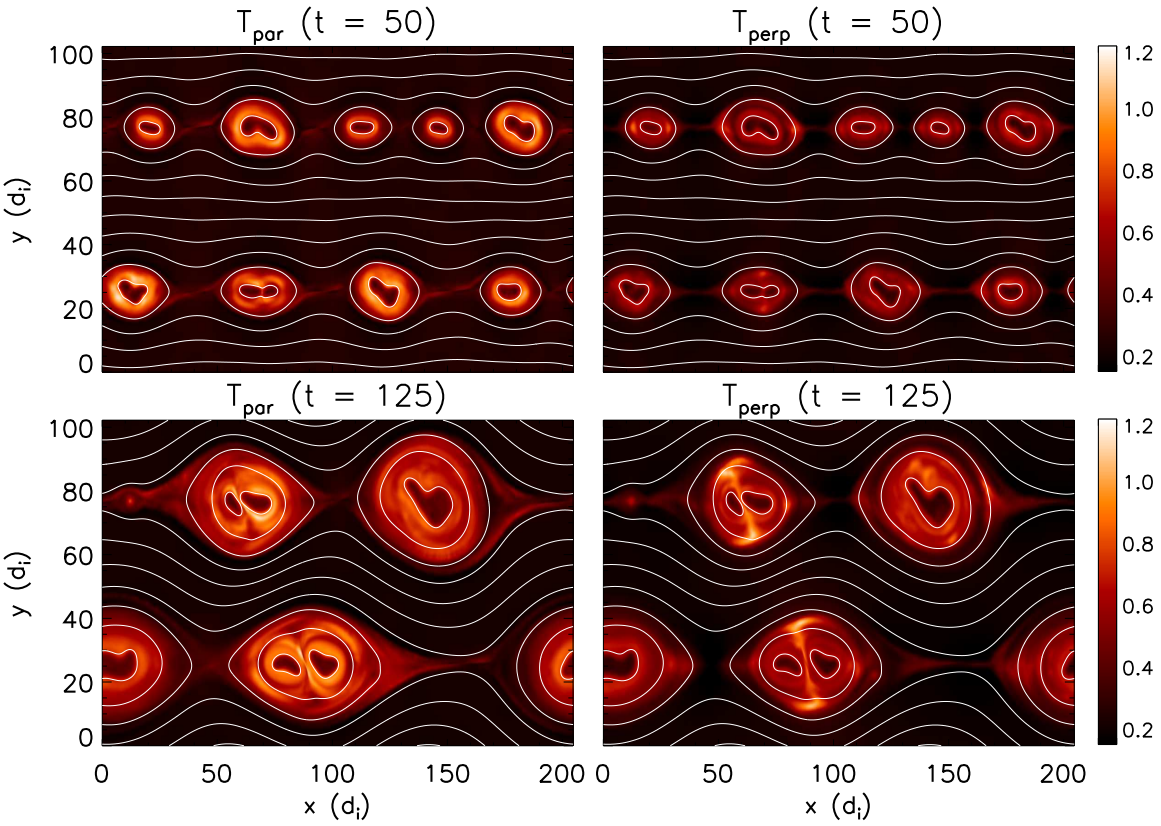

Figure 4.2: Parallel and perpendicular electron temperature from a simulation with a guide field of 0.2 (simulation A) at $t\Omega_{ci} = 50$ (top) and $t\Omega_{ci} = 125$ (bottom).

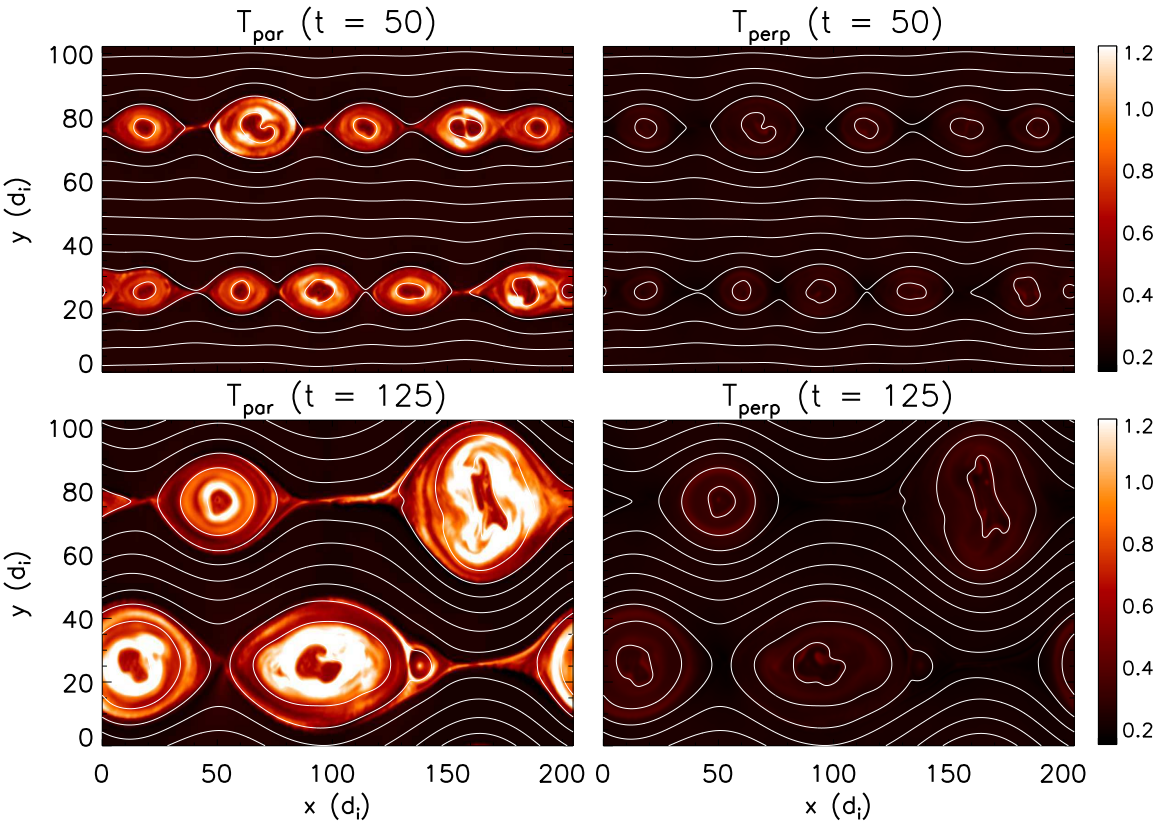

Figure 4.3: Parallel and perpendicular temperatures from a simulation with a guide field of $1.0B_0$ (simulation B) at $t\Omega_{ci} = 50$ (top) and $t\Omega_{ci} = 125$ (bottom).

Figures 4.4 and 4.5 show the contributions of the various terms in Eq. (3.28) in the upper current sheet in simulations A and B. At a given time each term in Eq. (3.28) was calculated at each grid point and then integrated over space to give the displayed curves. Some smoothing was performed to reduce the noise in the calculations but the results shown are insensitive to its details. The sum of heating terms on the right-hand side of Eq. (3.28) is given by the dashed black line, and should be compared to the solid black line which represents the total measured electron heating. To the extent that the two match, Eq. (3.28) represents a valid description of the system. The discrepancy at early time is due to the small initial size of the islands (which makes the guiding-center approach less accurate). Sharp, small-scale gradients that develop during island mergers may be a source of additional discrepancies.

In Fig. 4.4, which corresponds to simulation A, the curvature-drift term is the dominant source of heating and $E_\parallel J_\parallel$ is negligible. The grad-B and $\partial B/\partial t$ terms are also negligible and result in net cooling. This is because magnetic reconnection releases magnetic energy and therefore reduces the magnitude of B. Because of μ conservation electrons therefore on average lose energy in the perpendicular direction. By contrast, Fig. 4.5 shows that in simulation B the curvature-drift and $E_\parallel J_\parallel$ terms are comparable, while the other terms are negligible. The increased importance of the heating from the parallel electric field in the guide field unity case is because of the long current layers that develop in this case compared with those in the case of the weak guide field. Both simulations exhibit quasi-periodic heating which is largely due to island mergers. This can be seen by comparing times $t = 50$

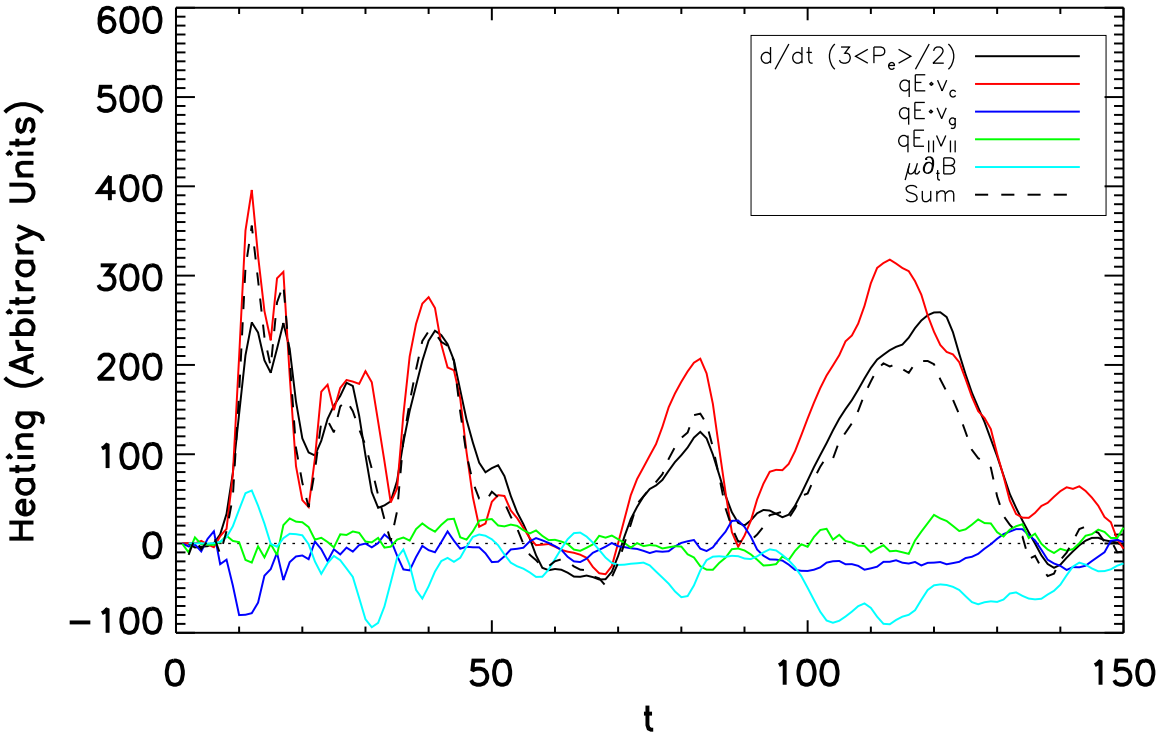

Figure 4.4: From a simulation with a guide field of $0.2B_0$ in black the electron heating integrated over the upper current layer versus time. From Eq. (3.28) the heating from the parallel electric field (green), the curvature drift (red), the gradient B drift (blue), induction (cyan) and the sum (dashed black) of all of the heating terms in Eq. (3.28). The curvature drift term, which describes Fermi reflection, dominates.

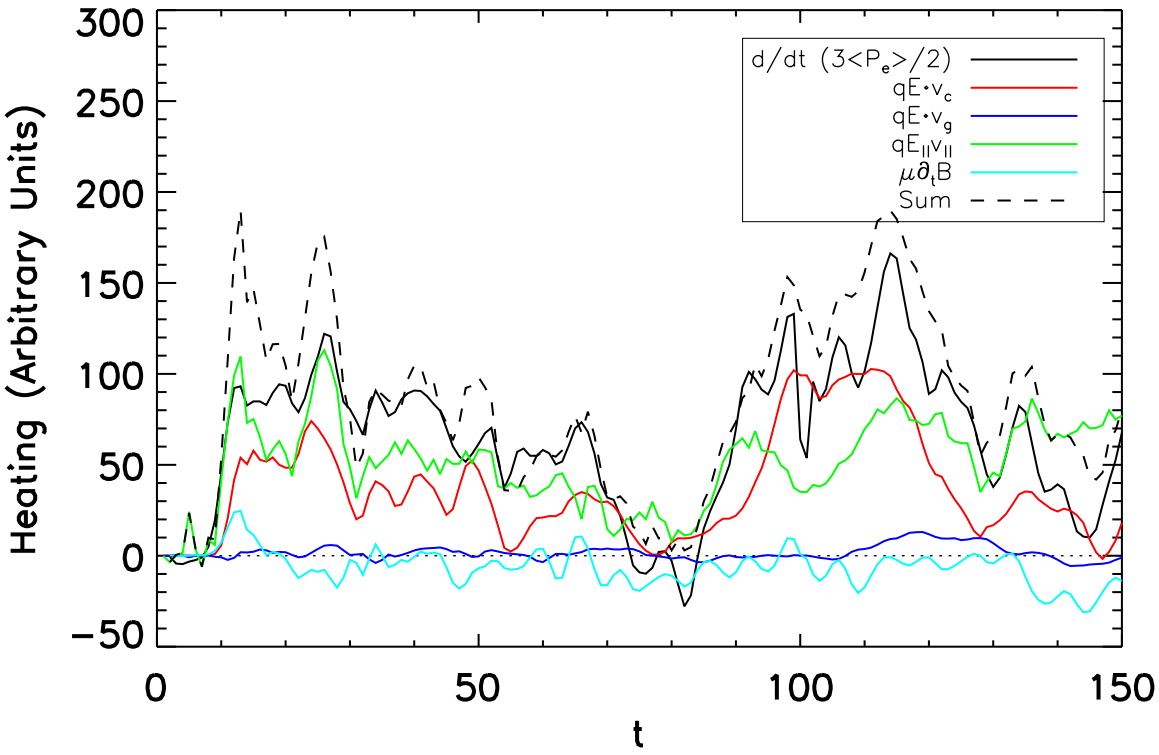

Figure 4.5: From a simulation with a guide field of $1.0B_0$ in black the electron heating integrated over the upper current layer versus time. Other heating terms as in Fig. 4.4. In contrast with the case of the weak guide field in Fig. 4.4, the curvature and $E_{\|}$ terms are comparable in magnitude.

and $t = 80$ in simulation A: the former exhibits only modest heating while the latter exhibits strong heating. Figure 4.8 (discussed further below) reveals that at $t = 80$ two islands are merging, which causes a burst of reconnection at the rightmost X-line in the system. In contrast, reconnection is proceeding in the normal fashion at $t = 50$.

Figures 4.6 and 4.7 show the spatial distribution of the curvature and $E_\parallel J_\parallel$ terms for simulation A at $t = 120$ and B at $t = 125$, respectively. As expected, the curvature-driven heating is primarily located in the reconnection exhaust regions and at the ends of the islands. Heating and cooling in the island cores are due to turbulent 'sloshing' of plasma inside the island. We show later that there is little net heating from this behavior. The $E_\parallel J_\parallel$ term is localized near the X-lines in both figures. The patchy regions of alternating heating and cooling throughout the islands, which is associated with electron holes [35, 50], does not on average produce much electron heating (shown later). Note the different color scales in the two plots in Fig. 4.6: the maximum intensity of the heating by $E_\parallel$ is much smaller than that of the curvature drift, consistent with its relatively small contribution to electron heating shown in Fig. 4.4.

The patchy nature of the $E_\parallel J_\parallel$ term makes the interpretation of this data difficult. It is not obvious, for example, whether the heating due to $E_\parallel$ around the X-line or due to the electrons holes dominates. As a further diagnostic, we therefore

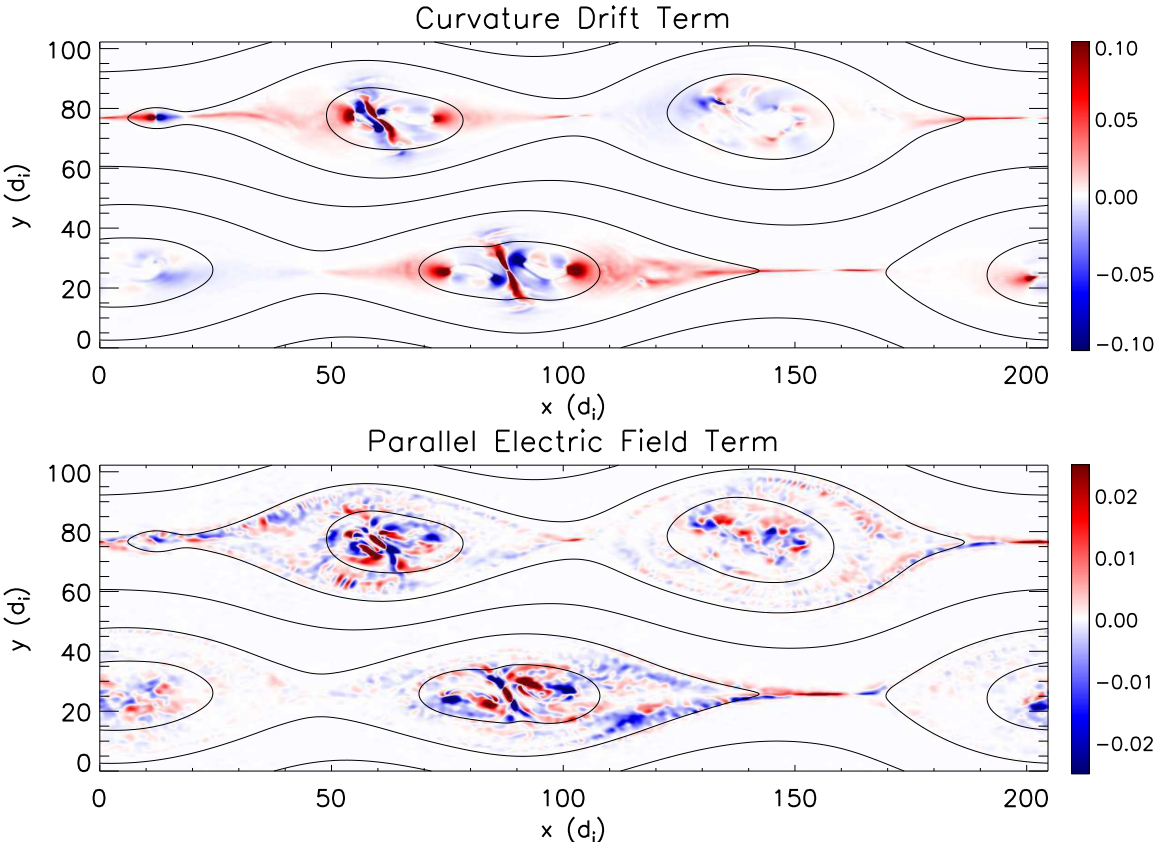

Figure 4.6: The distribution of electron heating for a guide field of $0.2B_0$ at $t = 125\Omega_{ci}^{-1}$ from the curvature (top) and the parallel electric field (bottom). Note the different color tables. The most intense heating occurs in the reconnection exhausts and at the ends of the islands from Fermi reflection.

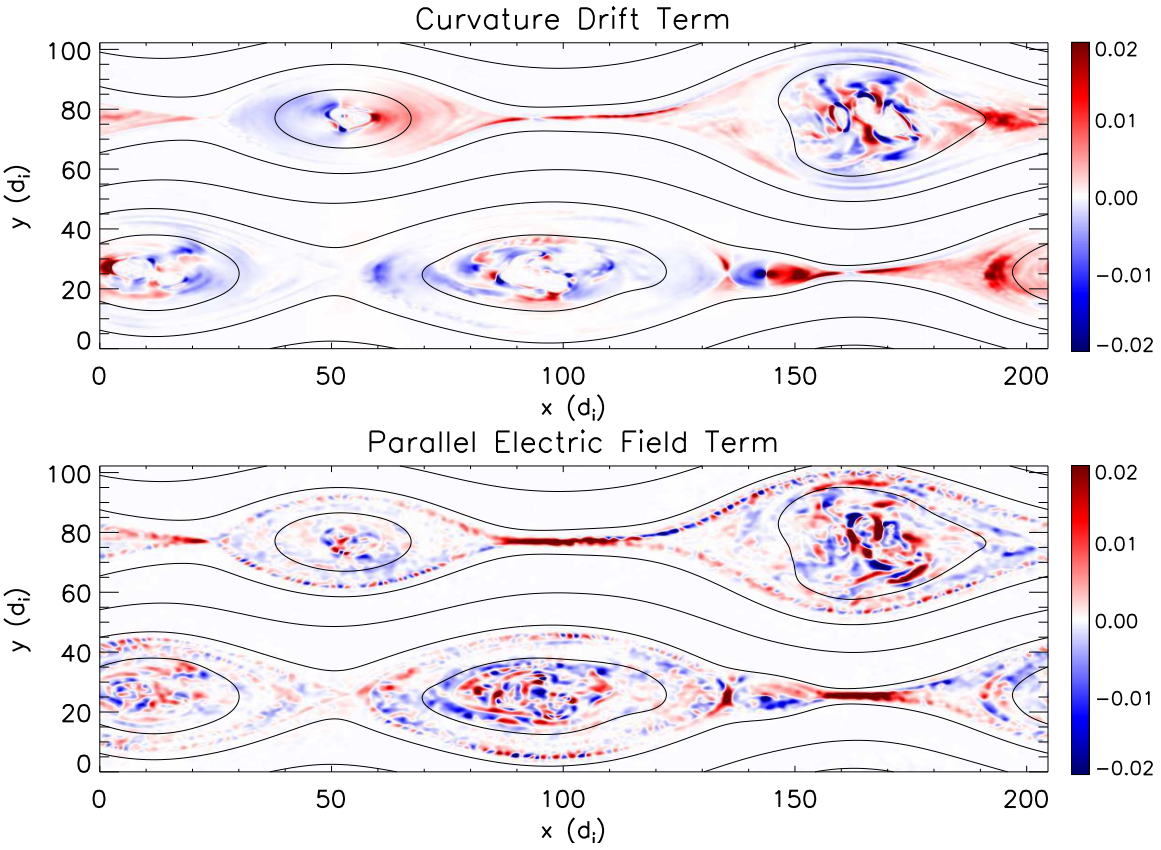

Figure 4.7: The distribution of electron heating for a guide field of $1.0B_0$ at $t = 120\Omega_{ci}^{-1}$ from the curvature (top) and the parallel electric field (bottom). Note that the color tables are the same. The current layers, where the heating from the parallel electric field is most intense, are much longer than in the case of a small guide field,

calculate the quantity:

$$\Xi(x) = \int_0^x dx' \int \mathcal{U}(x', y) dy \tag{4.3}$$

where $\mathcal{U}$ is a heating term, the y-integral is taken over the half of the box containing the current layer (varying the bounds of integration does not significantly affect the result). The slope $d\Xi(x)/dx = \int \mathcal{U}(x, y) dy$ yields the heating at a given x.

Figure 4.8 shows Ξ for the curvature-drift term in simulation A at two different times, corresponding to a temporal minimum in the curvature-drift heating ($t = 50$) and a temporal maximum ($t = 80$). The merger of two islands near $X \approx 160$ drives acceleration at the X-line in the far right of the simulation. The resulting island has a larger aspect ratio, (length x compared to width y) so that freshly reconnected field lines experience a greater tension force around the far right X-line. This enhances the rate of electron heating in the exhausts around this X-line. The plot of Ξ also reveals that the heating and cooling in island cores results in little net heating, as can be seen for example inside the island at $x \sim 165$ at $t = 80$.

Figure 4.9 shows Ξ for $E_\parallel J_\parallel$ at $t = 100$ from simulation B. The dominant heating occurs near the primary X-lines at $x \sim 30$ and 100 as well as the secondary X-lines (due to island mergers) at $x \sim 150$ and 190. Inside the islands, there is net cooling. Many of the small scale fluctuations in the $E_\parallel J_\parallel$ term correspond with electron holes, which are driven by electron beams generated near the X-line [35]. Because they tend to appear as bipolar structures in the heating term, they produce little net heating.

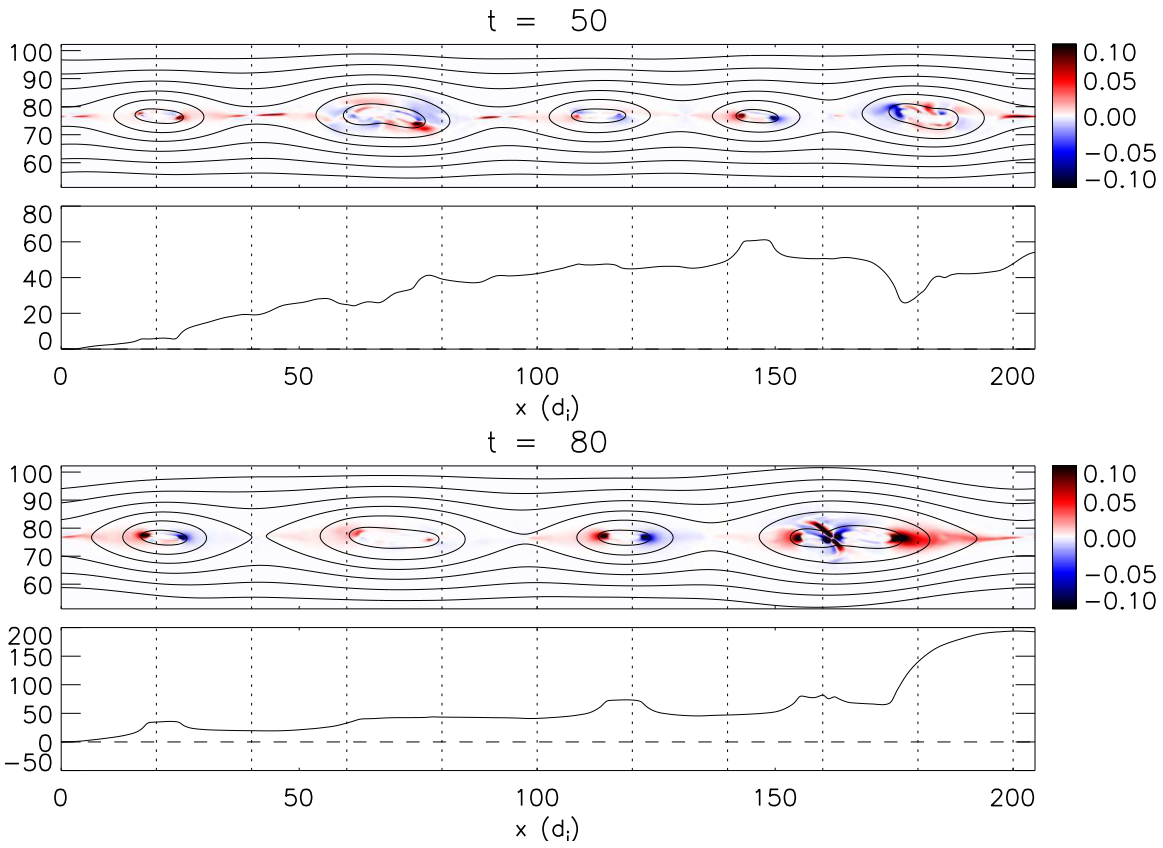

Figure 4.8: Plots of the heating from the curvature-drift and its spatially integrated contribution Ξ (see Eq. (4.3)) from the weak guide field simulation at $t = 50\Omega_{ci}^{-1}$ and $80\Omega_{ci}^{-1}$. For each time, the top half shows the spatial distribution and the bottom half shows its integrated contribution Ξ.

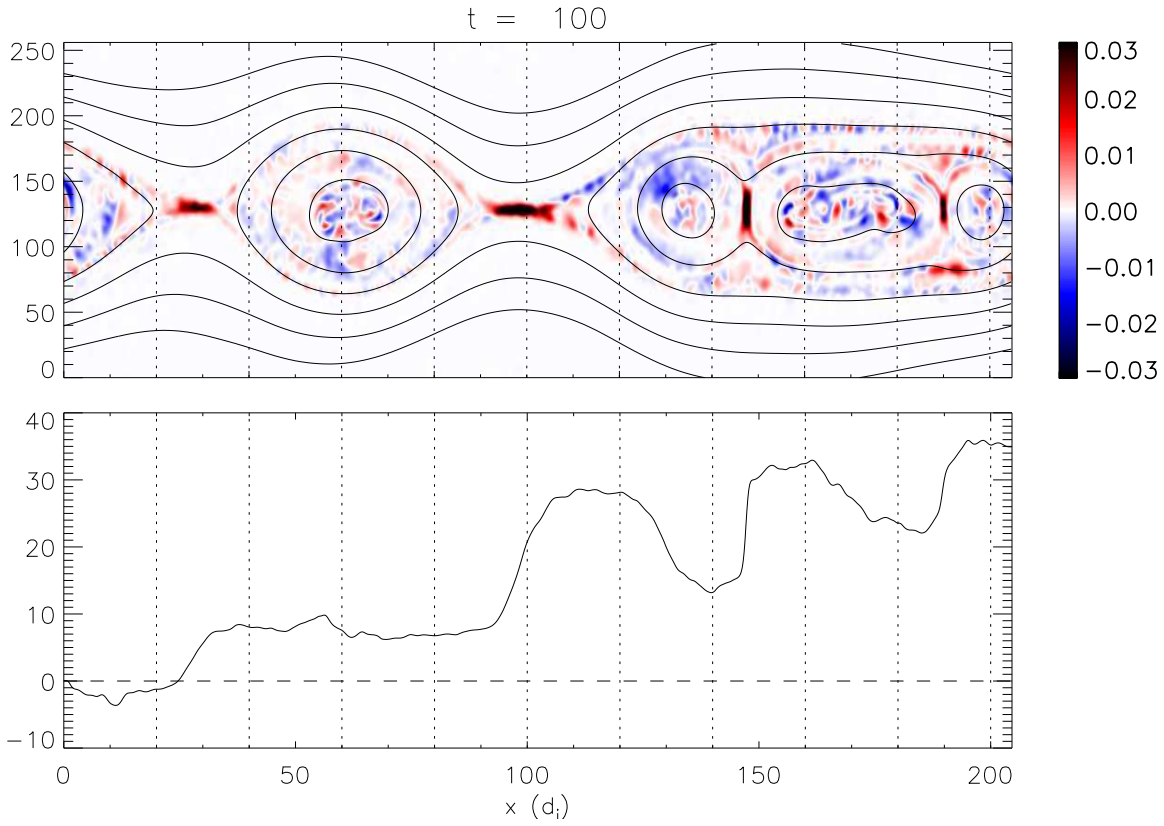

Figure 4.9: The spatial distribution of the rate of electron heating due to $E_{\parallel}$ at $t = 100\Omega_{ci}^{-1}$ from the strong guide field simulation (above) and its spatially integrated value Ξ. The dominant heating is from the current layers around the X-lines, while the contribution from electron holes in the islands appears to cause electron cooling.

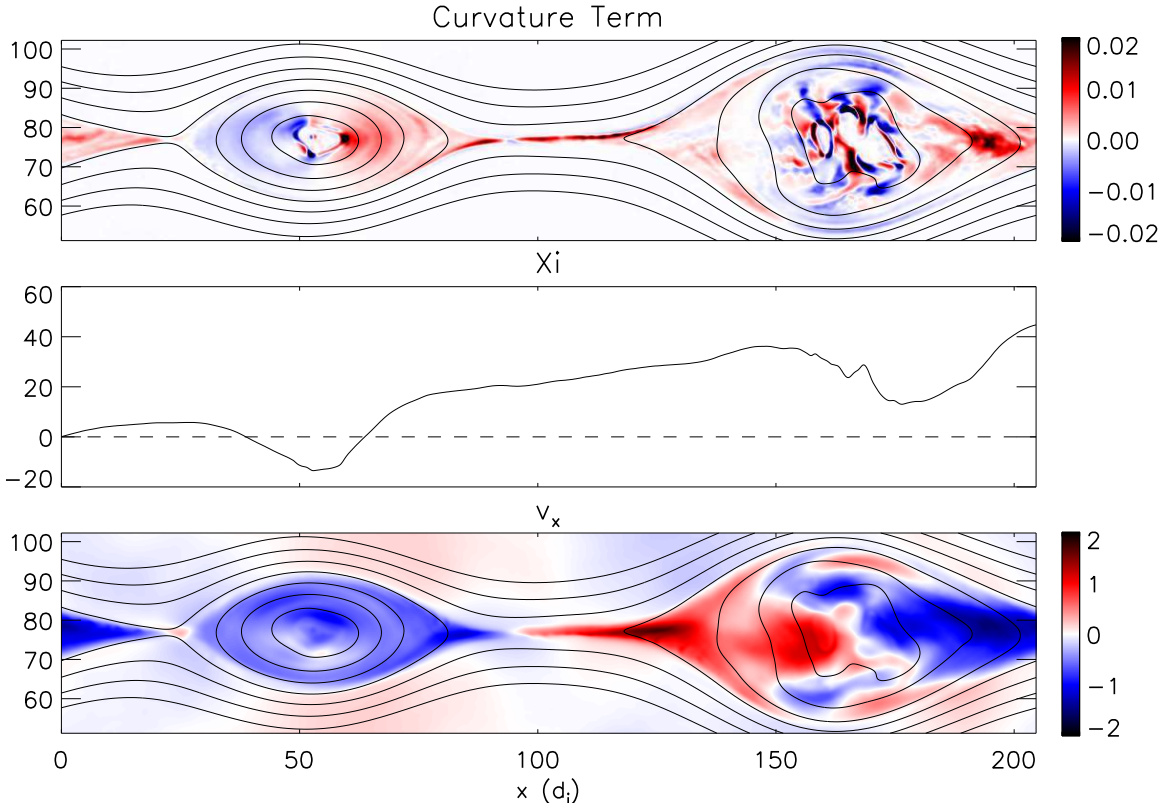

Figure 4.10: The effect of island motion on heating from the curvature drift from the strong guide field simulation at $t = 120\Omega_{ci}^{-1}$. The top panel shows the heating from the curvature drift, the middle panel shows its spatially integrated contribution Ξ, and the bottom panel shows the horizontal bulk flow v_x.

A number of the islands exhibit dipolar heating: the curvature term makes positive and negative contributions (red and blue) at the opposite ends of an island. Figure 4.10 exhibits this behavior. The island on the right drives heating due to Fermi reflection at both ends, and the plot of v_x shows large inward flows indicating island contraction. By contrast, the island on the left has dipolar heating. The entire island is moving in the $-x$ direction. In the simulation frame, particles see receding field lines at the left end of the island and lose energy in a reflection. Equivalently, $\mathbf{u}_{_E} \cdot \boldsymbol{\kappa} < 0$. However, the magnitude of the velocity at the right end is greater than that at the left, so the cooling at the left end is more than offset by the heating at the right: Ξ shows that the total heating across the island is positive. This is ultimately an issue of frame-dependence: in the frame of the island, both ends are contracting towards the center so that $\mathbf{u}_{_E} \cdot \boldsymbol{\kappa} > 0$.

4.4 Simulation Results: Electron Spectra

During reconnection with a strong guide field, which is expected to be the generic regime in most space and astrophysical systems, the dominant mechanisms for electron acceleration are the parallel electric field and Fermi reflection associated with the curvature drift, both of which accelerate electrons parallel to the local magnetic field. An important question, therefore, is whether the energetic component of the spectrum exhibits the strong anisotropy that is reflected in the moments $T_\parallel$ and $T_\perp$ in Fig. 4.3. Figure 4.11 shows electron spectra for the momenta parallel and perpendicular to the magnetic field. These spectra are taken from a simu-

lation with the same initial conditions as in simulation B but in a larger domain $L_x \times L_y = 819.2 \times 409.6$ carried out to $t = 400$. The larger simulation produces much better statistics in the particle spectra compared with simulation B shown earlier. In the parallel momentum a clear nonthermal tail develops by $t = 50$ and continues to strengthen until the end of the simulation. The perpendicular momentum also develops a nonthermal tail, but with an intensity that is smaller by more than two orders of magnitude. It is hence clear that the dominant nonthermal acceleration occurs in the parallel component and the anisotropy survives over long periods of time as the simulation develops. An important question is what mechanism causes the perpendicular heating of energetic electrons. If the magnetic moment were exactly preserved, electrons with such high values of $v_\perp$ would not be produced because the magnetic field B is not large enough anywhere. Therefore the increase in the perpendicular spectrum must arise from scattering either because of non-adiabatic behavior in the narrow boundary layers that develop as a result of reconnection or because of the development of an instability directly driven by the anisotropy.

The distribution of the electron magnetic moment $\mu = mv_\perp^2/2B$ for simulations A and B is shown in Fig. 4.12. It is clear that μ is very well conserved in simulation B, especially at low energies $\mu < 0.1$ where the electrons remain adiabatic in the presence of the strong guide field $B_z = B_0$. For simulation A with $B_z = 0.2B_0$, there is a drop of about 10% at the lowest energies, indicating that there is scattering into higher μ. This further suggests that the greater perpendicular heating in simulation A is due to non-adiabatic behavior in the small guide field regime.

Observations of magnetic reconnection typically find that the electron energy

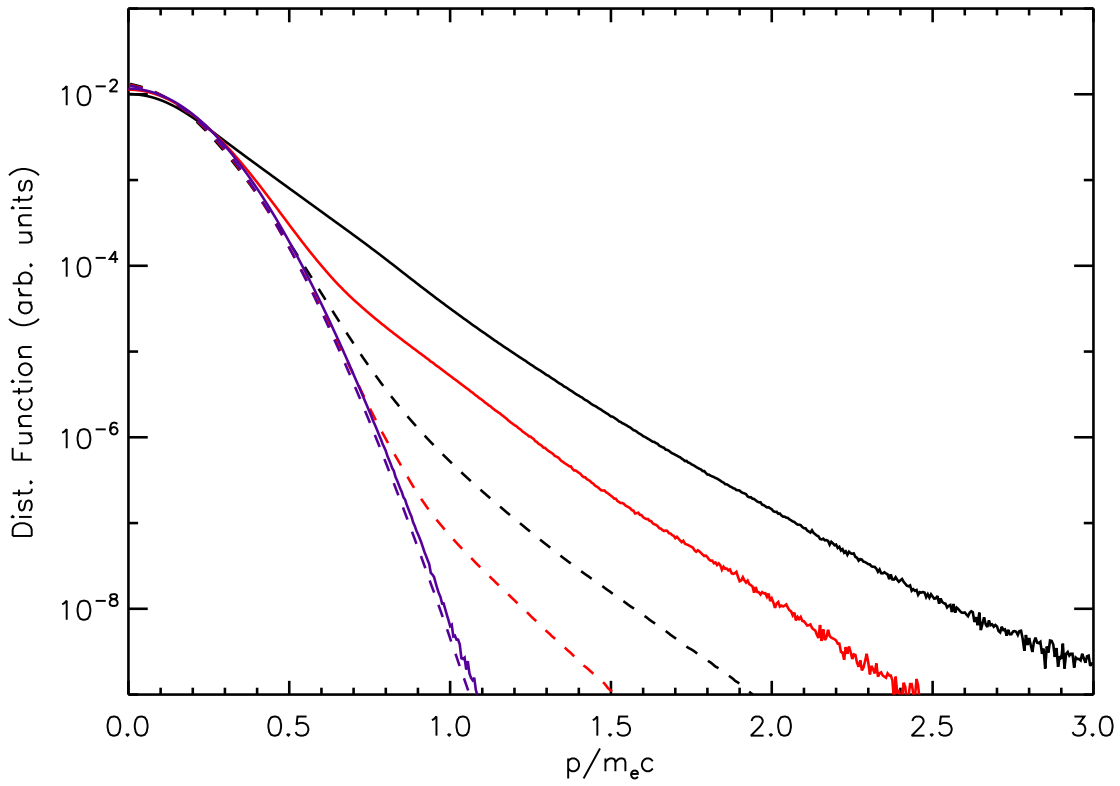

Figure 4.11: Parallel and perpendicular electron momentum spectra (over the entire domain) for a simulation with guide field of $1.0B_0$ in a $L_x \times L_y = 819.2 \times 409.6$ domain. Solid lines correspond to parallel momenta and dashed with perpendicular momenta. Purple, red, and black are at $t = 0$, $50\Omega_{ci}^{-1}$ and $350\Omega_{ci}^{-1}$, respectively. Note the extreme anisotropy of the spectra at late time.

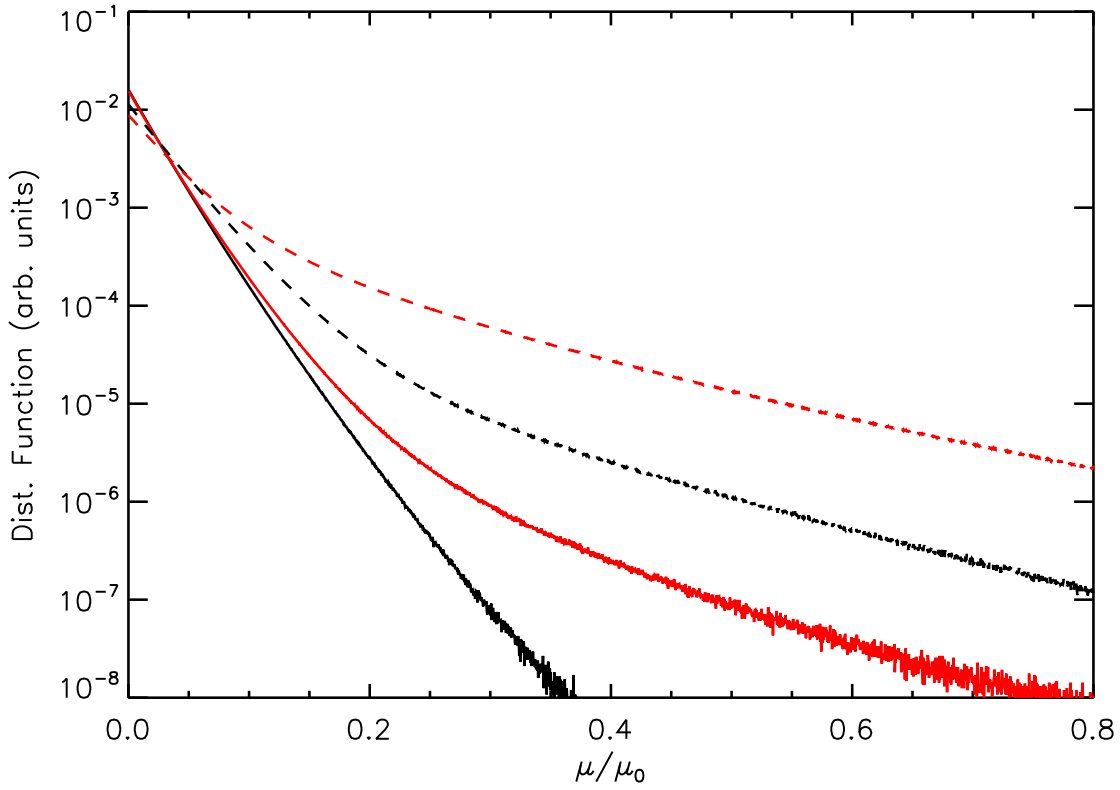

Figure 4.12: Distribution of the electron magnetic moment $\mu = mv_\perp^2/2B$ (over the entire domain) for simulation A (dashed lines) and B (solid lines). Black corresponds with $t = 0$, red with $t = 100$.

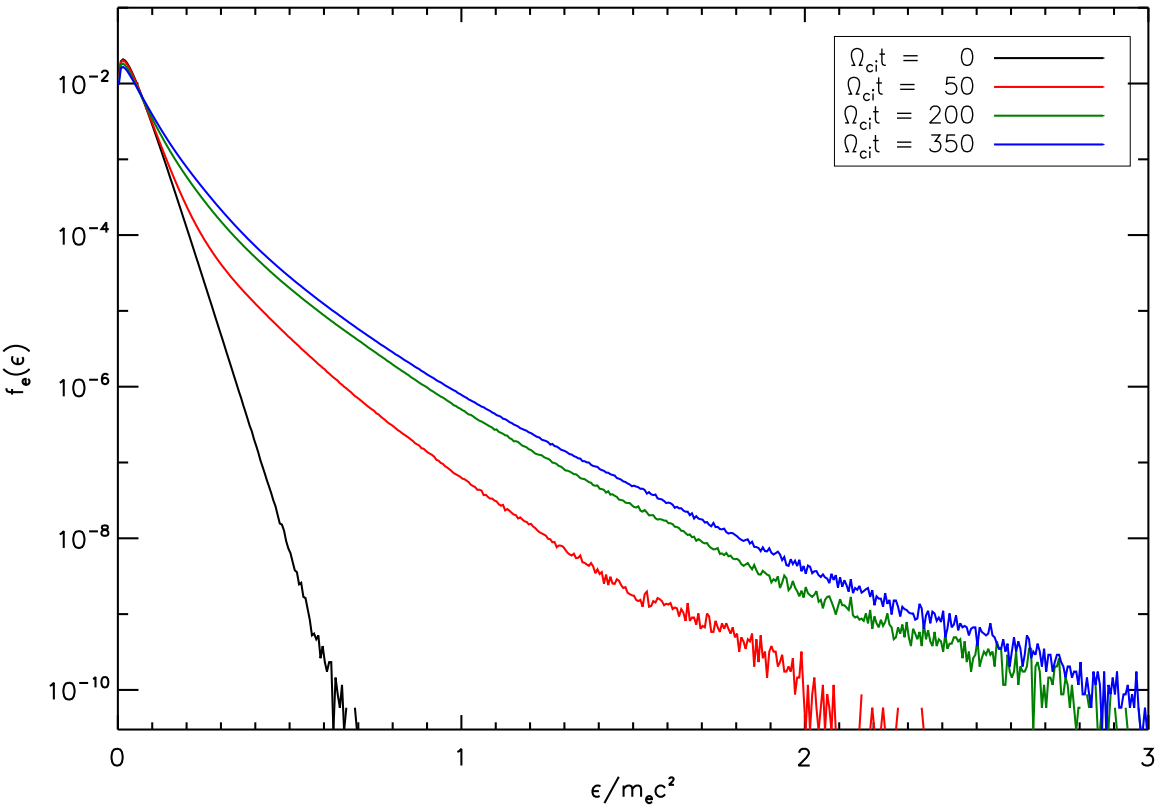

Figure 4.13: Log-linear plot of distribution of electron kinetic energy $\epsilon = (\gamma - 1)m_e c^2$ (over the entire domain) for a simulation with $L_x \times L_y = 409.6 \times 204.8$ and $B_{z0} = B_0$.

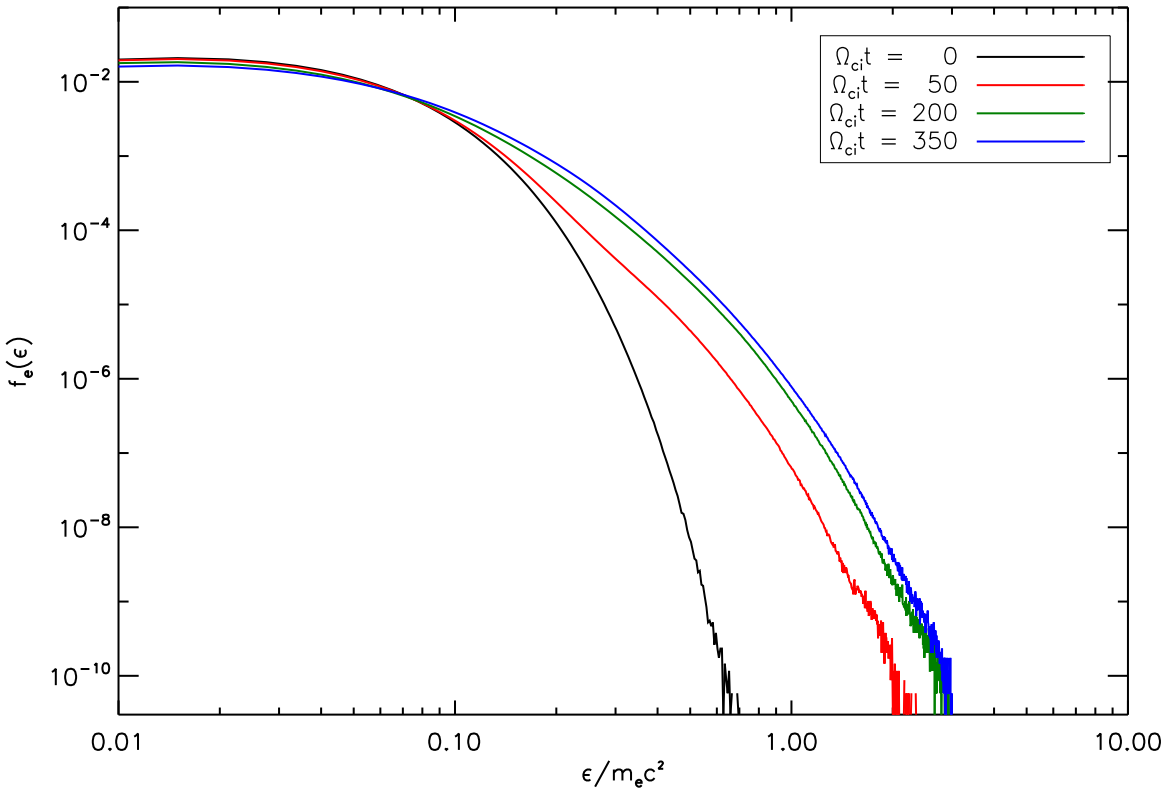

Figure 4.14: Log-log plot of distribution of electron kinetic energy $\epsilon = (\gamma - 1)m_e c^2$ (over the entire domain) for a simulation with $L_x \times L_y = 409.6 \times 204.8$ and $B_{z0} = B_0$. No clear power law develops in the energetic spectra.

spectra take the form of a power law. Electron energy spectra for a simulation with $L_x \times L_y = 409.6d_i \times 204.8d_i$ are shown in Figs. 4.13 (log-linear) and 4.14 (log-log). The late-time spectrum in Fig. 4.14 do not show any clear indications of a power-law component. This is not entirely surprising, as it has been argued that particle loss (absent in periodic simulations) is required for the formation of power-laws [53]. Another possible factor is that the maximum energy gain depends on the time of the simulation (which in turn depends on the domain size as larger systems have more magnetic flux to be reconnected). Hence a larger domain may be required in order for the most energetic electrons to attain an energy significantly separated from that of the thermal population.

4.5 Mass Ratio Scaling: $m_i/m_e = 100$

In order to explore how these results depend on the mass ratio, we performed a 2D simulation with $m_i/m_e = 100$, $L_x \times L_y = 102.4d_i \times 51.2d_i$ and a strong initial guide field $B_{z0} = B_0$. The speed of light in this simulation is $c = 30c_A$ so that $c/c_{Ae} = 3$ as in the simulations with a mass ratio of 25 (c_{Ae} is the electron Alfvén speed based on B_0). The energy spectra are shown in figure 4.15. There is little enhancement at the highest energies $\epsilon > m_e c^2$ over the last $25\Omega_{ci}^{-1}$.

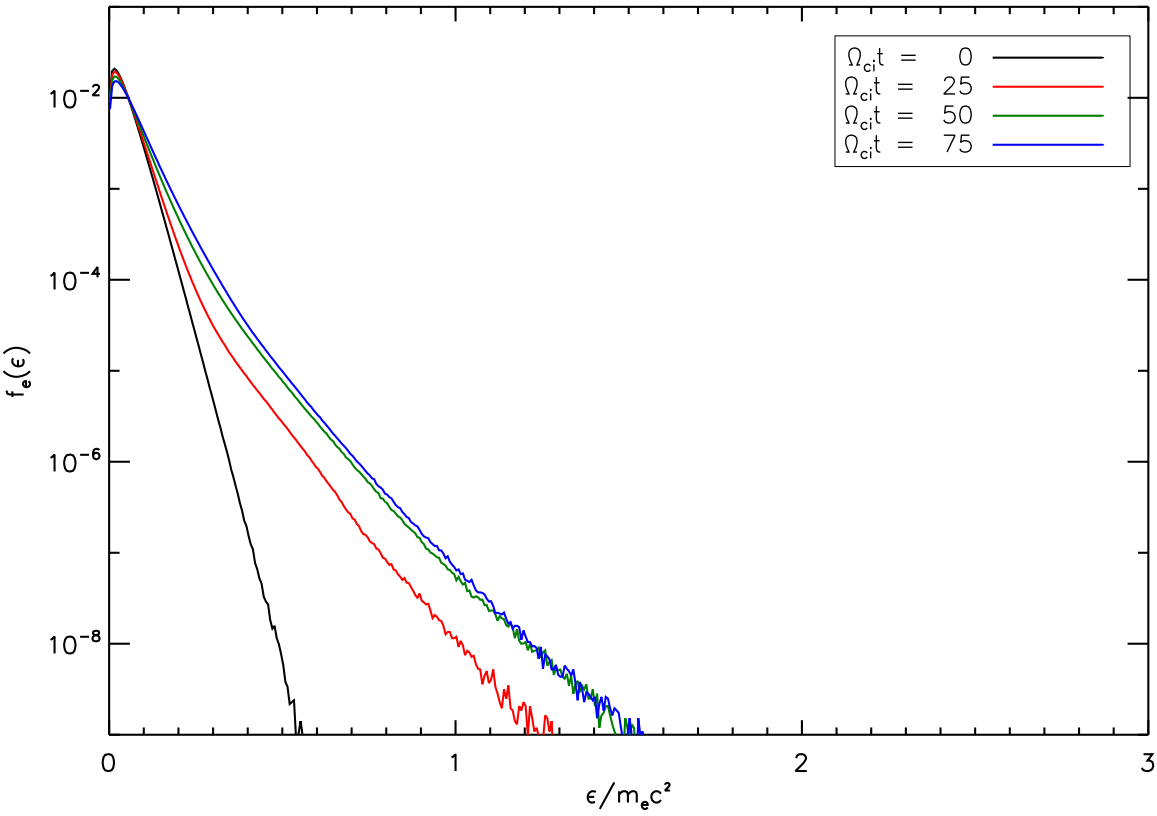

Figure 4.15: Distribution of electron kinetic energy $\epsilon = (\gamma - 1)m_e c^2$ (over the entire domain) for a simulation with mass ratio $m_i/m_e = 100$ and guide field $B_{z0} = B_0$.

Electron momentum spectra (figure 4.16) exhibit a strong anisotropy, as was the case in the strong guide field simulation with the smaller mass ratio. The only significant enhancement in the perpendicular momentum occurs at the highest energies; this is consistent with the idea that this is due to pitch-angle scattering of particles with high parallel momentum. The distribution of μ (figure 4.17) shows that the conservation of the magnetic moment is much better in this simulation. This is unsurprising, as electrons have smaller gyroradii and should therefore be more strongly magnetized. On the other hand, this result also suggests that there are no anisotropy-driven instabilities that are actively scattering the electrons since such instabilities should not be sensitive to the mass-ratio. The time evolution (Fig. 4.19) and spatial distribution (4.18) of the electron heating are not appreciably different than in the simulations with $m_i/m_e = 25$.

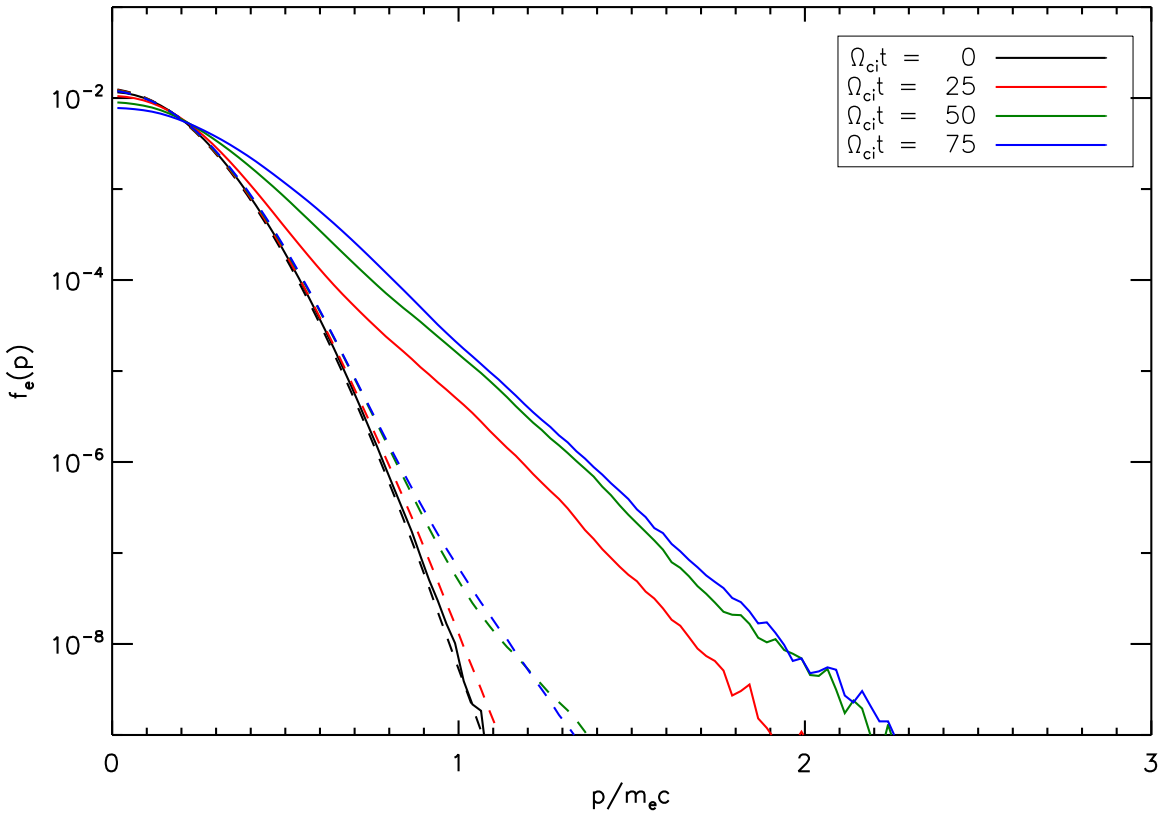

Figure 4.16: Parallel and perpendicular electron momentum spectra (over the entire domain) for a simulation with a mass ratio $m_i/m_e = 100$. Solid lines correspond to parallel momenta and dashed with perpendicular momenta.

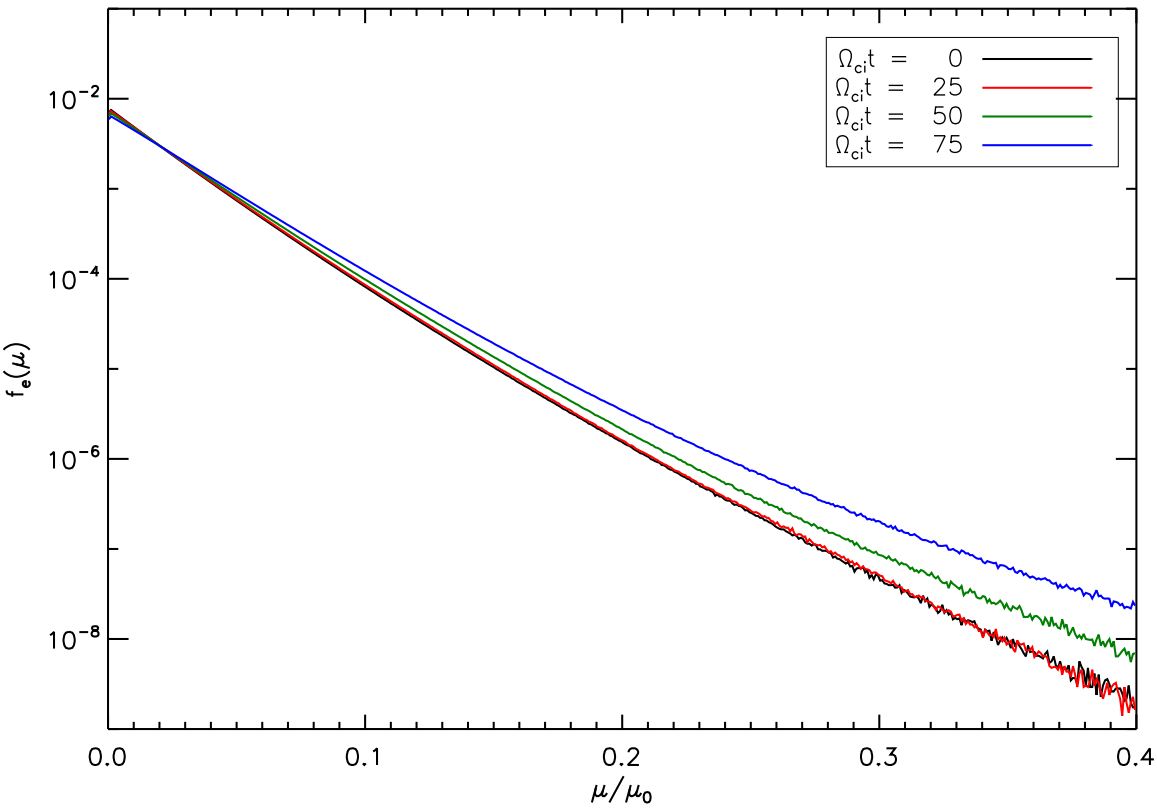

Figure 4.17: Distribution of the electron magnetic moment $\mu = mv_\perp^2/2B$ (over the entire domain) for a simulation with mass ratio $m_i/m_e = 100$.

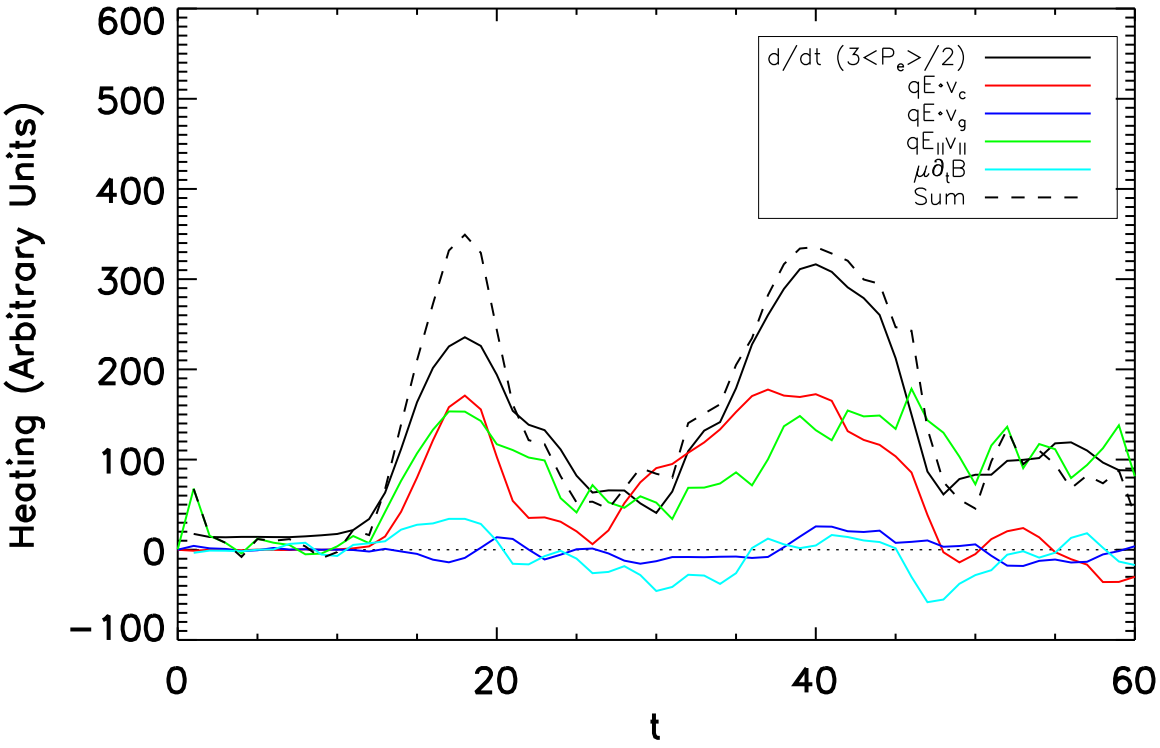

Figure 4.18: From a simulation with mass ratio $m_i/m_e = 100$ and a guide field of $1.0B_0$. The electron heating (black) integrated over the upper current layer versus time is shown. Other heating terms as in Fig. 4.4.

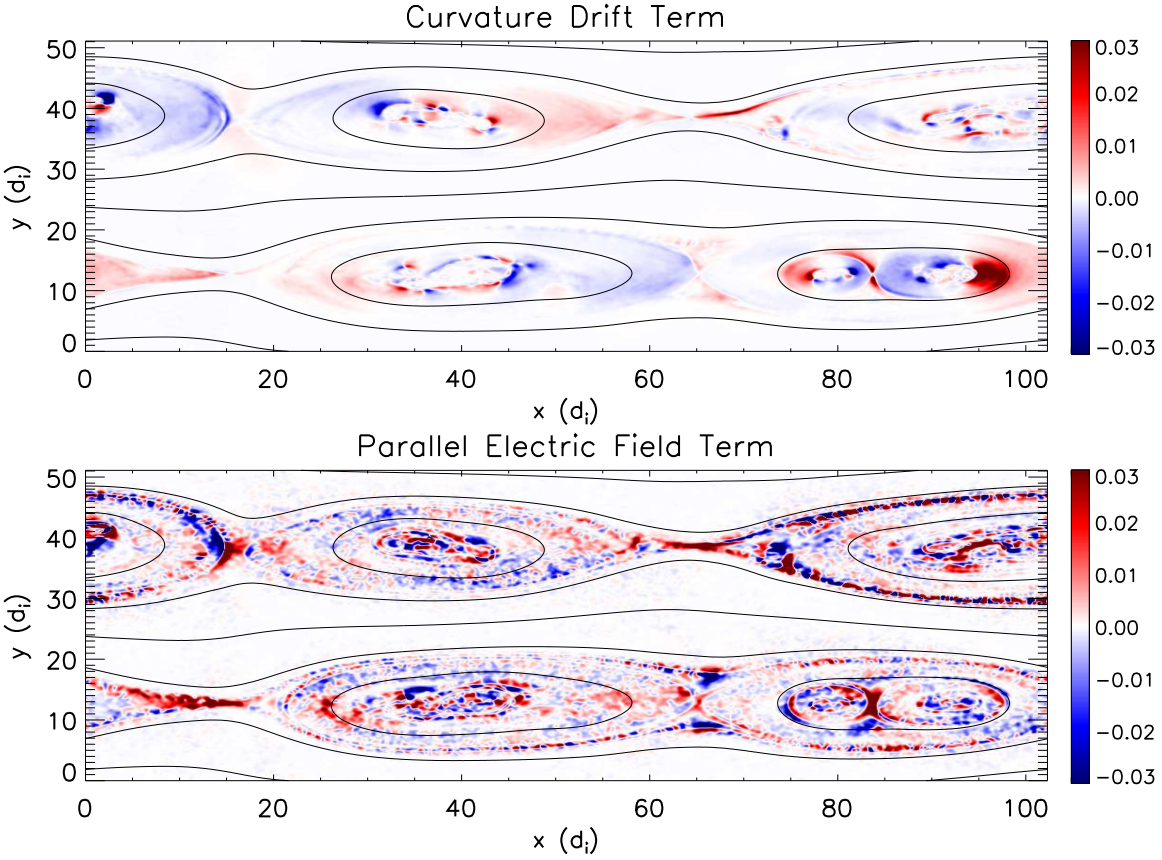

Figure 4.19: The distribution of electron heating for $m_i/m_e = 100$ and a guide field of $1.0B_0$ at $t = 60\Omega_{ci}^{-1}$ from the curvature (top) and the parallel electric field (bottom).

4.6 Discussion and Conclusions

We have presented a guiding center model to explore the heating of electrons during reconnection with modest and large guide fields. We find that for a small guide field of $0.2B_0$ (with B_0 the asymptotic reconnecting field) electron heating is dominated by the Fermi reflection of electrons downstream of X-lines where the tension of newly reconnected field lines drives the reconnection outflow. The electron energy gain is given by the curvature drift of electrons in the direction of the reconnection electric field. In this small guide field case heating from the parallel electric field and that associated with betatron acceleration (which is actually an energy sink) are negligible. In the case of a stronger guide field ($1.0B_0$) the heating associated with parallel electric fields and the Fermi mechanism are comparable. The greater importance of the parallel electric field is because of the elongated current layers that form during reconnection with a guide field, which is where most parallel heating by this mechanism takes place. The net electron heating from electron holes, which densely populate the separatrices and island cores, is small because positive and negative contributions cancel. For both weak and strong guide fields, island mergers lead to bursts of electron acceleration.

An important scaling question concerns the role of heating by the parallel electric field in very large systems. The acceleration by parallel electric fields is largely confined to the narrow current layers around the X-line. In contrast, the heating through Fermi reflection occurs in a broad region in the exhaust downstream of X-lines and well into the ends of magnetic islands. At early times the sheer number

of X-lines could well make parallel electric fields a significant source of heating and acceleration. However, at late time when islands may be system-size, fewer x-lines might remain so parallel electric fields might not produce significant acceleration. In addition, the regions in which the $E_\parallel J_\parallel$ term dominates have characteristic widths that scale with $d_e \propto m_e^{1/2}$ with m_e the electron mass. In the simulations presented here, $m_i/m_e = 25$. For a real mass ratio of $m_i/m_e \approx 1836$ the corresponding regions with $E_\parallel \neq 0$ are expected to be much smaller. In contrast, the curvature drift dominates electron heating on island scales, which are not expected to depend on the choice of mass ratio once islands grow to finite size.

Evidently, further simulations are required to test whether the conjecture that $E_\parallel J_\parallel$ becomes less important in large systems is valid. One of the motivations of exploring electron acceleration in the guiding center model is to develop a generic approach for addressing acceleration mechanisms in 3D systems where simple explanations of particle acceleration in contracting islands are no longer adequate: magnetic islands will generally no longer exist because field lines in 3D systems are chaotic and therefore volume-filling. However, since the conversion energy by the relaxation of magnetic tension is fundamental to the reconnection process, we expect that the Fermi-like acceleration mechanism will remain important in a 3D system and its role can be quantified by evaluating the heating mechanisms presented in Eq. (3.28).

Finally, we comment briefly about the implications of the strong anisotropy of the energetic electrons seen in the spectra in Fig. 4.11 for the simulation with a guide field of $1.0B_0$. Gamma-ray flares have recently been detected in the Crab

Nebula with photon energies exceeding ≈ 200 MeV. These photons exceed the upper cutoff (≈ 160 MeV) that is obtained by balancing energy gain from the electric field $E \sim B$ with that from losses associated with the synchrotron radiation reaction force. One proposed solution is that electrons are accelerated to the necessary energies ($\approx 10^{15}$ eV) in a large-scale reconnecting current sheet where $E \ggg B$ and the usual synchrotron assumptions do not apply [54]. On the other hand, constraining the electrons in a narrow layer and preventing their escape into the reconnection exhaust and downstream magnetic island is a challenge. Another possibility is that reconnection takes place in the presence of a guide field such that the acceleration of the electrons is dominantly parallel to the local magnetic field so that the anistropic energy distribution could mitigate synchrotron losses. In such a situation a rough upper limit on reconnection-driven energuzation can be obtained by balancing the Fermi drive (scaling as γ/R_c, where R_c is a typical radius of curvature of a reconnecting magnetic field) against the curvature radiation loss (γ^4/R_c^2),

$$\gamma < (R_c/R_e)^{1/3} \tag{4.4}$$

where $R_e = e^2/m_e c^2 = 2.82 \times 10^{-13}$ cm is the classical electron radius. For the most energetic events R_c should equal the system size. Based on the flare duration of 1 day, $R_c \approx 3 \times 10^{15}$ cm and the upper limit on the electron energy is $\epsilon = \gamma m_e c^2 \sim 10^{15}$ eV, which is in the range needed to explain the observations. Clearly, a fundamental question is whether there are scattering mechanisms that limit the degree of anisotropy of the energetic particle spectrum and therefore reduce the upper limit given in Eq. (4.4).

Chapter 5: Electron Acceleration in a Three-Dimensional System

In this chapter, we explore magnetic reconnection in 3D systems with a strong guide field, which is the most generic form of reconnection in space and astrophysical plasmas. We find that the efficiency of particle acceleration is greatly increased compared to that in 2D systems. We show that this occurs because the complex 3D magnetic fields enable the most energetic particles to continually access volume-filling acceleration sites rather than being confined to a single magnetic island that no longer accelerates particles once it has fully contracted. We also examine the energy dependence of the dominant $E_{\parallel}$ and Fermi acceleration mechanisms, and find that Fermi reflection is the primary accelerator of the energetic electrons. In section 5.1, we lay out the setup for the simulations discussed in this chapter. We then describe the three-dimensional evolution of the simulations and describe the stochastic structure of the magnetic field in section 5.2. We then examine energetic electron spectra and the localization of acceleration regions in 5.3. We compare and contrast particle trajectories in 2D and 3D systems in 5.4. The transition from 2D to 3D reconnection is examined in 5.5, and the role of anisotropy in the 2D and 3D systems is briefly discussed in 5.6. We then discuss some of the implications and limitations of these results in 5.7.

5.1 Three-Dimensional Setup

We explore particle acceleration via simulations using the massively parallel 3D particle-in-cell (PIC) code `p3d` [42]. Particle trajectories are calculated using the relativistic Newton-Lorentz equations, and the electromagnetic fields are advanced using Maxwell's equations. The simulations are initialized with a force-free magnetic field of the following form: $B_x = B_0 \tanh(y/w_0)$ and $B_z = \sqrt{2B_0^2 - B_x^2}$, where B_0 is the asymptotic value of B_x and and $w_0 = 0.25d_i$. This geometry corresponds to an asymptotic guide field with a magnitude equal to B_0. We include two current sheets at $y = L_y/4$ and $3L_y/4$ to produce a periodic system. The force-free configuration is chosen as the most generic model for large-scale systems such as the solar corona where the density jump between the current layer and the upstream plasma is not expected to be important.

The time and space coordinates are normalized, respectively, to the proton cyclotron time $\Omega_{ci}^{-1} = m_i c/eB$ and inertial length $d_i = c/\omega_{pi}$.

In sections 5.2, 5.3, and 5.4 we examine the results of a 3D simulation with dimensions $L_x \times L_y \times L_z = 51.2d_i \times 25.6d_i \times 25.6d_i$ and an analogous 2D simulation with $L_x \times L_y = 51.2d_i \times 25.6d_i$. The grid cell width is $d_e/4$, where $d_e = d_i\sqrt{m_e/m_i}$ is the electron inertial length. We use an artificial proton-to-electron mass ratio $m_i/m_e = 25$. The 3D simulation used 50 particles per cell for each species, and the 2D simulation used 1600 particles per cell. A 3D simulation with 100 particles per cell produced nearly identical results. The boundary conditions are periodic in all three dimensions and are most relevant for a large current sheet with many

interacting magnetic islands, which is expected in large systems such as the solar corona [55, 56]. The time step is $dt = 0.01\Omega_{ci}^{-1} = 0.25\Omega_{ce}^{-1}$, where $\Omega_{ce} = (m_i/m_e)\Omega_{ci}$ is the electron cyclotron frequency. The initial electron and proton temperatures are $T_e = T_i = 0.25 m_i c_A^2$, and the initial density n_0 and pressure p are constant so that $\beta = 8\pi p/B^2 = 0.5$. The speed of light is $c = 15 c_A$, where $c_A = B_0/\sqrt{4\pi m_i n_0}$.

5.2 3D Magnetic Field Structure

Reconnection develops from particle noise via the tearing instability, generating interacting flux ropes which grow and merge until they reach the system size at $t\Omega_{ci} \sim 50$. The macroscopic evolution of the 2D and 3D systems is similar at this point, though the 2D simulation has released roughly 15% more magnetic energy, as is illustrated in Fig. 5.1.

Fig. 5.2 shows an isosurface of one component of the electron current density J_{ez} at $t\Omega_{ci} = 50$ in the 3D simulation. The current exhibits filamentary structure which develops from instabilities with $k_z \neq 0$ that are prohibited in 2D reconnection simulations [41]. An analogous isosurface of the electron current in the 2D simulation (Figure 5.3) exhibits simple laminar structure.

A different view of that filamentary structure, which emphasizes the chaotic nature of the field lines, can be observed in the Poincaré surface-of-section plot shown in Figure 5.4. There is a clear boundary between the disordered punctures (stochastic field region) and the asymptotic, laminar magnetic field region. Fig. 5.5 shows where an initially uniformly spaced grid of points in the x-y plane at z=0

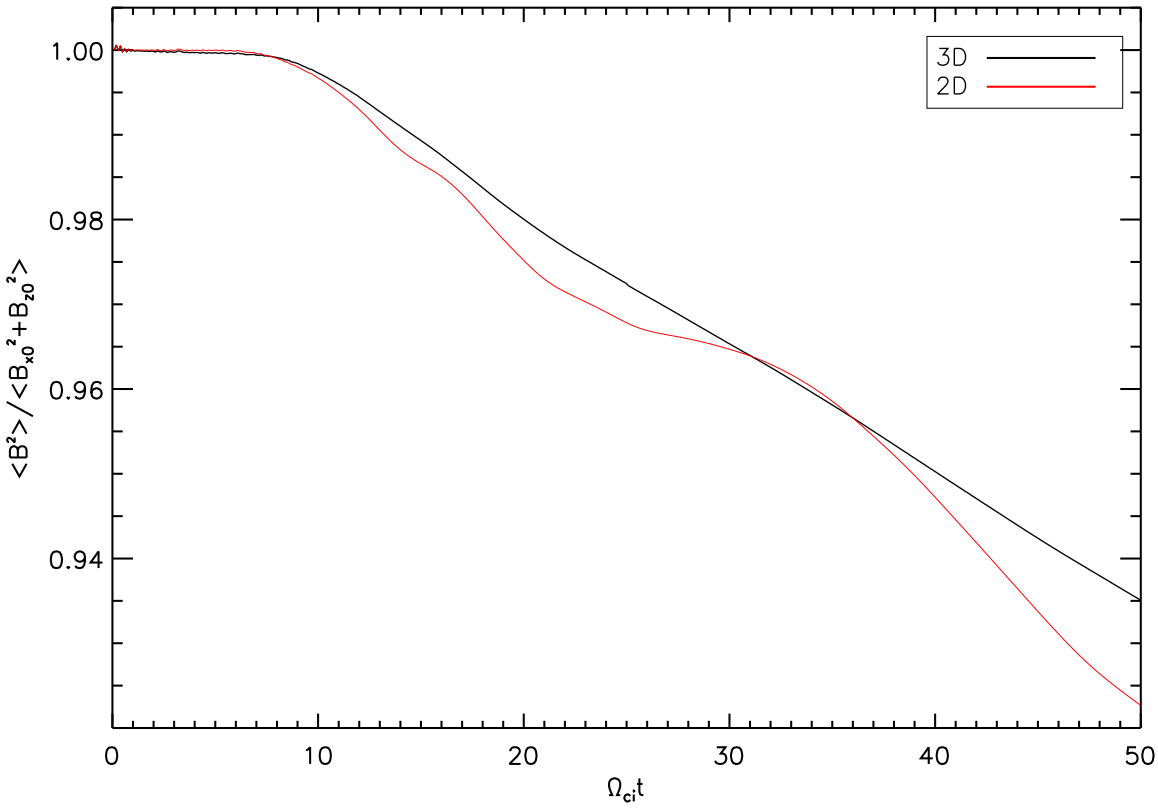

Figure 5.1: Magnetic energy vs. time in 2D and 3D simulations. At $\Omega_{ci}t = 50$, more energy has been released in the 2D simulation.

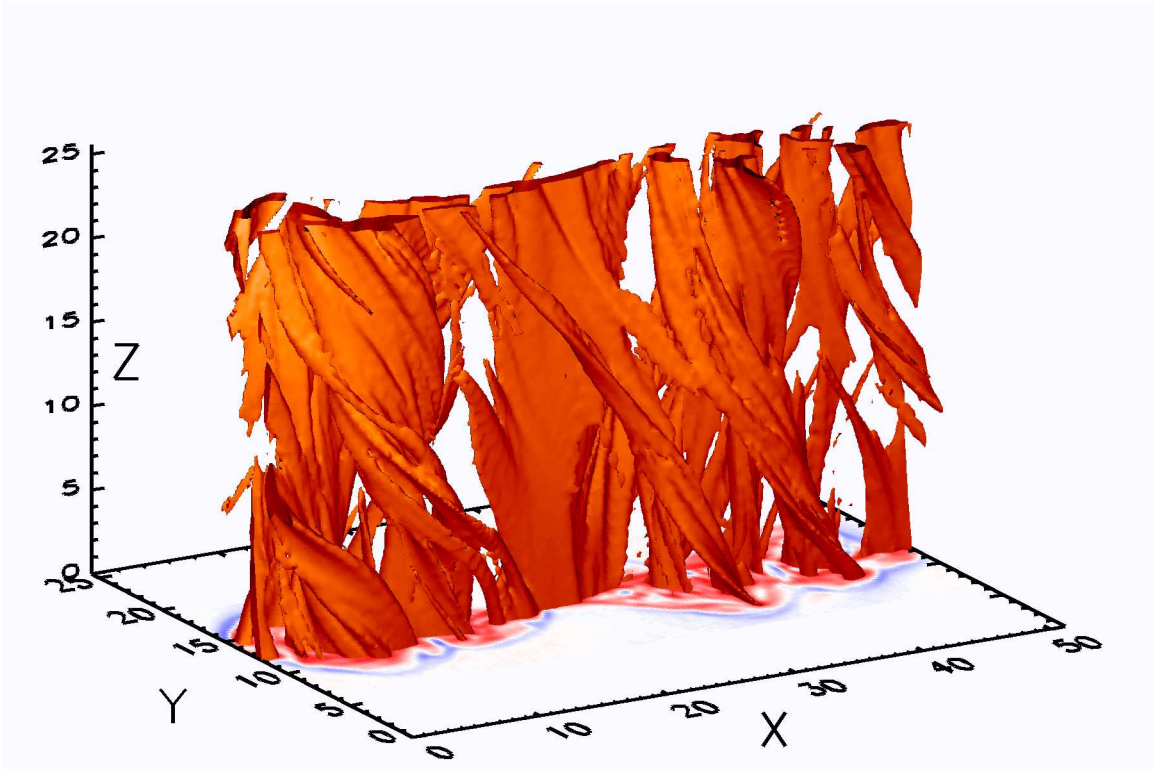

Figure 5.2: Isosurface of J_{ez} in the 3D simulation $t\Omega_{ci} = 50$. The isosurface level is 60% of the maximum current density (a 2D slice of the same quantity is shown on the bottom). The current is filamentary, exhibiting significant 3D structure.

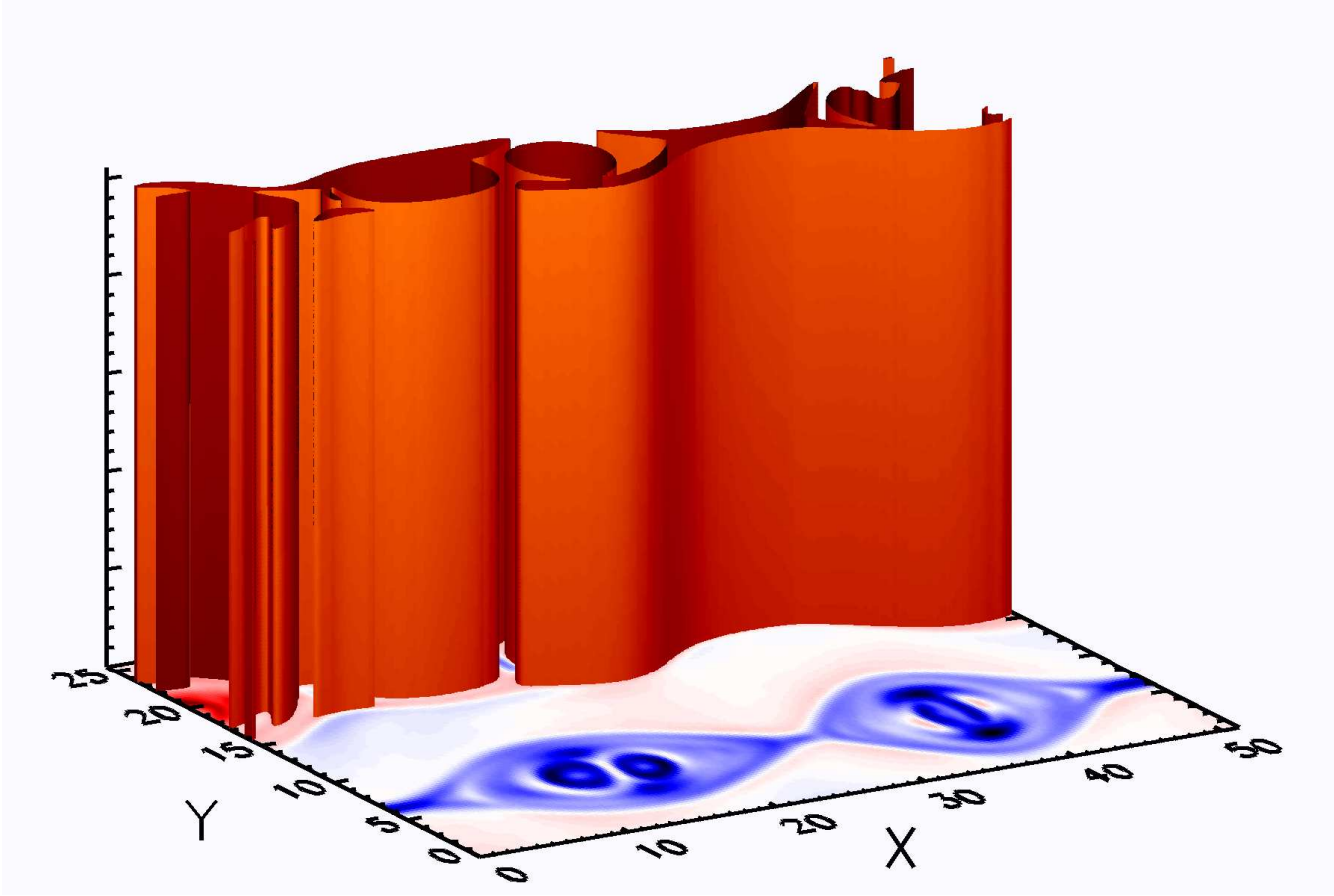

Figure 5.3: Contours of J_{ez} in the 2D simulation $t\Omega_{ci} = 50$. A 3D visualization of the equivalent isosurface with a level 15% of the maximum current density is shown for the upper current sheet. The structure is laminar, consisting of simple 2D flux ropes (islands).

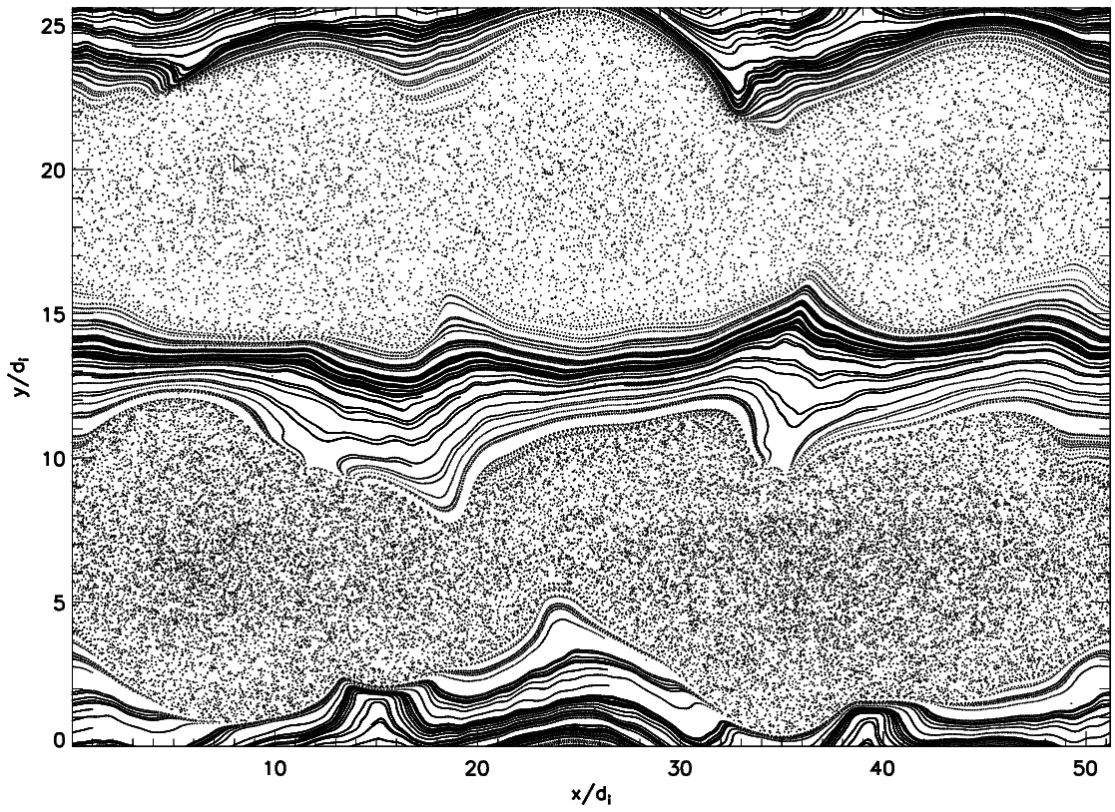

Figure 5.4: Poincaré surface-of-section for the 3D simulation at $\Omega_{ci}t = 50$. We trace a set of field lines beginning at $x = 0$, $0 < y < 25.6$, $z = 0$ and plot where they puncture the plane $z = 0$. The surface-of-section shows a clear boundary between the stochastic field lines inside the reconnecting region and the laminar unreconnected fields.

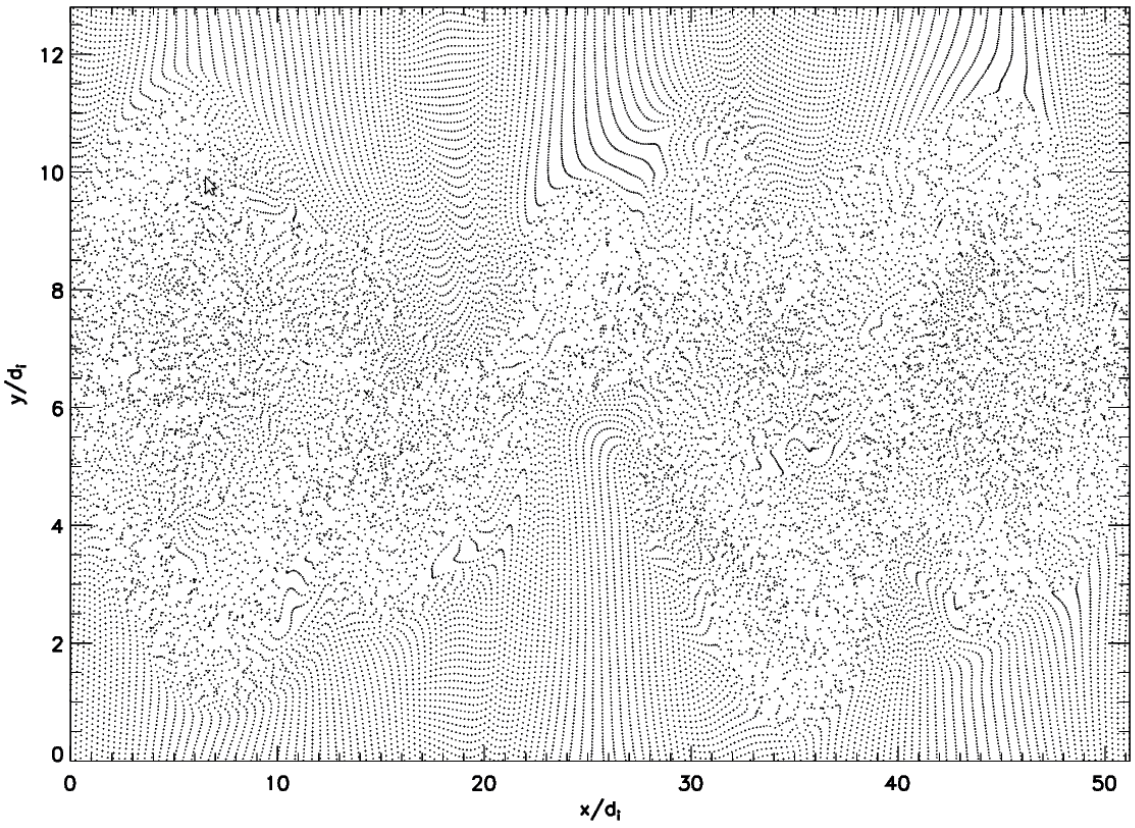

Figure 5.5: Single-puncture field line tracing. We trace an uniform grid of 160 x 320 points in the x-y plane at $z = 0$ along the magnetic lines a single passage through the domain and plot where these field lines puncture the surface at $z = 25.6d_i$. This plot shows finer structure which is reflected in the spatial distribution of the energetic particles (Fig. 5.7).

map along the magnetic field and puncture the plane $z = 25.6d_i$. This highlights additional fine-scale structure not visible in the usual Poincarè plot.

5.3 Electron Energization

Energy spectra (top panel of Fig. 5.6) reveal significant electron acceleration in both simulations. However, the 3D simulation produces a greater number of energetic particles: the fraction of electrons with energy exceeding $0.5m_ec^2$ is roughly an order of magnitude larger than in the 2D simulation. Since the magnetic energy dissipation is greater in the 2D system, this suggests that the increased energetic electron production in the 3D system is due to enhanced acceleration efficiency rather than an increase in the total energy imparted to the plasma.

The spatial distribution of the most energetic particles (shown in the left-hand panels of Fig. 5.7) also differs between these simulations: these particles occupy narrow bands well inside the islands in the 2D simulation, but are distributed throughout the reconnecting region in the 3D simulation. In the 2D system, the reconnected field lines form closed loops (islands) that trap particles. The stochastic structure of the magnetic field in the 3D system, however, allows field-line-following particles to wander throughout the chaotic reconnecting region [37]. The energetic electron energy density (Fig. 5.8) is distributed throughout a much larger region than in the 2D case. This distribution matches very well the distribution of single-pass field lines in Fig. 5.5.

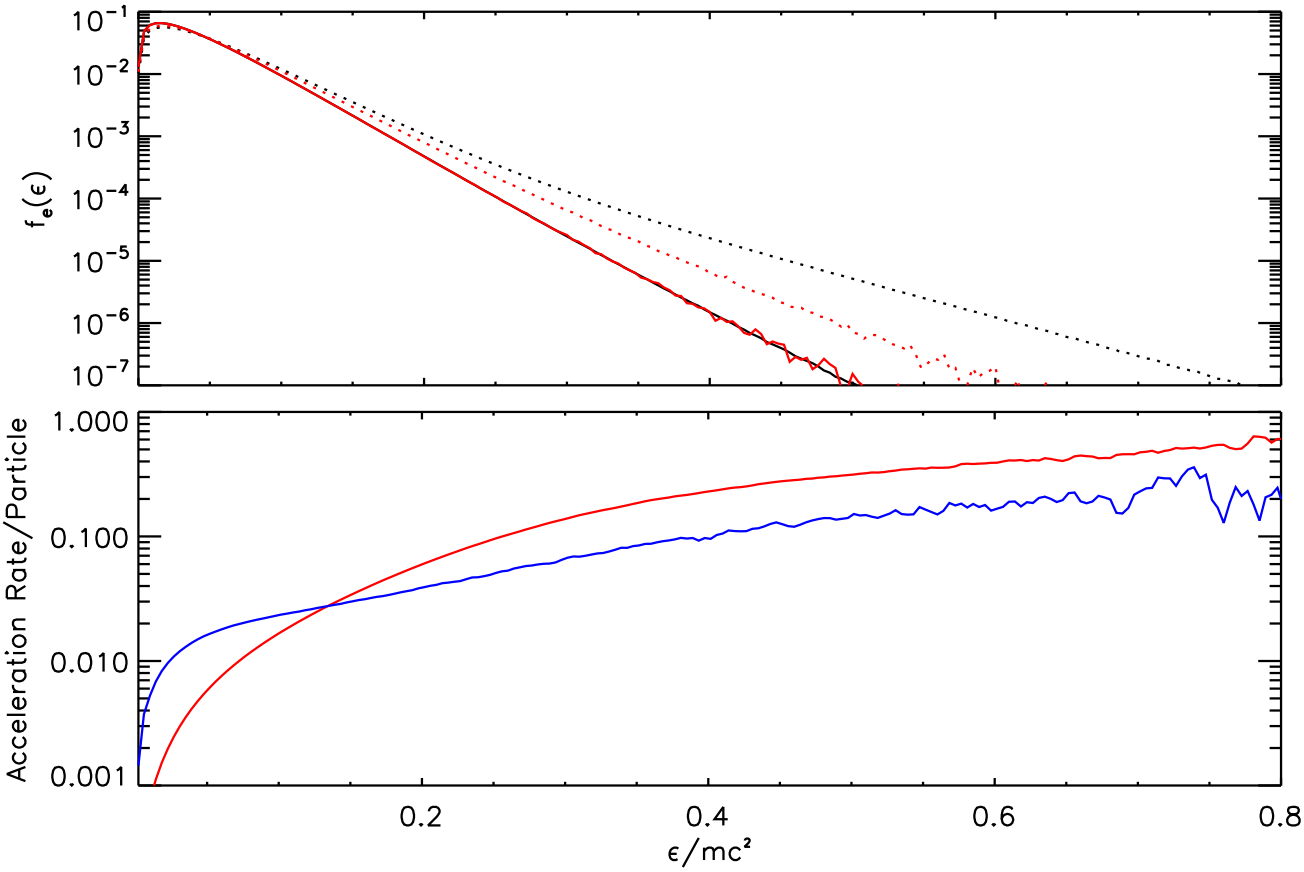

Figure 5.6: [Top] Global electron energy spectra at the beginning (solid lines) and end (dotted lines) of 2D (red) and 3D (black) simulations. The energetic electrons in the 3D simulation gain significantly more energy. [Bottom] Acceleration due to $E_{\|}$ (blue) and Fermi Reflection (red) in the 3D simulation at $t\Omega_{ci} = 50$. Parallel electric fields are most important for low energies, whereas Fermi reflection dominates at high energies.

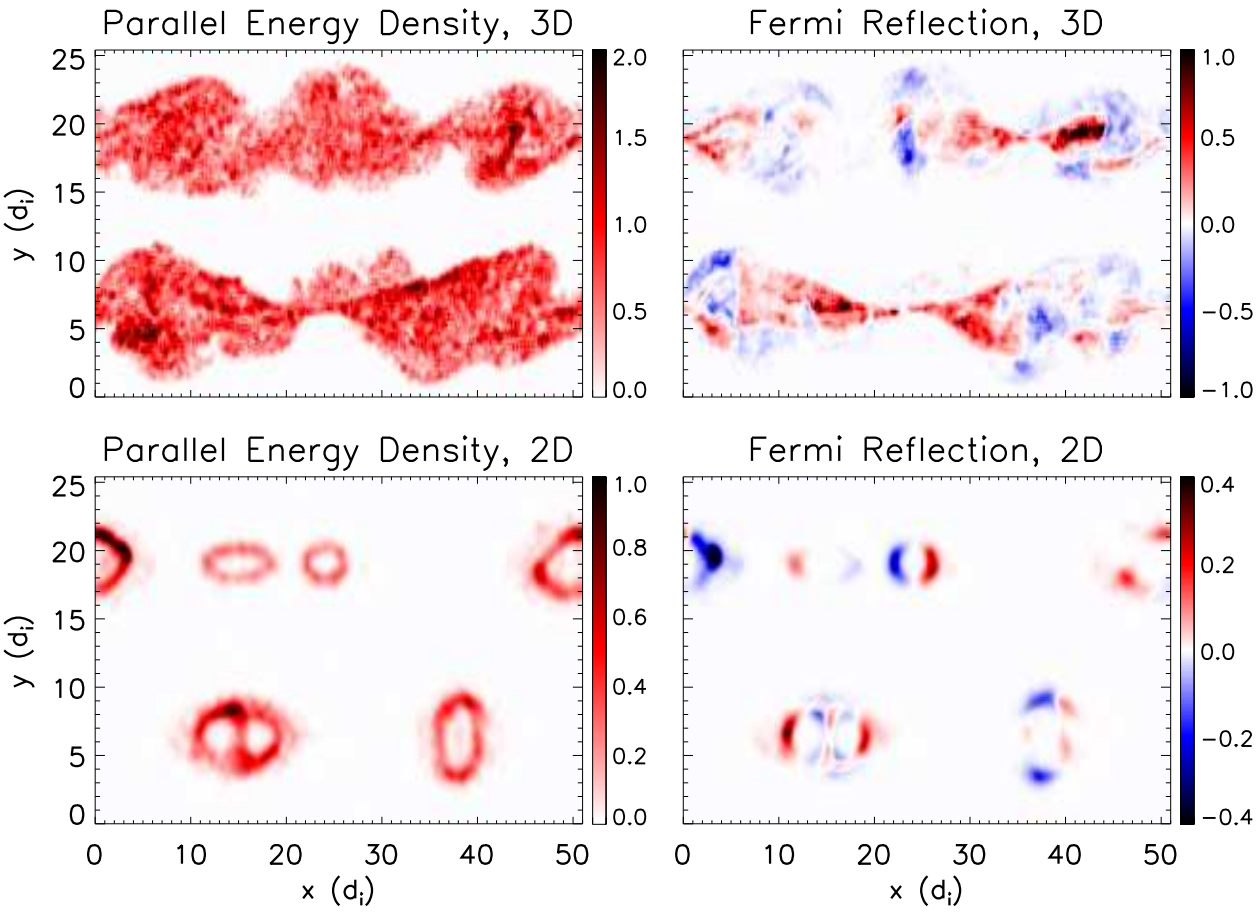

Figure 5.7: Parallel energy density and Fermi reflection heating rate for electrons with $\epsilon > 0.5 m_e c^2$ in the plane $z = 0$ at $\Omega_{ci} t = 50$. The energetic particles are confined to narrow rings in the 2D simulation, but are distributed throughout the reconnecting volume in the 3D simulation. This is reflected in the Fermi reflection heating rate, which is also localized to the rings in the 2D simulation, but distributed throughout the reconnection exhaust in the 3D simulation.

In order to examine the mechanisms responsible for accelerating these particles, we assume a guiding-center approximation relevant for a strong guide field [46] (for more details, see Chapter 2.6.3). In this limit, the evolution of the kinetic energy ϵ of a single electron can be written as:

$$\frac{d\epsilon}{dt} = qE_{\parallel}v_{\parallel} + \frac{\mu}{\gamma}\left(\frac{\partial B}{\partial t} + \mathbf{u}_{_E} \cdot \boldsymbol{\nabla} B\right) + \gamma m_e v_{\parallel}^2(\mathbf{u}_{_E} \cdot \boldsymbol{\kappa}) \tag{5.1}$$

where $E_{\parallel} = \mathbf{E} \cdot \mathbf{b}$ is the parallel electric field, $\mu = m_e\gamma^2 v_{\perp}^2/2B$ is the magnetic moment, $\mathbf{u}_{_E}$ is the $\mathbf{E} \times \mathbf{B}$ velocity corresponding to the advection of the magnetic field, and $\boldsymbol{\kappa} = \mathbf{b} \cdot \nabla \mathbf{b}$ is the magnetic curvature. The velocity components parallel and perpendicular to the magnetic field are $v_{\parallel}$ and $v_{\perp}$, respectively; γ is the relativistic Lorentz factor, and $\mathbf{b}$ is the unit vector in the direction of the local magnetic field.

The first term on the right-hand-side of the equation corresponds to acceleration by parallel electric fields, which are typically localized near the reconnection X-line and along separatrices. The second term corresponds to betatron acceleration and is a consequence of the conservation of the magnetic moment μ: when a particle experiences a change in B, its perpendicular energy evolves to compensate. In the case of reconnection, which reduces the overall magnetic field, betatron acceleration typically reduces particle energy [57]. The last term corresponds to reflection of particles from contracting magnetic field lines, a type of first order Fermi acceleration [25, 51, 58]. This occurs where tension is released as magnetic fields advect in the direction of magnetic curvature ($\mathbf{u}_{_E} \cdot \boldsymbol{\kappa} > 0$).

Equation 5.1 reveals that the acceleration mechanisms have different scaling with the particle energy: the Fermi reflection term is second order in the parallel

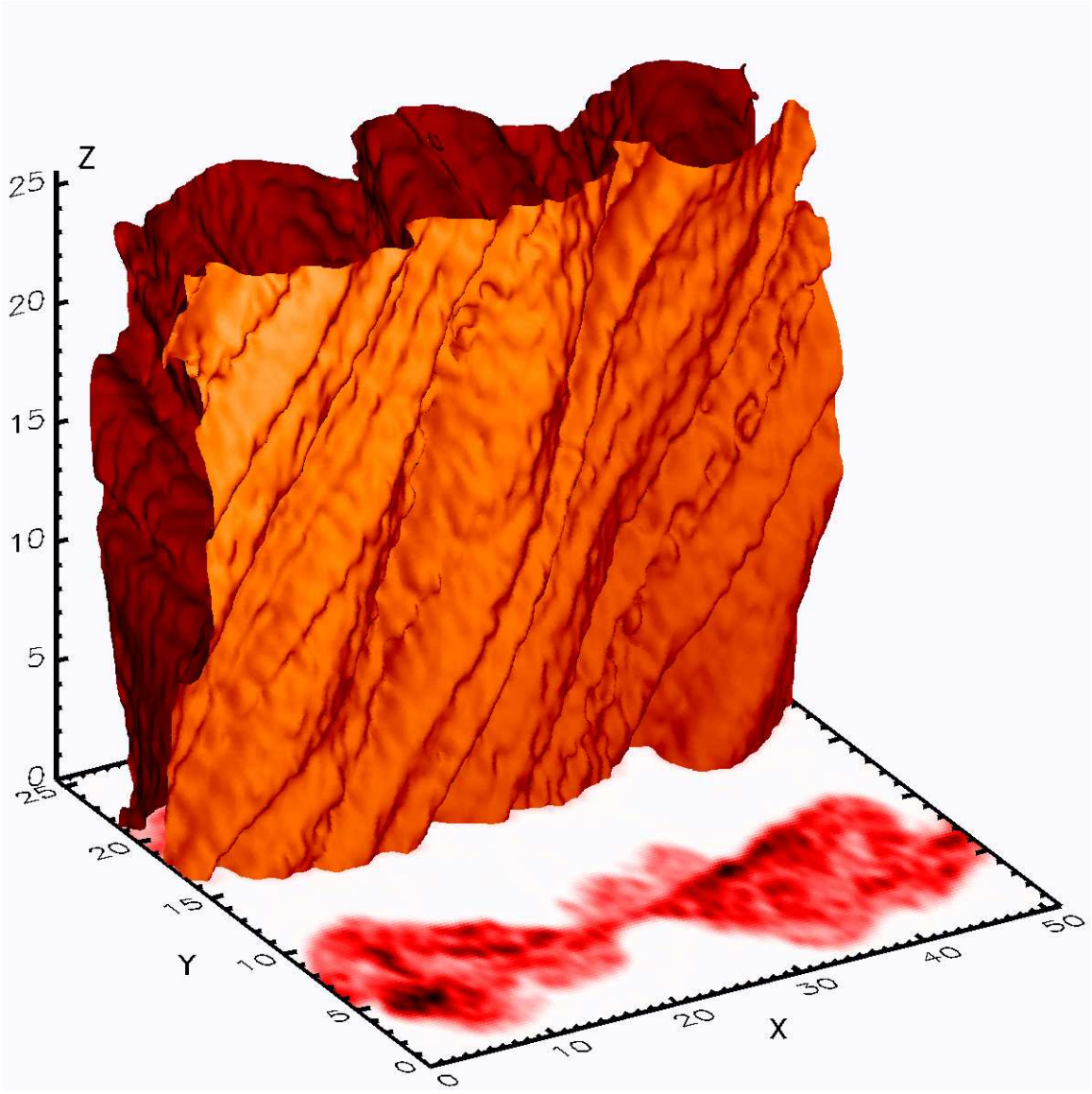

Figure 5.8: Isosurface of the parallel energy density of electrons with $\epsilon > 0.5 m_e c^2$. The isosurface level is set to 10% of the maximum value. The bottom of the figure shows the distribution of the parallel energy density of these particles in the lower current sheet in the plane $z = 0$.

velocity, whereas the parallel electric field term is only first order. The bottom panel of Fig. 5.6 shows the average acceleration per particle for both $E_\parallel$ and Fermi reflection in the 3D simulation at $t\Omega_{ci} = 50$. The bulk thermal electrons (low energies) are primarily accelerated by $E_\parallel$, whereas Fermi reflection is more important at high energies. This indicates that Fermi reflection is the dominant accelerator of the most energetic particles, consistent with the energy scaling of Eq. 5.1.

The spatial distribution of the Fermi reflection term for the most energetic electrons ($> 0.5 m_e c^2$) is shown on the right-hand side of Fig. 5.7. While acceleration occurs throughout the reconnection exhaust in the 3D simulation, in 2D the acceleration is limited to narrow bands near the cores of magnetic islands. This contrast suggests that the stochastic 3D field structure allows the electrons to have greater access to the acceleration regions where magnetic energy is being released. Similar behavior is visible in the parallel electric field term (again, for the most energetic electrons).

5.4 Particle Trajectories

To explore the reason for enhanced acceleration in the 3D system, we examine the trajectories of the 750 most energetic electrons in both the 2D and 3D simulations. A typical trajectory from the 2D simulation is shown in the top left panel in Fig. 5.9. The electron begins in the tail of the electron distribution with kinetic energy $\epsilon \approx 0.4 m_e c^2$. The electron streams along a field line outside the reconnection region before accelerating at an X-line near $x \sim 50$ and becoming trapped in

an island. The electron bounces several times inside this island, accelerating up to $\epsilon \approx 0.8 m_e c^2$. By this point, the field line the electron is following has released its tension, so acceleration ceases even as the electron continues to bounce.

The top right panel of Fig. 5.9 shows a typical electron trajectory from the 3D simulation. The electron is not confined to a single island, but instead moves throughout the reconnecting domain. This allows it to undergo significantly greater acceleration than the electron from the 2D simulation, as it is able to return to active acceleration regions rather than being confined to the stagnant field lines near island cores. The acceleration of this particle is spread across a number of different islands, enabling it to reach a maximum energy of $\epsilon \approx 1.15 m_e c^2$.

The electron trajectories shown here are generic for their respective simulations. Though the acceleration details differ, all of the electrons in the 2D simulation are confined to single islands, whereas no electrons in the 3D simulation show significant trapping. The bottom panels of Fig. 5.9 show the distribution of $|\Delta x| = |x(\Omega_{ci} t = 50) - x(\Omega_{ci} t = 25)|$ for the 750 most energetic particles in each simulation (the choice of $\Omega_{ci} t = 25$ as the earliest time eliminates free streaming along unreconnected field lines before islands develop). The average displacement of the energetic electrons in the 3D system is nearly an order of magnitude greater than that in the 2D simulation, underscoring a fundamental difference in the particle trajectories of the two systems.

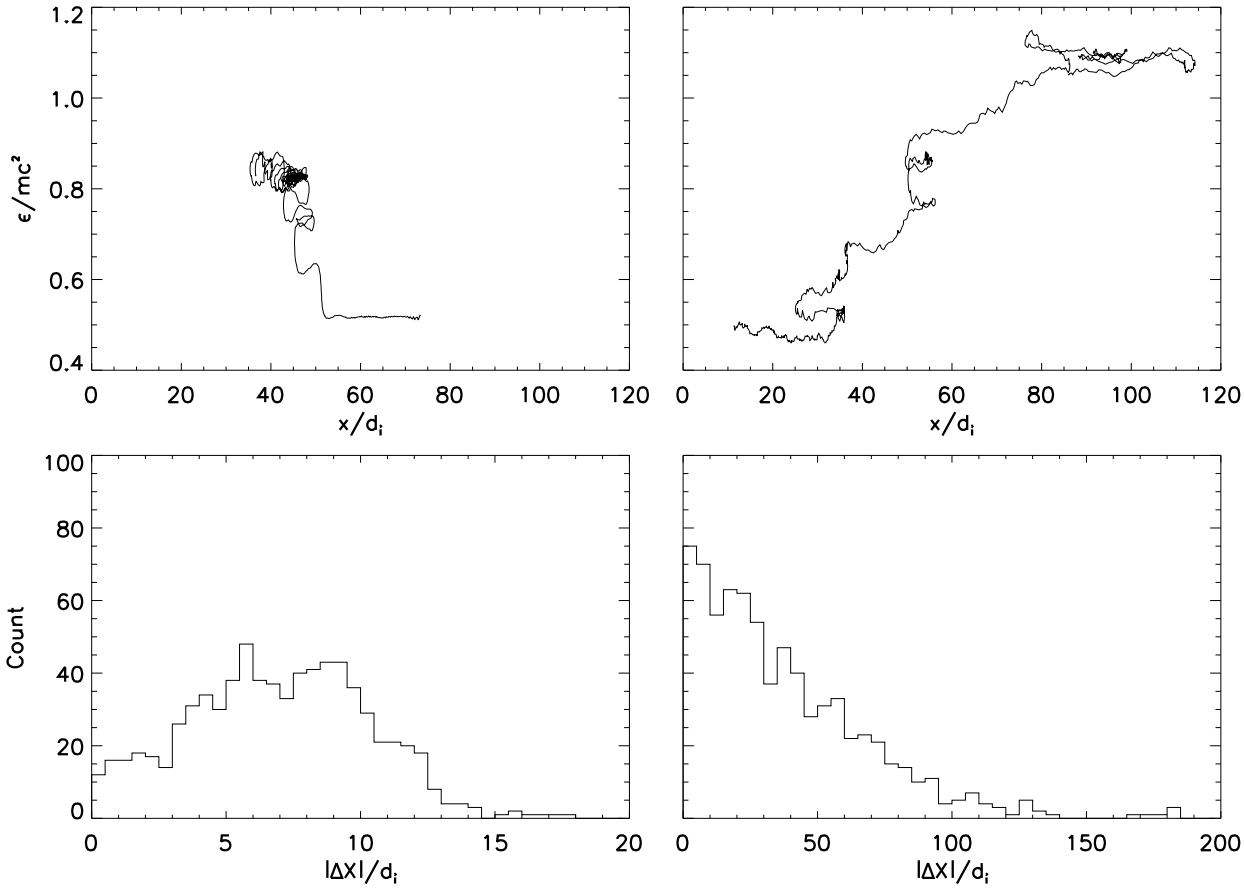

Figure 5.9: [Top] Typical energy vs. position plots for an energetic particle in the 2D system (left) and the 3D system (right) over the period $\Omega_{ci}t = 0$ to 50. The electron in the 3D simulation continuously gains energy as it moves throughout the domain. The electron in the 2D simulation is trapped in an island at $x \sim 40$ for a significant period of time and no longer gains energy after the island has released its tension. [Bottom] Distribution of $\Delta X = |x(t = 50) - x(t = 25)|$ for the 750 most energetic particles in the 2D simulation (left) and 3D simulation (right). The particles in the 3D simulation are able to access a much larger fraction of the simulation domain.

5.5 Transition from 2D to 3D

In order to examine the transition between 2D and 3D reconnection, we performed 3D simulations with different L_z. Fig. 5.10 shows the distribution of electrons with $\epsilon < 0.2 m_e c^2$. The simulations with small L_z have island structures which are mostly laminar. In contrast, the 'islands' in the largest simulations (especially $L_z = 12.8, 25.6$) do not have the simple oval shape as in the 2D simulations. Figure 5.11 shows the spatial distribution of the electrons with $\epsilon > 0.5 m_e c^2$. The simulations with small L_z have rings of energetic particles, as in the purely 2D case discussed earlier. The energetic particles are distributed throughout the reconnecting region in the simulations with $L_z > 6.4 d_i$. The $L_z = 6.4 d_i$ simulation has elements of both the '2D' and '3D' features; while the electrons are well-distributed throughout a few of the islands, others show more of the localized ring distribution.

The electron energy spectra, shown in Fig. 5.12, show a transition between the simulations $L_z = 4.8 d_i$ and $L_z = 6.4 d_i$. The 3D simulations with $L_z \leq 4.8 d_i$ along with the 2D simulation all have spectra which extend to rougly the same energy range. The 3D simulations with $L_z \geq 6.4 d_i$ have spectra which are comparatively enhanced. A transition at $L_z \sim 5 d_i$ is consistent with the energetic electron spatial distribution; though the $L_z = 6.4 d_i$ shows remnants of 2D structure, it appears to be sufficiently three-dimensional for the electron acceleration to be enhanced.

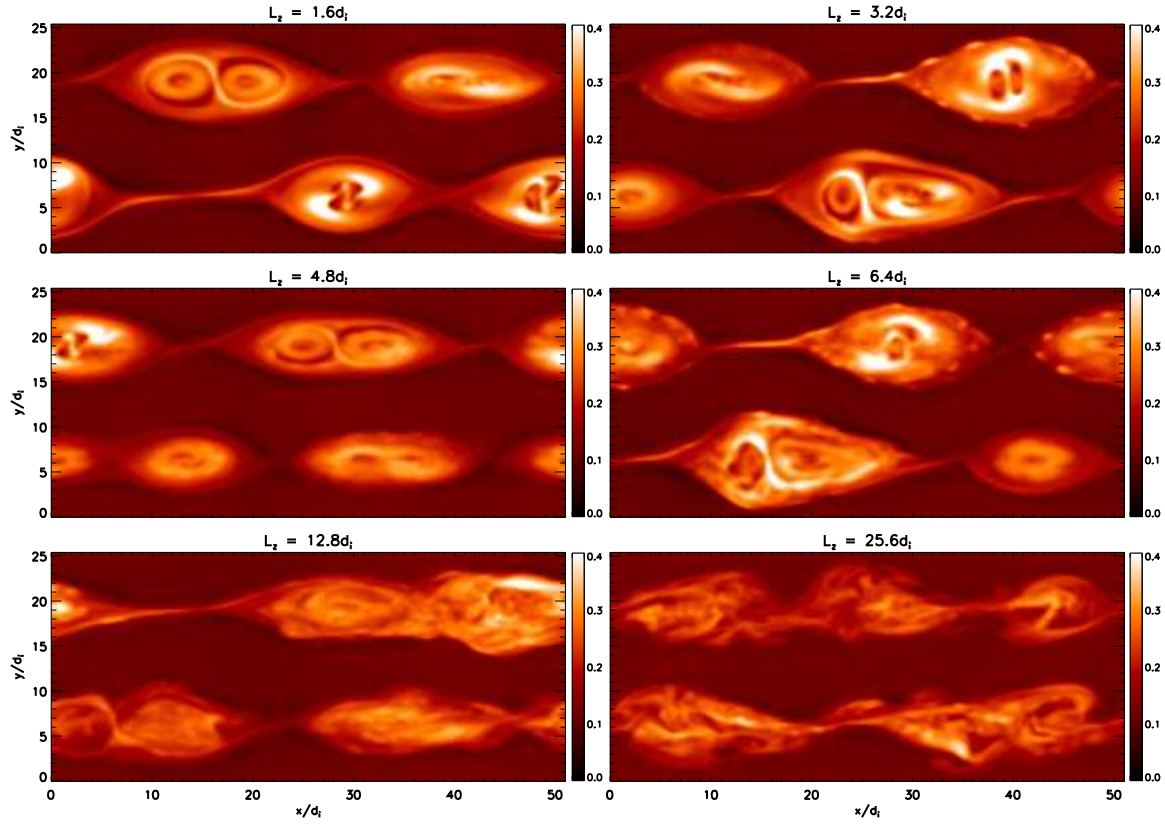

Figure 5.10: Spatial distribution of electrons $\epsilon < 0.2 m_e c^2$ at $\Omega_{ci} t = 50$ in the plane $z = 0$ for 3D simulations with differing L_z. The islands in the smallest simulations are largely laminar, while the islands in the largest simulations exhibit complex, turbulent structure.

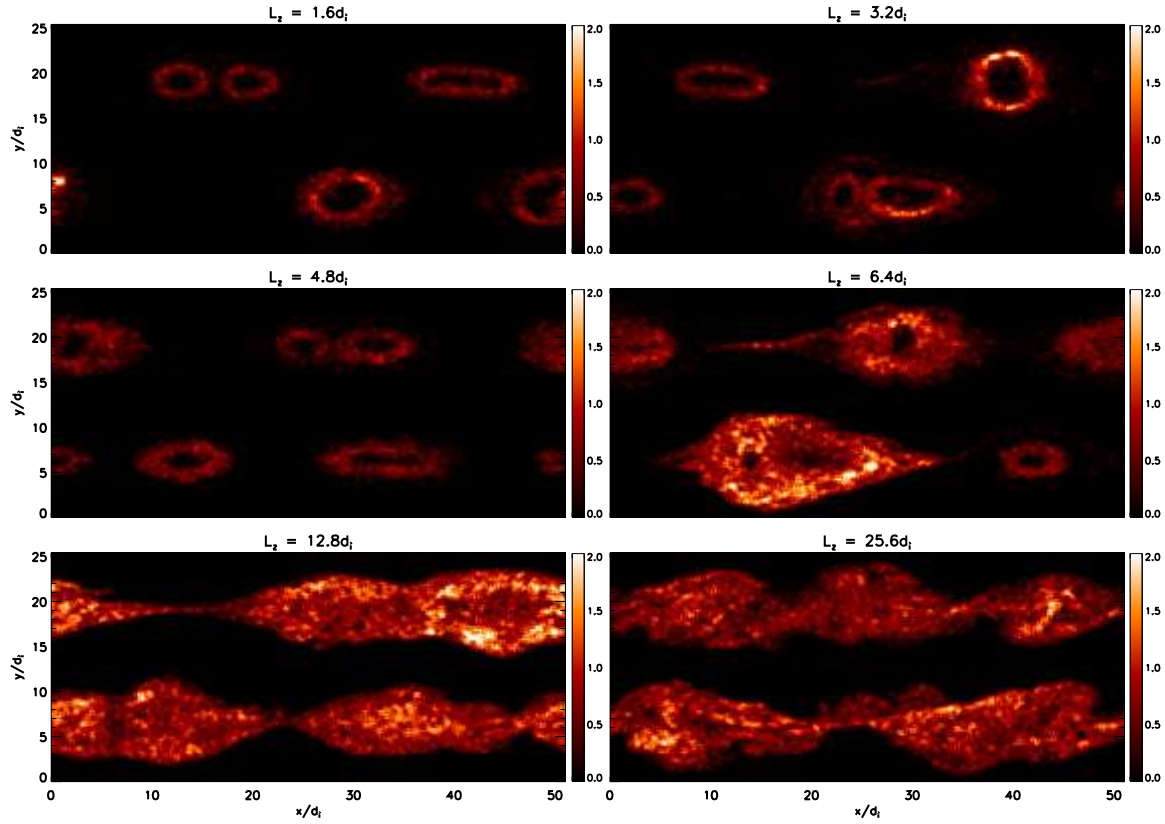

Figure 5.11: Spatial distribution of electrons $\epsilon > 0.5 m_e c^2$ at $\Omega_{ci} t = 50$ in the plane $z = 0$ for the simulations shown in Fig. 5.10. Simulations $L_z \leq 4.8 d_i$ exhibit localized rings of energetic particles as in the purely 2D simulation, whereas those with $L_z \geq 6.4 d_i$ have energetic electrons distributed throughout the reconnecting region.

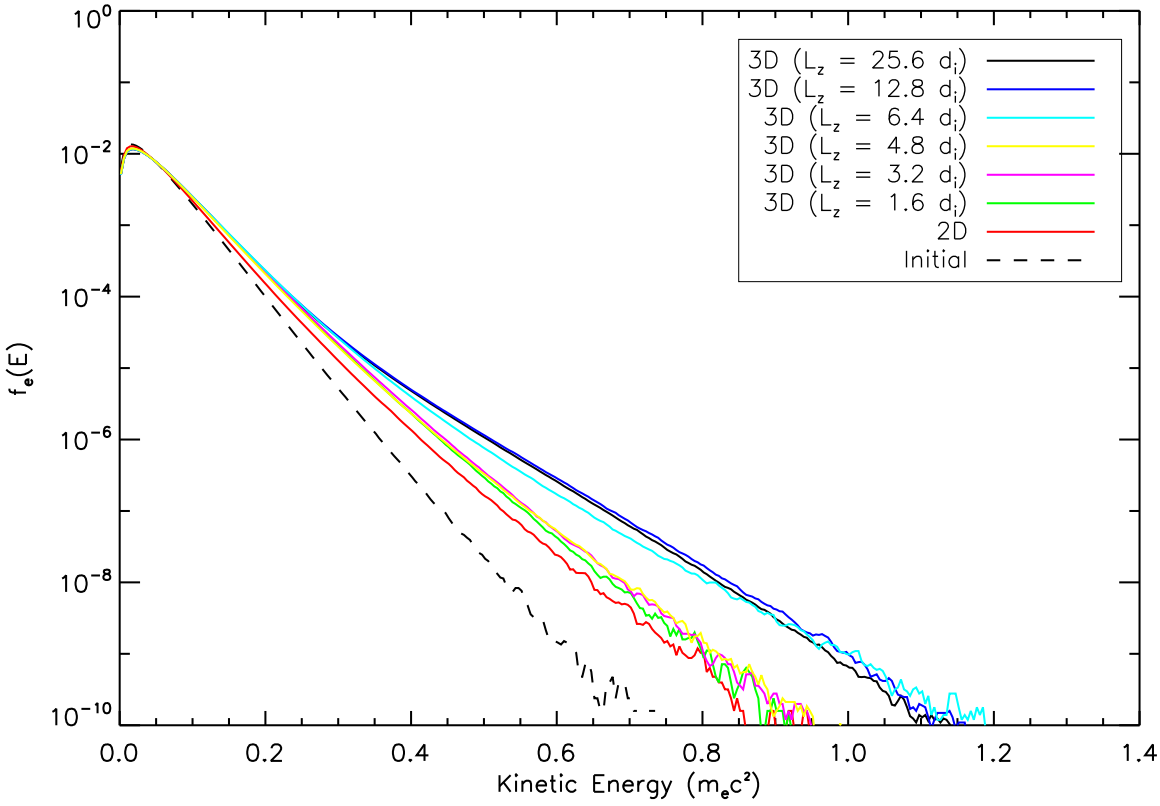

Figure 5.12: Electron energy spectra at $\Omega_{ci}t = 50$ for the simulations shown in Fig. 5.10. The simulations with $L_z \geq 6.4d_i$ show enhanced electron energization compared to the simulations with $L_z \leq 4.8d_i$.

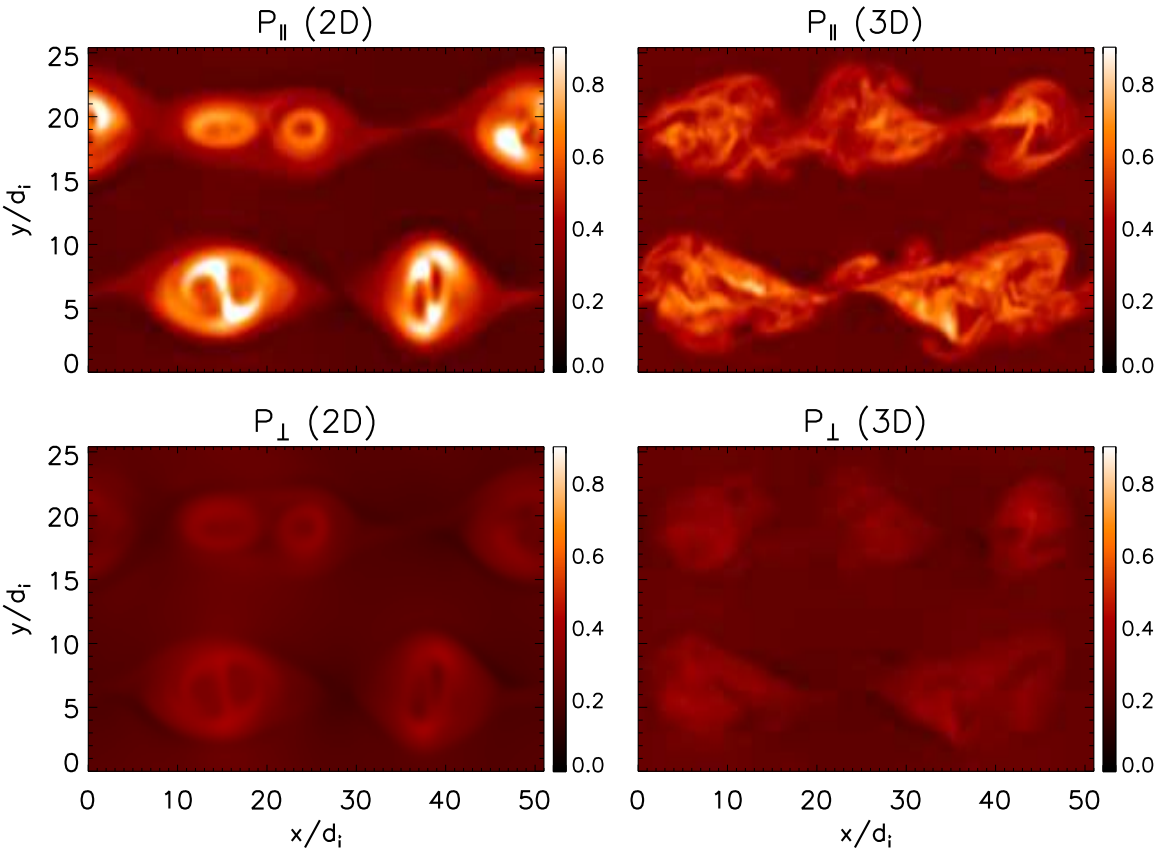

Figure 5.13: Comparison of parallel and perpendicular electron temperature $P_{\parallel}$ and $P_{\perp}$ for the 2D and 3D systems. Both simulations exhibit a strong anisotropy.

5.6 Anisotropy

It has been shown previously that the development of pressure anisotropy with $P_{\parallel} \gg P_{\perp}$ causes the cores of magnetic islands to approach firehose marginal stability, where the tension driving magnetic reconnection ceases, thereby throttling reconnection. Figure 5.13 shows that a significant anisotropy $P_{\parallel} > P_{\perp}$ persists in the 3D system, suggesting that the turbulent dynamics do not significantly isotropize the pressure. It therefore seems likely that energetic particle feedback on reconnection through the firehose mechanism will continue in the more complex magnetic geometry of 3D systems.

5.7 Discussion

The nonthermal electron spectra in both simulations do not assume a power law form as is frequently observed in nature. This is due in part to the limited energy gain possible in the modest-sized 3D simulation presented here. Previous 2D simulations have shown the total energy gain is greater in larger systems [57]. An additional issue is that these simulations have periodic boundary conditions so no particles are lost from the system. Solar observations suggest that electrons are confined in regions of energy release in the corona [17]. The mechanism for confinement remains an open issue. Both magnetic mirroring and double layers are possible mechanisms [59]. On the other hand, it has been suggested that the development of a power law requires a loss mechanism in addition to an energy drive

[53]. However, recent electron-positron simulations [60, 61] suggest that power-law spectra may still develop in the absence of a loss mechanism. The set of conditions under which power-law spectra form in kinetic reconnection simulations remains an open issue.

A limitation of the present simulations is the use of an artificial mass ratio, which reduces the separation between proton and electron scales. In order for an electron to access multiple acceleration sites, as we observe in our simulations, its characteristic velocity must exceed that of the macroscopic flows associated with the protons. This suggests that we have achieved a significant separation of scales (the dependence on the mass ratio will be discussed more fully in Chapter 6). In contrast, proton spectra (not shown) do not exhibit enhanced acceleration in the 3D system. The absence of a separation of scales between the motion of energetic electrons and the flows associated with reconnection exhausts may explain why enhanced electron acceleration is not observed in electron-positron simulations [60].

Chapter 6: Scaling of Electron Acceleration in Three-Dimensional Reconnection

Three-dimensional kinetic simulations of magnetic reconnection are greatly constrained by computational expense. Hence, runs require compromises in the numerical prameters of a simulation. There are two key areas where numerical constraints could pose a potential problem. The first is the use of an artificial mass ratio in order to reduce the separation of scales between protons and electrons and hence reduce computational expense (discussed more extensively in Section 2.6.2). The simulations and analysis presented thus far have focused on the case of a modest mass ratio of $m_i/m_e = 25$, which is much smaller than the physical ratio $m_i/m_e \approx 1836$.

The second important concern is the relatively small domains of these simulations when compared to physical scales. The simulations described in this thesis have characteristic length scales on the order of tens or hundreds of d_i. The proton inertial length is ~ 500 km in the magnetosphere, so that the simulations are on the scale of a few earth radii. The proton inertial length is only a few tens of meters in the solar corona, so that these simulations represent volumes of km^3, much smaller than the Mm^3 flaring regions.

It is therefore important to examine how these results depend on system size and the mass ratio in order to determine how they scale to physically relevant regimes. We will first address the issue of the system size by exploring a simulation with dimensions larger than that discussed in the previous chapter. We will then address the mass ratio issue by exploring a simulation with $m_i/m_e = 100$.

6.1 Spatial Domain Size Scaling

In order to examine the dependence on the system size, we performed a simulation with $L_x \times L_y \times L_z = 102.4d_i \times 51.2d_i \times 25.6d_i$. This doubles both L_x and L_y with respect to the simulation discussed in detail in the previous chapter, and leaves L_z unchanged (we found that the important 3D features were insensitive to L_z so long as $L_z \geq 6.4d_i$).

Figures 6.1 and 6.2 show the energetic electron spatial distribution in the 2D and 3D simulations at two different times. The characteristic scales of the island structures increase with time as earlier structures coalesce. As was the case in the smaller domains, the energetic electrons are confined to narrow rings in 2D, and are instead relatively uniformly distributed throughout the reconnecting region in 3D. The evolution of the energetic electron spectra as a function of time is shown in Fig. 6.3. Figure 6.4 shows the same spectra normalized to the 3D spectrum at $\Omega_{ci}t = 125$ to emphasize the behavior of electrons at high energy. In 2D the evolution of the spectra slows down at late time while in 3D the spectra at high energy continue to separate in time, suggesting that the 3D physics becomes more important as the

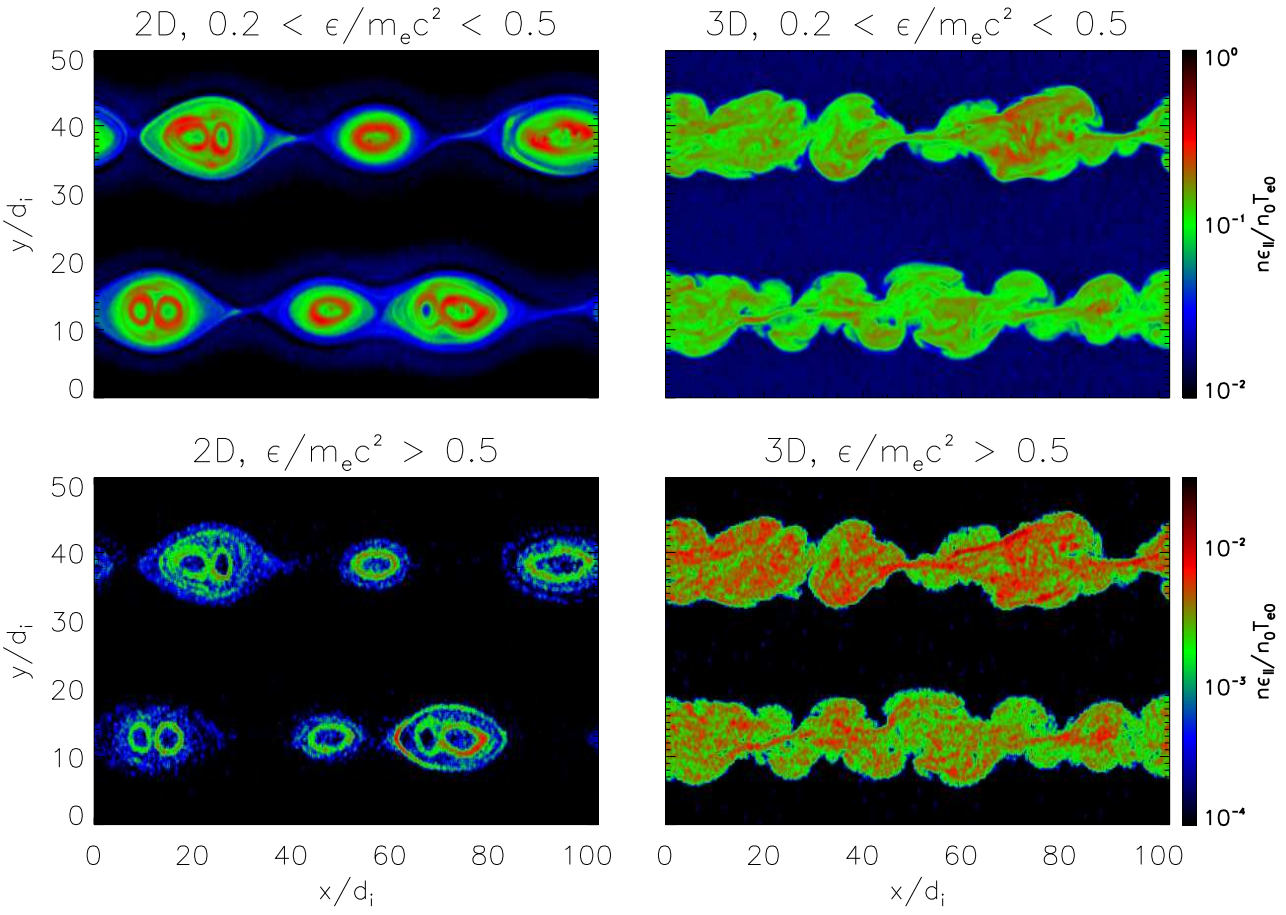

Figure 6.1: Spatial distribution of parallel energy density for electrons in 2D and 3D simulations at $\Omega_{ci}t = 75$. The spatial distribution for the 3D simulation represents the plane $z = 0$. Plot titles list the electron energy range for each panel.

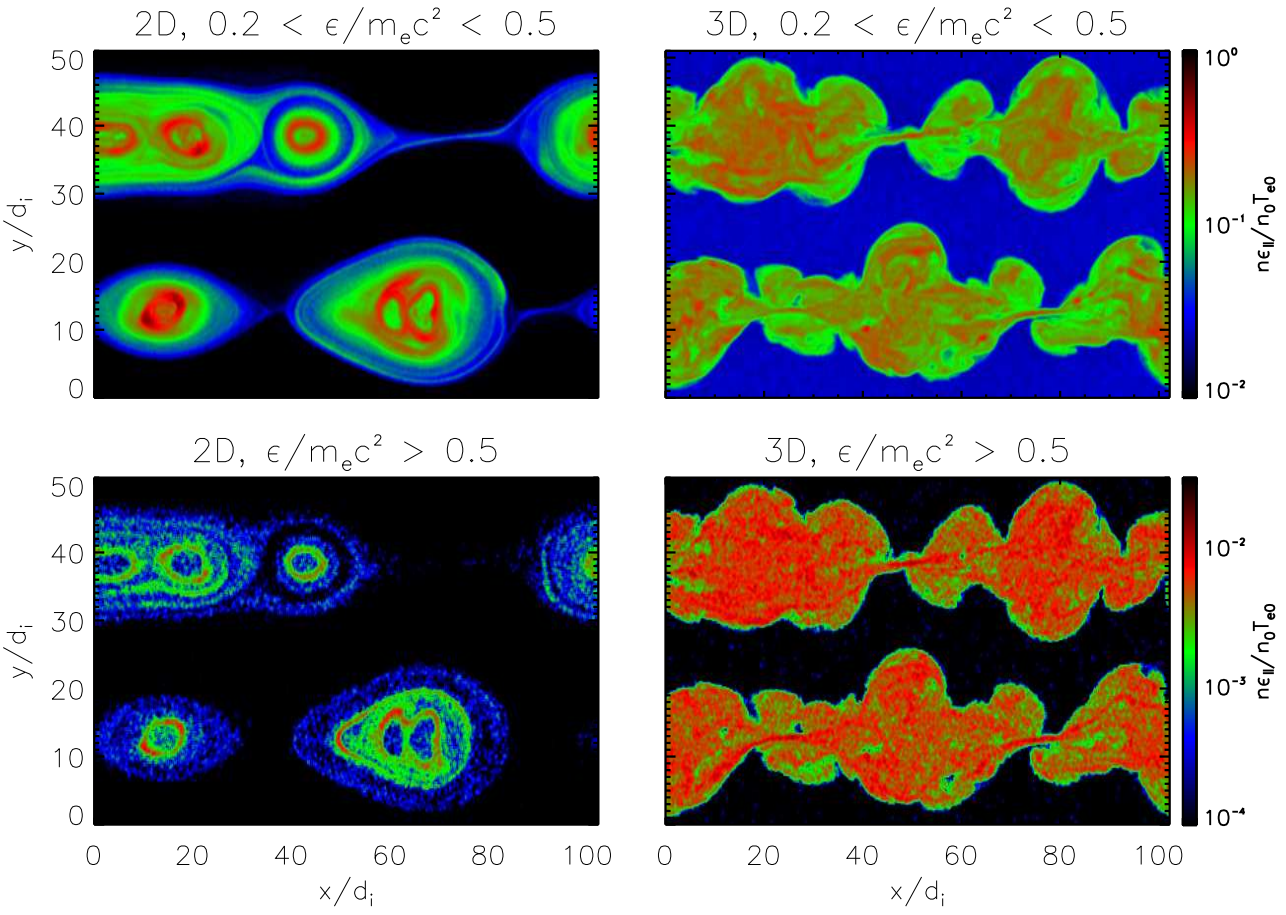

Figure 6.2: Spatial distribution of parallel energy density for electrons in 2D and 3D simulations at $\Omega_{ci}t = 125$. The spatial distribution for the 3D simulation represents the plane $z = 0$. Plot titles list the electron energy range for each panel.

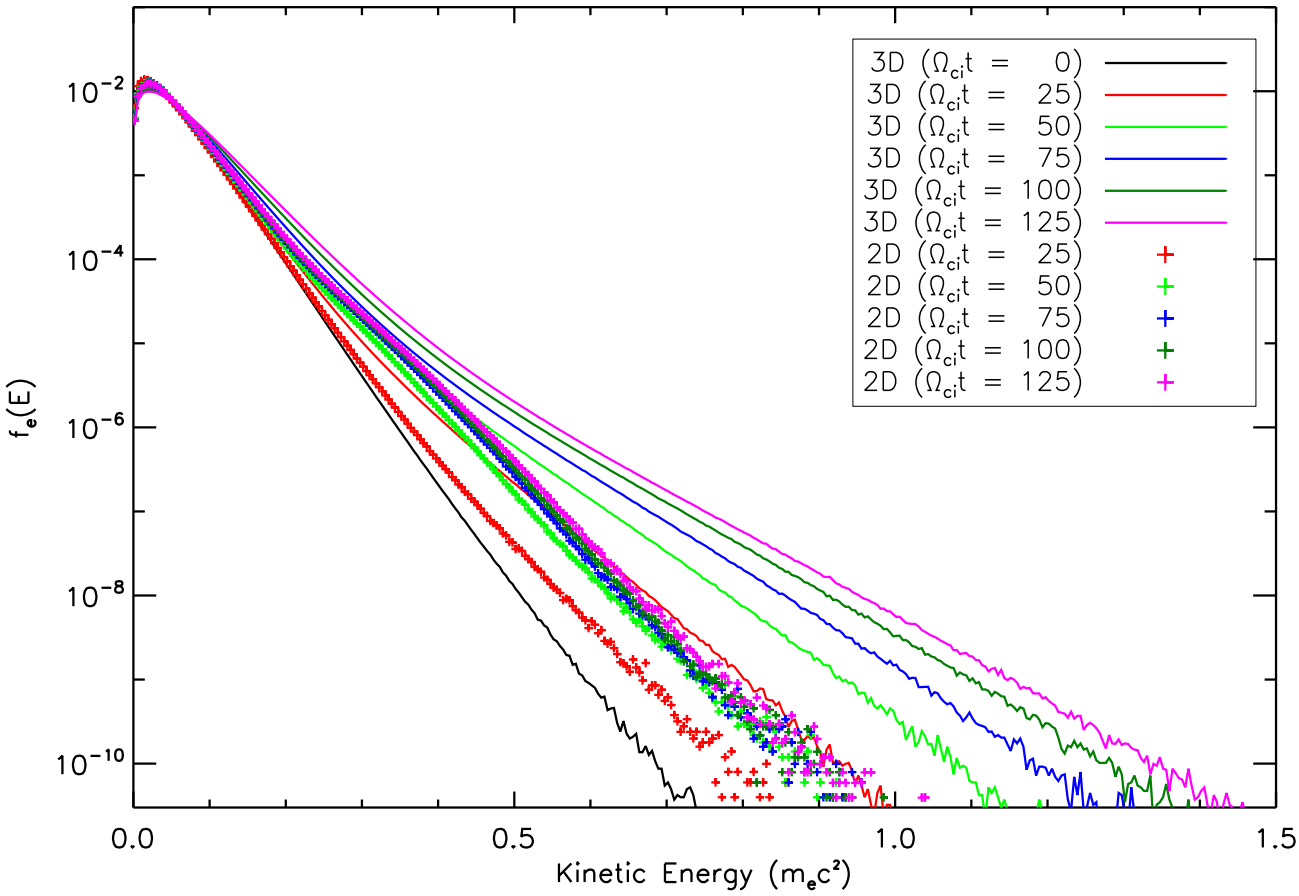

Figure 6.3: Electron kinetic energy spectra for simulations with $L_x \times L_y = 102.4d_i \times 51.2d_i$. The separation between spectra in the 2D and 3D systems increases with time, suggesting that this behavior scales favorably with the system size.

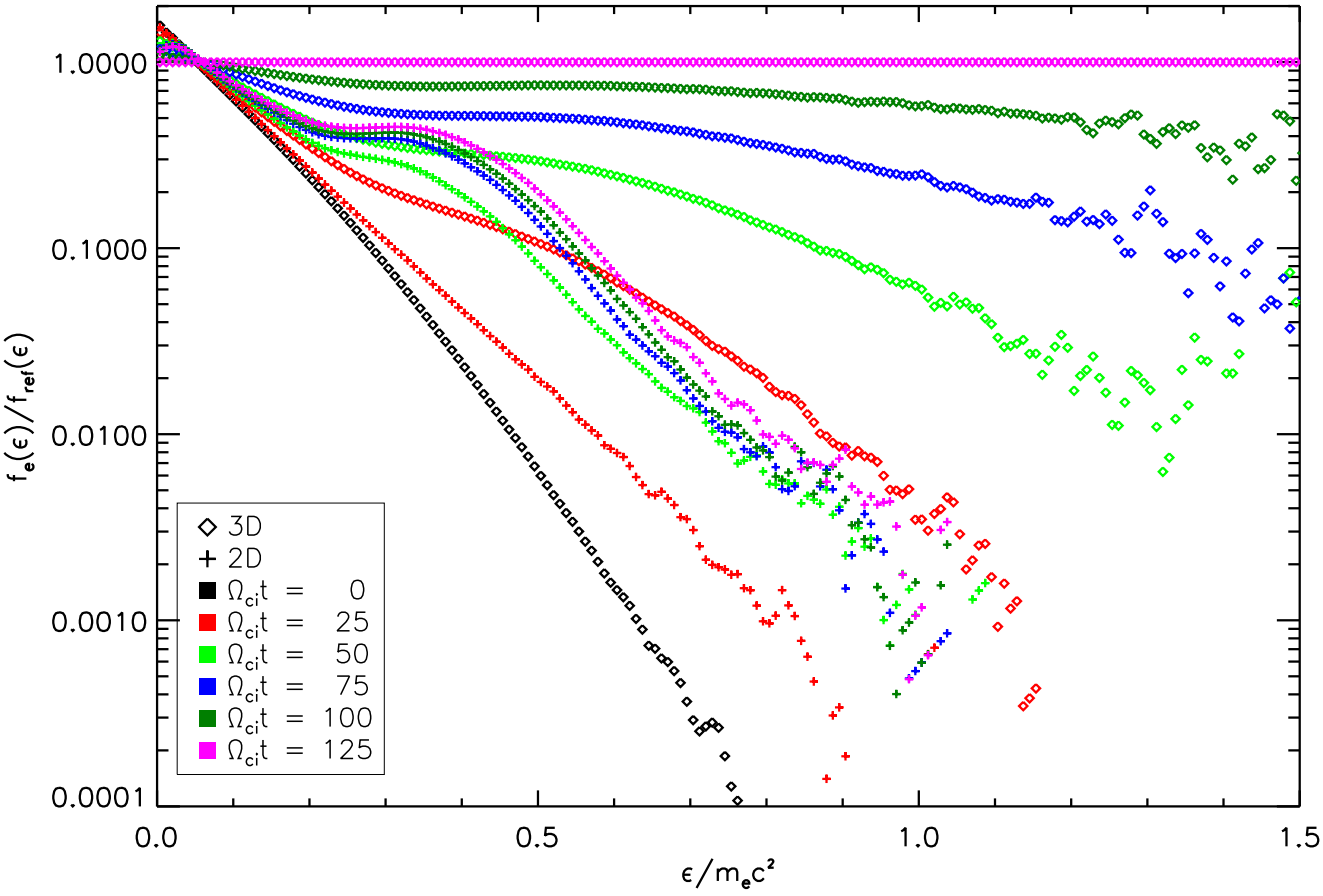

Figure 6.4: Electron energy spectra for simulations with $L_x \times L_y = 102.4d_i \times 51.2d_i$. The spectra are normalized to the 3D spectrum at $t = 125$. At late time electrons in the 2D simulation show very little enhancement at high energies. The 3D spectra show that the energetic electrons continue to gain energy, and that the energetic portion of the spectrum continues to fill in throughout the simulation.

characteristic scale lengths (and hence the system size) increases. The energetic electrons continue to fill in at high energies for the 3D simulation, suggesting that the maximum energy gain depends on the time scale of reconnection and hence the spatial scale of the system. Hence though the energy gain in these simulations is relatively modest compared to the initial energy; in real systems the maximum energy gain is likely to be very large because the electrons continue to steadily gain energy during the entire time evolution of the system —a larger system will accelerate particles for a longer period of time.

6.2 Mass Ratio Scaling

In this section, we explore a simulation with a mass ratio of $m_i/m_e = 100$ and $L_x \times L_y \times L_z = 51.2d_i \times 25.6d_i \times 12.8d_i$ and compare it with a 2D simulation with $L_x \times L_y = 51.2d_i \times 25.6d_i$ as well as a simulation with the same dimensions and $m_i/m_e = 25$. The initial current sheet width is $w_0 = 1.25d_e$ for both simulations (this corresponds to $w_0 = d_i/4$ for mass-ratio 25 and $w_0 = d_i/8$ for mass-ratio 100).

The spatial distribution of energetic electrons in the 2D and 3D simulations are shown in figure 6.5. The electron energy spectra, shown in Fig. 6.6 show a substantial separation between 2D and 3D distributions which increases with time. This can be most easily seen by comparing the $t = 20$ and $t = 50$ spectra for the 2D and 3D simulations; there is a much larger enhancement between these two times for the 3D simulation. Figure 6.7 shows spectra from simulations with two mass ratios. The number of energetic electrons is slightly greater in the mass ratio 100

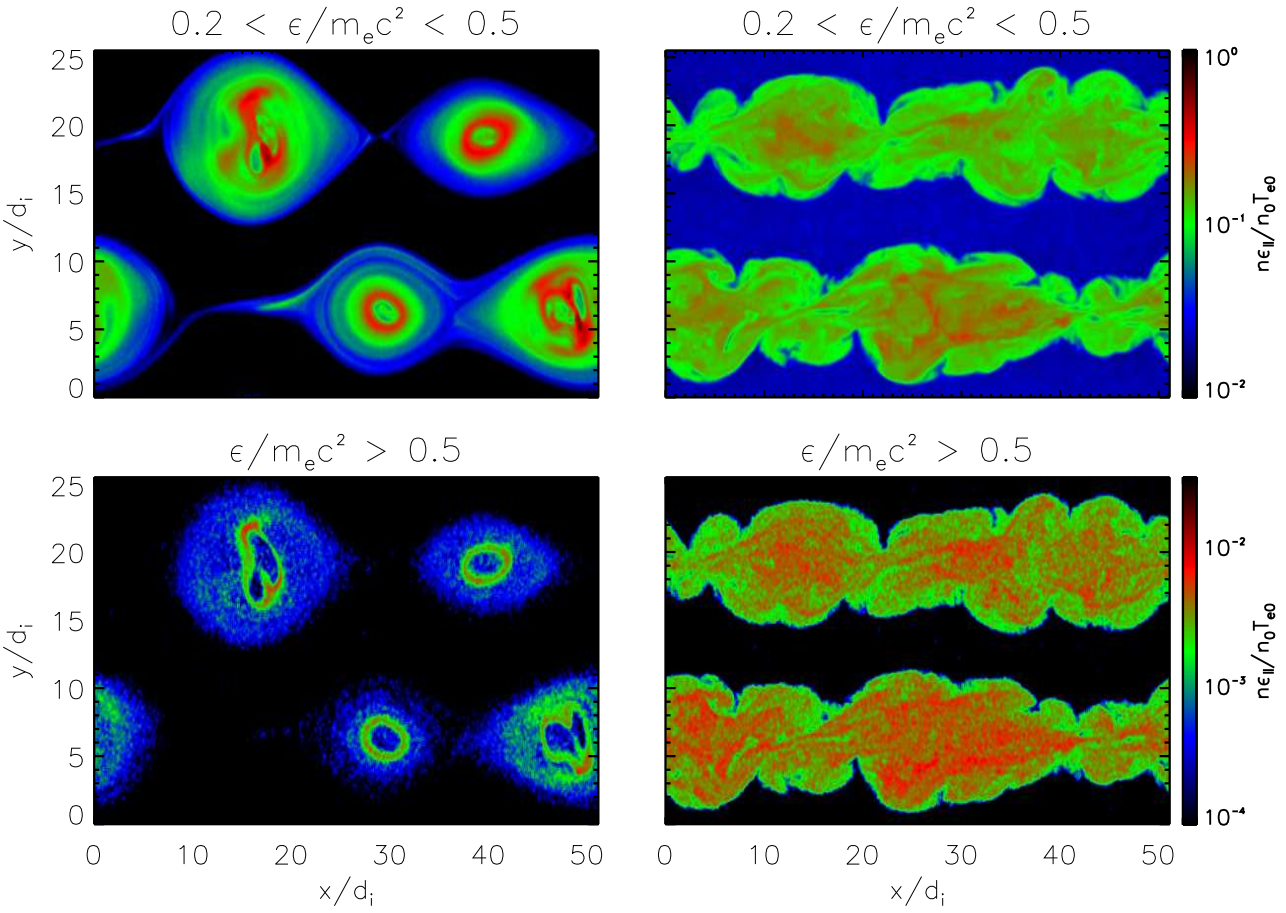

Figure 6.5: Spatial distribution of parallel energy density for electrons in 2D and 3D simulations with mass ratio $m_i/m_e = 100$ at $\Omega_{ci}t = 50$. The spatial distribution for the 3D simulation represents the plane $z = 0$. Plot titles list the electron energy range for each panel.

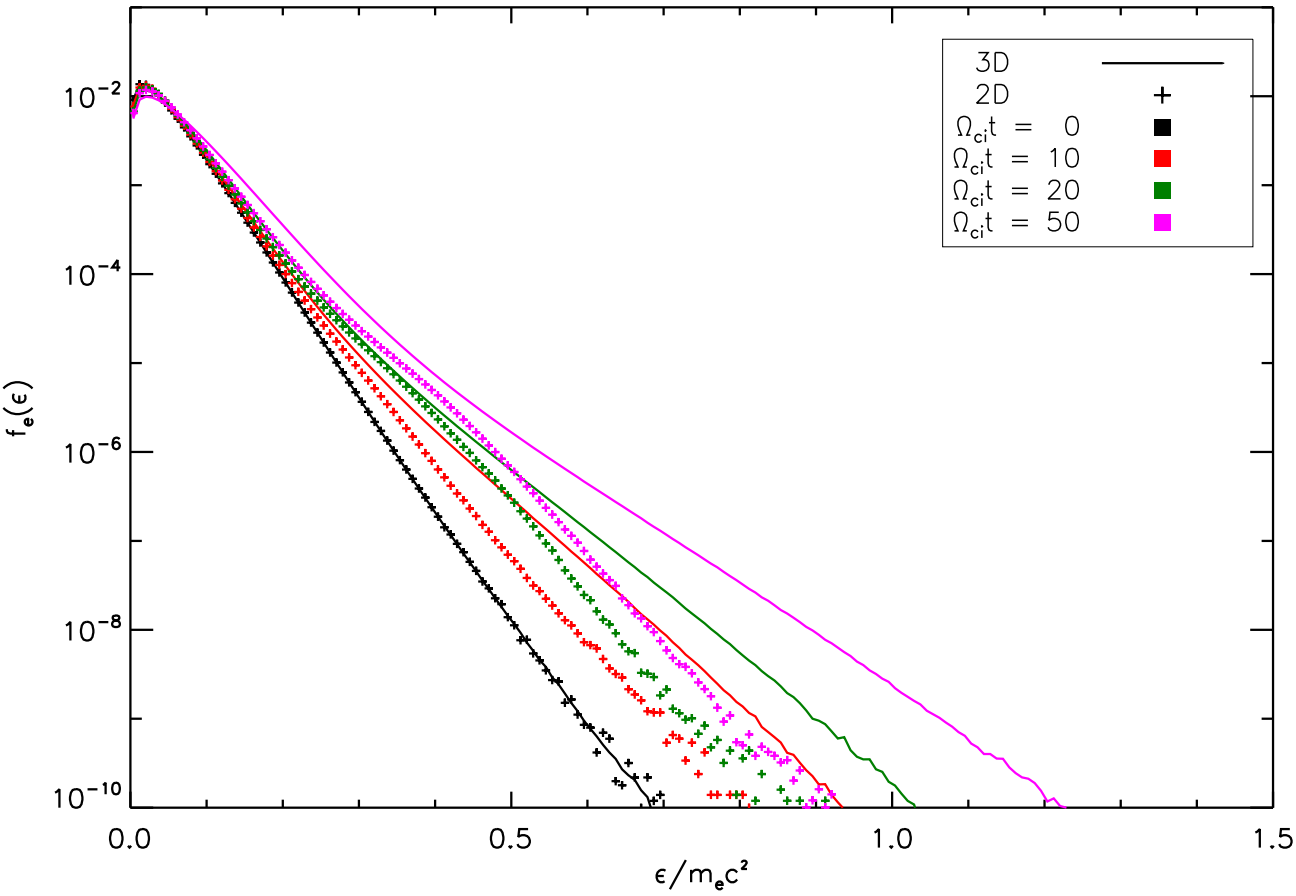

Figure 6.6: Electron energy spectra for simulations with mass ratio $m_i/m_e = 100$.

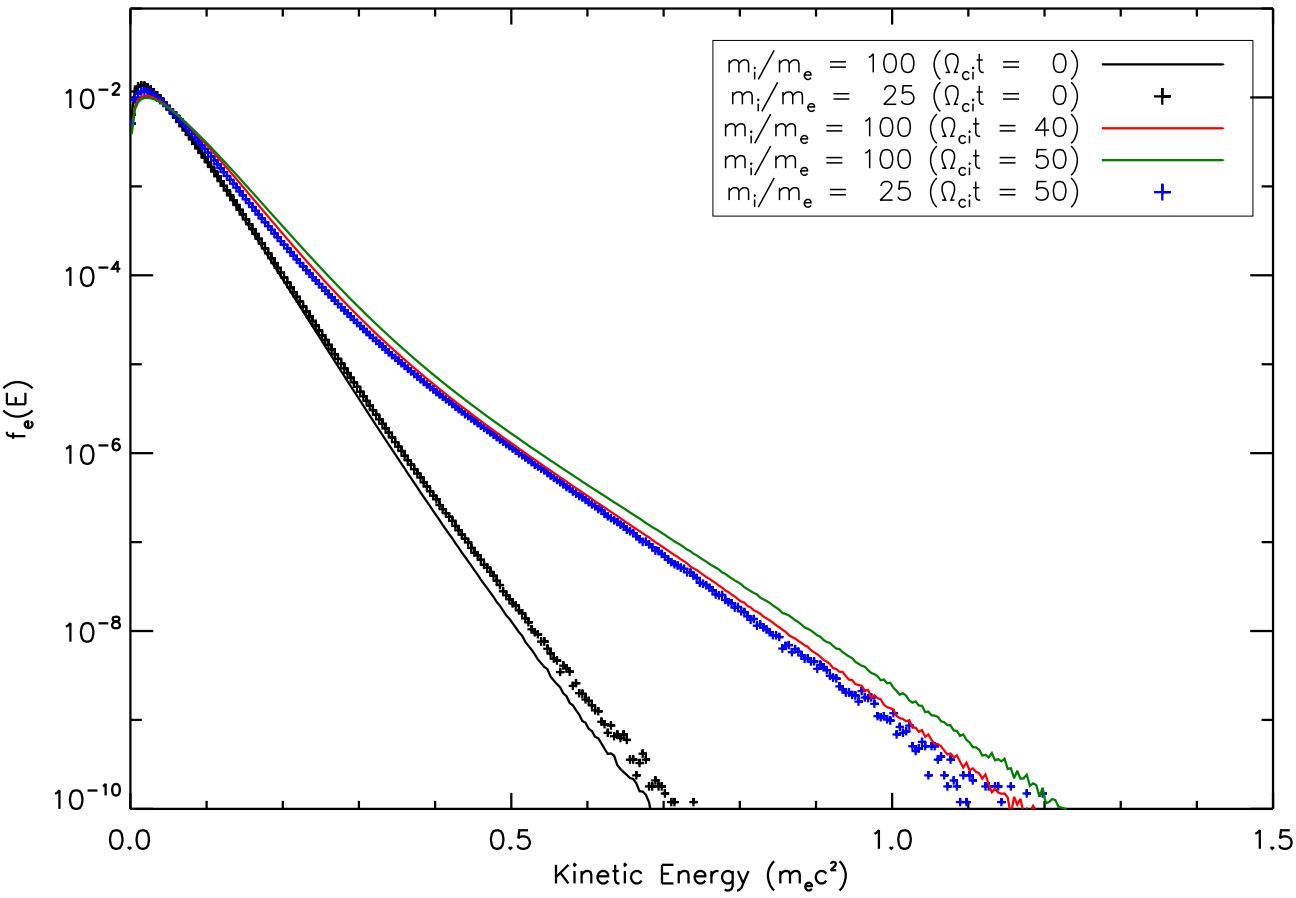

Figure 6.7: Electron energy spectra for 3D simulations with $L_x \times L_y \times L_z = 51.2d_i \times 25.6d_i \times 12.8d_i$.

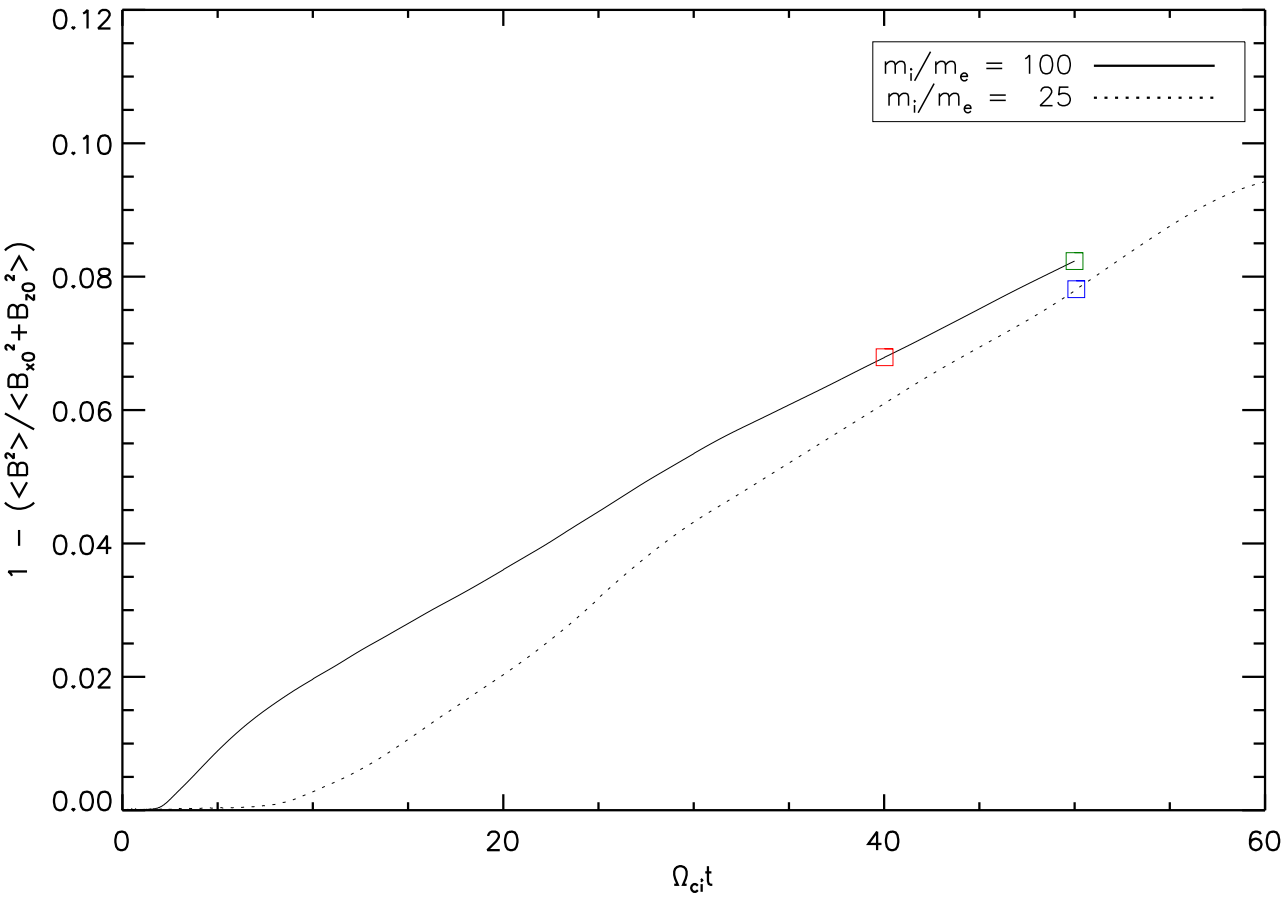

Figure 6.8: Magnetic energy dissipated vs. time in simulations with $L_x \times L_y \times L_z = 51.2d_i \times 25.6d_i \times 12.8d_i$. Colored boxes correspond to same-color lines in fig. 6.7.

simulation at $t = 50$. However, according to figure 6.8, reconnection onset occurs approximately $10\Omega_{ci}^{-1}$ earlier for the mass-ratio 100 simulation compared with the mass-ratio 25 simulation (reconnection onset is faster for smaller w_0/d_i) Accounting for this offset (red line in Fig. 6.7) the difference between the two simulations is negligible.

6.3 Discussion

In this chapter, we examined how particle acceleration in 3D reconnection scales with the mass ratio and the system size. We found that as time proceeds (and the reconnecting region grows) the distinction between 3D and 2D electron acceleration physics increases. The energetic spectra in the 3D system continue to fill in. In contrast, the energetic particle spectra from 2D simulations seem to saturate as the most energetic electrons become trapped in islands that have already undergone contraction but have not yet merged with other islands. This suggests that the qualitative differences between these simulations are robust for large spatial scales, and should play an important role for systems such as the solar corona.

We also examined how the dynamics of reconnection and the electron energy gain depends on the mass ratio, and found that the 3D structuring of the magnetic field and the associated enhancement of electron energy gain continues as the ion-to-electron mass-ratio is increased. The qualitative features of the energetic spectra and the spatial distribution of energetic particles were not sensitive to the mass ratio. The enhanced acceleration in the 3D system is contingent on the separation

between proton and electron scales so that the electrons may explore the system on a faster time scale than that of the macroscopic dynamics tied to proton time scales. The limit $m_i \gg m_e$ is therefore favorable for the enhancement of electron acceleration.

Chapter 7: Conclusions

7.1 Summary

In this thesis, I used kinetic PIC simulations to examine electron energization mechanisms in magnetic reconnection. In 2D simulations of kinetic reconnection, I found that Fermi reflection dominated electron energy gain for reconnection with a weak guide field while in the case of a strong guide field Fermi reflection and parallel electric fields played comparable roles. In both cases betatron acceleration was small and in fact acted as an energy sink since the magnetic field strength is reduced during reconnection —the conservation of the electron magnetic moment therefore produces a reduction of the electron perpendicular energy. Since both Fermi reflection and parallel electric fields increase the parallel energy of electrons, the late time spectra displayed extreme anisotropy with the parallel energy being much greater than the perpendicular energy. The Fermi mechanism is the dominant accelerator of the most energetic electrons, which was expected because Fermi reflection is quadratic in the electron velocity while the parallel electric field is linear. Additionally, I found that parallel electric fields are localized to small regions near the X-lines, and might be expected to have negligible impact in large astrophysical systems. I then explored 3D simulations of reconnection, and found that the

stochastic field structure that develops in a 3D system facilitates energetic electrons access to regions where magnetic energy is released, dramatically enhancing the production of superthermal particles. These energetic particles were spatially distributed throughout the reconnecting region rather than being confined to narrow boundary layers as occurs in 2D systems. A consequence of the enhanced mobility of energetic electrons in 3D is that robust energy gain of the energetic component continues to the end of the simulations while in 2D energy gain stagnates because energetic electrons are trapped in fully contracted islands where further energy gain is not possible without merging with other islands.

7.2 Comparison to Observations

Direct comparison of simulations to observational results is difficult, especially given that power-law spectra do not form. However, a simple analytical argument can be carried out to show that the Fermi mechanism is capable of driving sufficient energy gain to produce MeV particles such as those observed in solar flares (e.g. Krucker et al. 2010 [17]). According to recent scaling studies [62], the electron heating at a single X-line is $\Delta T_e \approx 0.033 m_i c_A^2$. If the initial electron energy is neglected, a density of $10^9/\mathrm{cm}^3$ and magnetic field $B \approx 50\mathrm{G}$ implies that the seed electron temperature arising from reconnection at a single X-line is $T_e \approx 4\mathrm{keV}$. Further energy gain takes place during the merger of magnetic islands. Two islands of nearly equal size reduce the field line length by around $\sqrt{2}$. The invariance of the action as discussed in Chapter 2.6.3 then implies that the parallel particle velocity

increases by the same factor of $\sqrt{2}$. During an island merger, an energetic particle can therefore roughly double its energy as the contracting field lines shorten. A thermal electron therefore requires only ≈ 8 island mergers to attain an energy of 1MeV.

The island merger time can be estimated as $t_{merge} \approx \ell/(0.1c_A)$, where ℓ is the island size and $0.1c_A$ is the reconnection rate given in terms of the Alfvén speed. In the flare observed by Krucker et al., $c_A \approx 3 \times 10^3$km/s. For an island scale size $\ell \approx 100$km (in a flaring region with a length scale ~ 10Mm), the merger time is $t_{merge} < 1$s so 1MeV electrons can be produced in around 10s. Since the hard X-ray decay time is around 40s, Fermi reflection is sufficiently fast to account for the production of MeV electrons in this event.

7.3 Future Work

There are a number of useful ways to extend the results described in this thesis. An important extension would be a rigorous scaling study that explores how the relative roles of the various acceleration mechanisms depend on parameters such as the guide field, plasma beta, and system size. The role of the guide field has been partially addressed in this work, but would benefit from an analytical treatment that could be applied to specific physical situations. The dependence on the plasma beta was largely unaddressed in this thesis, as the simulations used initial conditions where β was of order unity. Beam-driven instabilities in low β systems can generate turbulence that might play a role in particle energization.

The dependence of particle acceleration on the system size is a challenging problem. The kinetic scales of regions with significant $E_{\parallel}$ suggest that this term would be negligible in large systems. However, the continuous generation of magnetic islands during reconnection leads to a broad distribution of magnetic island sizes [23, 63], including many at kinetic scales. The relative role of these small ('secondary') islands in particle acceleration remains an open question but they are expected to play an important role because of the short time scale required for their contraction and merger with similar size islands.

The electron energy spectra in the simulations presented in this thesis do not form power-laws as is observed in nature. Drake et al. [53] have suggested that power-law formation requires particle loss, which does not occur in periodic simulations. However, recent studies [60, 61] suggest that power-law spectra may still form in such systems. Guo et al. [60] argue that the dominant curvature-drift mechanism acting on an initial distribution preserves its form, effectively only increasing the temperature. In their model, a continuous injection of particles leads to overlapping distribution functions which, when added together, form a power-law. Rather than particle loss, injection is invoked as necessary for power-law formation.

The stochastic magnetic field that develops in 3D reconnection has important implications for particle loss. In 2D systems where islands trap particles on closed flux surfaces, particles primarily leave the system due to the convection of magnetic islands away from the reconnecting region (this is true so long as the gyroradius is much smaller than the scale size of the islands, which is typically true for electrons). The breakdown of magnetic surfaces in 3D enables particles to pass between flux

ropes, so that they might leave the reconnecting region faster than would occur due to pure convection. Transport on random-walking field lines operates as a diffusive process, so its relative role in particle loss should depend on the system size.

There are many astrophysical systems that are too large for kinetic PIC modeling of the entire domain to be feasible. In order to include the effects of particle acceleration in these systems, it is vital to capture both the large-scale dynamics and the important kinetic physics important for particle acceleration. The energization due to Fermi reflection can, in principle, be calculated in fluid (MHD) models, as it can be determined from the bulk flow and magnetic curvature. A method for including energetic particle back pressure in fluid models is somewhat less clear, and warrants further study.

Appendix A: Energization Terms Derived using a Gyrotropic Pressure Tensor

The acceleration mechanisms described in Chapter 2.6.3 may be derived via the momentum equation (including an gyrotropic pressure tensor) and Maxwell's Equations. In the reconnection process, we are primarily concerned with the dissipation of magnetic energy. We begin with Faraday's law:

$$\begin{aligned}
\frac{\partial \mathbf{B}}{\partial t} &= -c\nabla \times \mathbf{E} \\
\frac{\mathbf{B}}{4\pi} \cdot \frac{\partial \mathbf{B}}{\partial t} &= -\frac{\mathbf{B}}{4\pi} \cdot c\nabla \times \mathbf{E} \\
\frac{\partial}{\partial t}\frac{B^2}{8\pi} &= -\nabla \cdot \left(\frac{c}{4\pi}\mathbf{E} \times \mathbf{B}\right) - \mathbf{E} \cdot \frac{c\boldsymbol{\nabla} \times \mathbf{B}}{4\pi} \\
\frac{\partial}{\partial t}\frac{B^2}{8\pi} &= -\nabla \cdot \left(\frac{c}{4\pi}\mathbf{E} \times \mathbf{B}\right) - \mathbf{E} \cdot \mathbf{J}
\end{aligned}$$

where we have used Ampère's law, neglecting the displacement current. The first term on the right corresponds to the divergence of the Poynting flux, and the second term corresponds with work done by the electromagnetic fields.

The momentum equation is:

$$\rho\frac{d\mathbf{V}}{dt} = \frac{\mathbf{J} \times \mathbf{B}}{c} - \nabla \cdot \left[(P_{\parallel} - P_{\perp})\mathbf{bb} + P_{\perp}\mathbf{I}\right]$$

where $\mathbf{V}$ is the bulk flow, $P_{\parallel}$ and $P_{\perp}$ are the parallel and perpendicular pressures, $\mathbf{b}$ is the unit vector in the direction of the local magnetic field, and $\mathbf{I}$ is the identity

tensor.

The current perpendicular to the magnetic field is then given by:

$$\mathbf{J}_\perp = \frac{c\mathbf{B}}{B^2} \times \left[\rho \frac{d\mathbf{V}_\perp}{dt} + \nabla P_\perp + \frac{(P_\parallel - P_\perp)}{B^2} (\mathbf{B} \cdot \nabla)\mathbf{B} \right] \tag{A.1}$$

We may separate this current into a magnetization current $\mathbf{J}_{\mathbf{m}\perp} = c(\nabla \times \mathbf{M})_\perp$ and a free current $\mathbf{J}_{\mathbf{f}\perp}$. The magnetization corresponds to the magnetic moment density which is given by:

$$\mathbf{M}(\mathbf{r}) = -\int \frac{m v_\perp^2 \mathbf{b}}{2B} f(\mathbf{r}, \mathbf{v}) d^3\mathbf{v} = -\frac{P_\perp \mathbf{B}}{B^2} = -\beta_\perp \frac{\mathbf{B}}{8\pi}$$

The two current terms are then:

$$\begin{aligned}
\mathbf{J}_{\mathbf{m}\perp} &= c(\nabla \times \mathbf{M})_\perp \\
&= \frac{c\mathbf{B}}{B^2} \times \left[\nabla P_\perp - \frac{P_\perp}{2B^2} \nabla B^2 - \frac{P_\perp}{B^2} (\mathbf{B} \cdot \nabla)\mathbf{B} \right] \\
\mathbf{J}_{\mathbf{f}\perp} &= \mathbf{J}_\perp - \mathbf{J}_{\mathbf{m}\perp} \\
&= \frac{c\mathbf{B}}{B^2} \times \left[\frac{P_\perp}{2B^2} \nabla B^2 + \frac{P_\parallel}{B^2} (\mathbf{B} \cdot \nabla)\mathbf{B} + \rho \frac{d\mathbf{V}_\perp}{dt} \right]
\end{aligned}$$

The magnetization current contains the diamagnetic drift current (the first term) and other terms which do not correspond to individual particle motions. In contrast, the free current contains terms associated with single-particle drifts: the first term corresponds to the grad-B drift ($\propto \mathbf{B} \times \nabla B$), the second corresponds to the curvature drift ($\propto \mathbf{B} \times (\mathbf{B} \cdot \nabla \mathbf{B})$) and the third term corresponds to the polarization drift.

It is worth examining some features of the work done on the full magnetization

current:

$$\begin{aligned}\mathbf{E}\cdot\mathbf{J_m} &= \mathbf{E}\cdot(c\nabla\times\mathbf{M})\\ &= c\mathbf{M}\cdot(\nabla\times\mathbf{E}) - c\nabla\cdot(\mathbf{E}\times\mathbf{M})\\ &= \mathbf{M}\cdot\frac{\partial\mathbf{B}}{\partial t} - \nabla\cdot\left(P_\perp\frac{c\mathbf{E}\times\mathbf{B}}{B^2}\right)\\ &= \mathbf{M}\cdot\frac{\partial\mathbf{B}}{\partial t} - \nabla\cdot(P_\perp\mathbf{V}_\perp)\end{aligned}$$

This term is generally associated with the diamagnetic properties of the plasma. The first term corresponds to betatron acceleration via the electromotive force (associated with $\boldsymbol{\nabla}\times\mathbf{E}$) acting on gyrating particles. The second term corresponds to the change in the magnetic field due to a flux of magnetic dipoles. The divergence of this flux corresponds to a change in the local diamagnetic properties of the plasma due to a change in the magnetization ($\mathbf{M}\propto P_\perp$).

We must now determine the parallel free current, which is modified through terms that arise in $c(\nabla\times\mathbf{M})_\parallel$:

$$\begin{aligned}J_{\mathbf{f}\parallel} &= J_\parallel - \mathbf{b}\cdot(c\nabla\times\mathbf{M})\\ &= J_\parallel + \mathbf{b}\cdot\left(c\nabla\times\frac{P_\perp\mathbf{B}}{B^2}\right)\\ &= J_\parallel + \frac{4\pi P_\perp}{B^2}\mathbf{b}\cdot\left(\frac{c}{4\pi}\nabla\times B\right)\\ &= \left(1+\frac{\beta_\perp}{2}\right)J_\parallel\end{aligned}$$

The $\beta_\perp/2$ term arises from the Baños parallel drift (e.g. Appendix B of Northrop and Rome, 1978):

$$v_{\mathbf{d}\parallel} = \frac{v_\perp^2}{2\Omega_{ce}}\mathbf{b}\cdot(\nabla\times\mathbf{b}) \tag{A.2}$$

This velocity is typically small compared to the thermal velocities of energetic particles, as it is of order $v_\perp(\rho_e/\ell)$ where ℓ is the length scale. We now have all of the necessary terms to separate $\mathbf{J}$ as free current and magnetization current. We finally arrive at the following form for the evolution of $B^2/8\pi$:

$$\begin{aligned}\frac{\partial}{\partial t}\frac{B^2}{8\pi} =& -\nabla\cdot\left(\frac{c}{4\pi}\mathbf{E}\times\mathbf{B}\right)+\nabla\cdot(P_\perp\mathbf{V}_\perp)\\ &-\frac{\beta_\perp}{2}\left(\frac{\partial}{\partial t}+\mathbf{V}_\perp\cdot\nabla\right)\frac{B^2}{8\pi}\\ &-E_\parallel J_\parallel\left(1+\frac{\beta_\perp}{2}\right)\\ &-\rho\frac{d}{dt}\frac{V_\perp^2}{2}\\ &-P_\parallel\mathbf{V}_\perp\cdot\left[\frac{\mathbf{B}\cdot\nabla\mathbf{B}}{B^2}\right]\end{aligned}$$

The first term is the divergence of the Poynting flux, the second term is the divergence of the flux of magnetic dipoles. The third term corresponds to betatron acceleration (μ conservation). The fourth term is the work done by the parallel electric field on the free current, modified by the Baños drift. The fifth term corresponds to the polarization drift, or bulk perpendicular acceleration of the plasma. The final term corresponds to Fermi reflection associated with the curvature drift.

Bibliography

[1] R. C. Carrington. Description of a singular appearance seen in the sun on september 1, 1859. *MNRAS*, 20:13–15, 1859.

[2] R. Hodgson. On a curious appearance seen in the sun. *MNRAS*, 20:15–16, 1859.

[3] E.W. Cliver and L. Svalgaard. The 1859 solar–terrestrial disturbance and the current limits of extreme space weather activity. *Solar Physics*, 224(1-2):407–422, 2004.

[4] R. G. Giovanelli. Magnetic and electric phenomena in the sun's atmosphere associated with sunspots. *Monthly Notices of the Royal Astronomical Society*, 107(4):338–355, 1947.

[5] J.W. Dungey. Conditions for the occurrence of electrical discharges in astrophysical systems. *The London, Edinburgh, and Dublin Philosophical Magazine and Journal of Science*, 44(354):725–738, 1953.

[6] J.W. Dungey. Neutral point discharge theory of solar flares. a reply to cowling's criticism. *Electromagnetic Phenomena in Cosmical Physics, Proceedings from IAU Symposium*, 6:135, 1958.

[7] E. N. Parker. Acceleration of cosmic rays in solar flares. *Phys. Rev.*, 107:830–836, 1957.

[8] P. A. Sweet. *Electromagnetic Phenomena in Cosmical Physics*, page 123. Cambridge University Press, New York, 1958.

[9] E. N. Parker. The Solar-Flare Phenomenon and the Theory of Reconnection and Annihiliation of Magnetic Fields. *Astrophys. Journal Supp.*, 8:177, July 1963.

[10] Harry E. Petschek. Magnetic field annihilation. In *Proc. AAS-NASA Symp. Phys. Solar Flares*, volume 50 of *NASA-SP*, pages 425–439, 1964.

[11] Masayuki Ugai and Takao Tsuda. Magnetic field-line reconnexion by localized enhancement of resistivity: Part 1. evolution in a compressible mhd fluid. *Journal of Plasma Physics*, 17:337–356, 6 1977.

[12] D. Biskamp. Magnetic reconnection via current sheets. *Phys. Fluids*, 29(5):1520–1531, 1986.

[13] J. Birn, J. F. Drake, M. A. Shay, B. N. Rogers, R. E. Denton, M. Hesse, M. Kuznetsova, Z. W. Ma, A. Bhattacharjee, A. Otto, and P. L. Pritchett. Geospace Environmental Modeling (GEM) magnetic reconnection challenge. *J. Geophys. Res.*, 106(A3):3715–3719, 2001.

[14] K. A. Anderson and J. R. Winckler. Solar flare x-ray burst on september 28,1961. *Journal of Geophysical Research*, 67(11):4103–4117, 1962.

[15] R. P. Lin and H. S. Hudson. 10-100 keV electron acceleration and emission from solar flares. *Solar Phys.*, 17:412–435, 1971.

[16] R. P. Lin, S. Krucker, G. J. Hurford, D. M. Smith, H. S. Hudson, G. D. Holman, R. A. Schwartz, B. R. Dennis, G. H. Share, R. J. Murphy, A. G. Emslie, C. Johns-Krull, and N. Vilmer. RHESSI observations of particle acceleration and energy release in an intense solar gamma-ray line flare. *Ap. J.*, 595:L69–L76, 2003.

[17] Säm Krucker, H. S. Hudson, L. Glesener, S. M. White, S. Masuda, J.-P. Wuelser, and R. P. Lin. Measurements of the coronal acceleration region of a solar flare. *Ap. J.*, 714:1108–1119, 2010.

[18] M. Oka, S. Ishikawa, P. Saint-Hilaire, S. Krucker, and R. P. Lin. Kappa distribution model for hard x-ray coronal sources of solar flares. *The Astrophysical Journal*, 764(1):6, 2013.

[19] A. G. Emslie, H. Kucharek, B. R. Dennis, N. Gopalswamy, G. D. Holman, G. H. Share, A. Vourlidas, T. G. Forbes, P. T. Gallagher, G. M. Mason, T. R. Metcalf, R. A. Mewaldt, R. J. Murphy, R. A. Schwartz, and T. H. Zurbuchen. Energy partition in two solar flare/CME events. *J. Geophys. Res.*, 109, 2004.

[20] M. Øieroset, R. P. Lin, T. D. Phan, D. E. Larson, and S. D. Bale. Evidence for electron acceleration up to $\sim$ 300 keV in the magnetic reconnection diffusion region of earth's magnetotail. *Phys. Rev. Lett.*, 89(19):195001, 2002.

[21] L.-J. Chen, A. Bhattacharjee, P. A. Puhl-Quinn, H. Yang, N. Bessho, S. Imada, S. Mühlbachler, P. W. Daly, B. Lefebvre, Y. Khotyaintsev, A. Vaivads, A. Fazakerley, and E. Georgescu. Observation of energetic electrons within magnetic islands. *Nature Physics*, 4:19–23, 2008.

[22] A. Retinò, R. Nakamura, A. Vaivads, Y. Khotyaintsev, T. Hayakawa, K. Tanaka, S. Kasahara, M. Fujimoto, I. Shinohara, J. P. Eastwood, M. André,

W. Baumjohann, P. W. Daly, E. A. Kronberg, and N. Cornilleau-Wehrlin. Cluster observations of energetic electrons and electromagnetic fields within a reconnecting thin current sheet in the earth's magnetotail. *Journal of Geophysical Research: Space Physics*, 113(A12), 2008. A12215.

[23] S. Y. Huang, A. Vaivads, Y. V. Khotyaintsev, M. Zhou, H. S. Fu, A. Retinò, X. H. Deng, M. André, C. M. Cully, J. S. He, F. Sahraoui, Z. G. Yuan, and Y. Pang. Electron acceleration in the reconnection diffusion region: Cluster observations. *Geophysical Research Letters*, 39(11), 2012. L11103.

[24] A. Lazarian and M. Opher. A model of acceleration of anomalous cosmic rays by reconnection in the heliosheath. *Ap. J.*, 703:8–21, 2009.

[25] J. F. Drake, M. Opher, M. Swisdak, and J. N. Chamoun. A magnetic reconnection mechanism for the generation of anomalous cosmic rays. *Ap. J.*, 709:963–974, 2010.

[26] A. A. Abdo et al. Gamma-ray flares from the crab nebula. *Science*, 331(6018):739–742, 2011.

[27] M. Tavani et al. Discovery of powerful gamma-ray flares from the crab nebula. *Science*, 331(6018):736–739, 2011.

[28] Enrico Fermi. On the origin of the cosmic radiation. *Phys. Rev.*, 75:1169–1174, Apr 1949.

[29] Elisabete M. de Gouveia Dal Pino and Alex Lazarian. Ultra-high-energy cosmic-ray acceleration by magnetic reconnection in newborn accretion-induced collapse pulsars. *The Astrophysical Journal Letters*, 536(1):L31, 2000.

[30] S. W. H. Cowley. The causes of convection in the earth's magnetosphere: A review of developments during the ims. *Reviews of Geophysics*, 20(3):531–565, 1982.

[31] Petr Hellinger, Pavel Trávníček, Justin C. Kasper, and Alan J. Lazarus. Solar wind proton temperature anisotropy: Linear theory and WIND/SWE observations. *Geophys. Res. Lett.*, 33, 2006.

[32] S. D. Bale, J. C. Kasper, G. G. Howes, E. Quataert, C. Salem, and D. Sundkvist. Magnetic fluctuation power near proton temperature anisotropy instability thresholds in the solar wind. *Phys. Rev. Lett.*, 103, 2009.

[33] K. M. Schoeffler, J. F. Drake, and M. Swisdak. The effects of plasma beta and anisotropy instabilities on the dynamics of reconnecting magnetic fields in the heliosheath. *Ap. J.*, 743(1):70, 2011.

[34] K. M. Schoeffler, J. F. Drake, M. Swisdak, and K. Knizhnik. The role of pressure anisotropy on particle acceleration during magnetic reconnection. *The Astrophysical Journal*, 764(2):126, 2013.

[35] J. F. Drake, M. Swisdak, C. Cattell, M. A. Shay, B. N. Rogers, and A. Zeiler. Formation of electron holes and particle energization during magnetic reconnection. *Science*, 299(5608):873–877, 2003.

[36] H. Che, J. F. Drake, and M. Swisdak. A current filamentation mechanism for breaking field magnetic field lines during reconnection. *Nature*, 474:184–187, 2011.

[37] J. R. Jokipii and E. N. Parker. Stochastic Aspects of Magnetic Lines of Force with Application to Cosmic-Ray Propagation. *The Astrophysical Journal*, 155:777, March 1969.

[38] A. B. Rechester and M. N. Rosenbluth. Electron heat transport in a tokamak with destroyed magnetic surfaces. *Phys. Rev. Lett.*, 40:38–41, Jan 1978.

[39] Harold P. Furth, John Killeen, and Marshall N. Rosenbluth. Finite-resistivity instabilities of a sheet pinch. *Physics of Fluids*, 6(4), 1963.

[40] R. Schreier, M. Swisdak, J. F. Drake, and P. A. Cassak. Three-dimensional simulations of the orientation and structure of reconnection X-lines. *Phys. Plasmas*, 17, 2010.

[41] W. Daughton, V. Roytershteyn, H. Karimabadi, L. Yin, B. J. Albright, B. Bergen, and K. J. Bowers. Role of electron physics in the development of turbulent magnetic reconnection in collisionless plasmas. *Nature Phys.*, 7:539–542, 2011.

[42] A. Zeiler, D. Biskamp, J. F. Drake, B. N. Rogers, M. A. Shay, and M. Scholer. Three-dimensional particle simulations of collisionless magnetic reconnection. *J. Geophys. Res.*, 107(A9):1230, 2002.

[43] William Daughton, Jack Scudder, and Homa Karimabadi. Fully kinetic simulations of undriven magnetic reconnection with open boundary conditions. *Phys. Plasmas*, 13, 2006.

[44] A. V. Divin, M. I. Sitnov, M. Swisdak, and J. F. Drake. Reconnection onset in the magnetotail: Particle simulations with open boundary conditions. *Geophys. Res. Lett.*, 34, 2007.

[45] E. G. Harris. On a plasma sheet separating regions of oppositely directed magnetic field. *Nuovo Cim.*, 23(1):115–121, 1962.

[46] Theodore G. Northrop. Adiabatic charged-particle motion. *Reviews of Geophysics*, 1(3):283–304, 1963.

[47] J. F. Drake, M. A. Shay, W. Thongthai, and M. Swisdak. Production of energetic electrons during magnetic reconnection. *Phys. Rev. Lett.*, 94:095001, 2005.

[48] J. Egedal, W. Daughton, and A. Lê. Large-scale electron acceleration by parallel electric fields during magnetic reconnection. *Nature Phys.*, 8:321–324, 2012.

[49] *Reconnection of Magnetic Fields: Magnetohydrodynamics and Collisionless Theory and Observations*, chapter 3.1 Fundamentals of Collisionless Reconnection, page 87. Cambridge University Press, Cambridge, U.K., 2007.

[50] C. Cattell, J. Dombeck, J. Wygant, J. F. Drake, M. Swisdak, M. L. Goldstein, W. Keith, A. Fazakerley, M. André, E. Lucek, and A. Balogh. Cluster observations of electron holes in association with magnetotail reconnection and comparison to simulations. *J. Geophys. Res.*, 110, 2005.

[51] J. F. Drake, M. Swisdak, H. Che, and M. A. Shay. Electron acceleration from contracting magnetic islands during reconnection. *Nature*, 443:553–556, 2006.

[52] M. Swisdak, J. F. Drake, J. McIlhargey, and M. A. Shay. The transition from anti-parallel to component magnetic reconnection. *J. Geophys. Res.*, 110, 2005.

[53] J. F. Drake, M. Swisdak, and R. Fermo. The power-law spectra of energetic particles during multi-island magnetic reconnection. *The Astrophysical Journal Letters*, 763(1):L5, 2013.

[54] Dmitri A. Uzdensky, Benoît Cerutti, and Mitchell C. Begelman. Reconnection-powered linear accelerator and gamma-ray flares in the crab nebula. *The Astrophysical Journal Letters*, 737(2):L40, 2011.

[55] P. A. Cassak, M. A. Shay, and J. F. Drake. Scaling of Sweet-Parker reconnection with secondary islands. *Phys. Plasmas*, 16, 2009.

[56] Yi-Min Huang and A. Bhattacharjee. Scaling laws of resistive magnetohydrodynamic reconnection in the high-Lundquist=number plasmoid-unstable regime. *Phys. Plasmas*, 17, 2010.

[57] J. T. Dahlin, J. F. Drake, and M. Swisdak. The mechanisms of electron heating and acceleration during magnetic reconnection. *Phys. Plasmas*, 21(9):–, 2014.

[58] Masahiro Hoshino. Stochastic particle acceleration in multiple magnetic islands during reconnection. *Phys. Rev. Lett.*, 108:135003, Mar 2012.

[59] T. C. Li, J. F. Drake, and M. Swisdak. Suppression of energetic electron transport in flares by double layers. *The Astrophysical Journal*, 757(1):20, 2012.

[60] Fan Guo, Hui Li, William Daughton, and Yi-Hsin Liu. Formation of hard power laws in the energetic particle spectra resulting from relativistic magnetic reconnection. *Phys. Rev. Lett.*, 113:155005, Oct 2014.

[61] Lorenzo Sironi and Anatoly Spitkovsky. Relativistic reconnection: An efficient source of non-thermal particles. *The Astrophysical Journal Letters*, 783(1):L21, 2014.

[62] M. A. Shay, C. C. Haggerty, T. D. Phan, J. F. Drake, P. A. Cassak, P. Wu, M. Oieroset, M. Swisdak, and K. Malakit. Electron heating during magnetic reconnection: A simulation scaling study. *Physics of Plasmas (1994-present)*, 21(12):–, 2014.

[63] R. L. Fermo, J. F. Drake, and M. Swisdak. A statistical model of magnetic islands in a current layer. *Phys. Plasmas*, 17(1):–, 2010.